TESTING OF DEMOUNTABLE SHEAR CONNECTORS

A THESIS SUBMITTED TO
THE GRADUATE SCHOOL OF NATURAL AND APPLIED SCIENCES
OF
MIDDLE EAST TECHNICAL UNIVERSITY

BY

BERK KARAKUŞ

IN PARTIAL FULFILLMENT OF THE REQUIREMENTS
FOR
THE DEGREE OF MASTER OF SCIENCE
IN
CIVIL ENGINEERING

JULY 2022

Approval of the thesis:

TESTING OF DEMOUNTABLE SHEAR CONNECTORS

submitted by **BERK KARAKUŞ** in partial fulfillment of the requirements for the degree of **Master of Science** i**n Civil Engineering, Middle East Technical University** by,

Prof. Dr. Halil Kalıpçılar
Dean, Graduate School of **Natural and Applied Sciences** _____

Prof. Dr. Erdem Canbay
Head of the Department, **Civil Engineering** _____

Prof. Dr. Cem Topkaya
Supervisor, **Civil Engineering, METU** _____

Examining Committee Members:

Prof. Dr. Kağan Tuncay
Civil Engineering, METU _____

Prof. Dr. Cem Topkaya
Civil Engineering, METU _____

Prof. Dr. Eray Baran
Civil Engineering, METU _____

Prof. Dr. Alp Caner
Civil Engineering., METU. _____

Assoc. Prof. Dr. Alper Aldemir
Civil Engineering, Hacettepe Uni. _____

Date: 05.07.2022

I hereby declare that all information in this document has been obtained and presented in accordance with academic rules and ethical conduct. I also declare that, as required by these rules and conduct, I have fully cited and referenced all material and results that are not original to this work.

Name Last name: Berk Karakuş

Signature:

ABSTRACT

TESTING OF DEMOUNTABLE SHEAR CONNECTORS

Karakuş, Berk
Master of Science, Civil Engineering
Supervisor: Prof. Dr. Cem Topkaya

July 2022, 161 pages

In composite beams, the concrete deck cannot be easily demounted from the steel I-section if welded headed stud connectors are used. A new demountable shear connector was developed as a part of this thesis to promote sustainable composite construction. The connector is composed of two angle sections and a high-strength bolt. The proposed system has been studied through a three-phase experimental program. In the first phase, 33 push-out experiments were conducted to determine the shear load-carrying capacity. The size of the angle section, bolt diameter, bolt grade, concrete strength, loading direction, and bolt thread conditions were considered as the parameters. The results showed that the proposed connector system provides shear capacities that range between 150 kN and 330 kN and shows ductile behavior. In the second phase, six pull-out experiments were conducted to determine the tensile load-carrying capacity. The size of the angle sections and total height were considered as the parameters. The experimental results showed that the proposed connector provides tensile capacities that range between 50 kN and 90 kN. In the third phase of the study, four full-scale beam specimens with varying degrees of composite action were tested to demonstrate the applicability of the proposed connectors. The bending resistance provided by the beams was similar to the ones calculated using the conventional rigid plastic analysis of stress blocks. The concrete

decks were easily demounted after the beam tests demonstrating the applicability of the proposed system for practical applications.

Keywords: Composite Structures, Sustainable Structures, Demountable Connector, Mechanical Anchorage, Experimental Investigation

ÖZ

SÖKÜLEBİLİR MEKANİK ANKRAJLARININ DENEYSEL İNCELENMESİ

Karakuş, Berk
Yüksek Lisans, İnşaat Mühendisliği
Tez Yöneticisi: Prof. Dr. Cem Topkaya

Temmuz 2022, 161 sayfa

Kompozit kirişlerde, geleneksel kaynaklı başlıklı çelik ankraj kullanıldığında, betonarme tabliye çelik I-kesitinden kolayca sökülemez. Sürdürülebilir kompozit yapıları teşvik etmek için bu tezin bir parçası olarak yeni bir sökülebilir kesme ankrajı geliştirilmiştir. Geliştirilen ankraj, iki adet farklı boyutlardaki korniyer kesitten ve yüksek mukavemetli bir bulondan oluşmaktadır. Önerilen sistem, üç fazlı bir deneysel program aracılığıyla incelenmiştir. İlk fazda, 33 adet itme deneyi bağlantı elemanının kesme kapasitesini ve davranışını, korniyer boyutu, bulon çapı, bulon dayanımı, beton dayanımı, yükleme yönü ve bulon diş durumu gibi parametrelerin etkisi altında, incelemek için gerçekleştirilmiştir. Sonuçlar, önerilen bağlantı sisteminin 150 kN ile 330 kN arasında değişen kesme kapasiteleri sağladığını ve sünek bir davranış sergilediğini göstermiştir. İkinci fazda, 6 adet çekme deneyi bağlantı elemanının çekme kapasitesini ve davranışını, korniyer boyutu ve toplam yükseklik gibi parametrelerin etkisi altında, incelemek için gerçekleştirilmiştir. Deneysel sonuçlar, önerilen ankrajın 50 kN ile 90 kN arasında değişen bir çekme kapasitesi sağladığını göstermiştir. Çalışmanın üçüncü fazında, önerilen sökülebilir ankraj sisteminin uygulanabilirliğini göstermek için değişen kompozitlik derecelerine sahip dört adet tam ölçekli kiriş numunesi test edilmiştir.

Kirişler tarafından sağlanan eğilme kapasitesinin, geleneksel rijit plastik analiz metodu olan stres blok analiz metodu kullanılarak hesaplanan kapasiteler ile benzer olduğu belirlenmiştir. Önerilen sistemin pratikte ve saha koşullarında uygulanabilirliğini gösteren kiriş testleri sonrasında, beton tabliyeler kolaylıkla demonte edilebilmiştir.

Anahtar Kelimeler: Kompozit Yapılar, Sürdürülebilir Yapılar, Sökülebilir Ankraj, Mekanik Ankraj, Deneysel İnceleme

To my family and beloved ones

ACKNOWLEDGMENTS

The person who deserves the greatest gratitude is the supervisor of this thesis, Prof. Dr. Cem Topkaya. During this thesis study, he showed inimitable support, wisdom, patience, guidance, trust, self-devotion, and encouragement.

Secondly, I want to show my gratitude to my family, friends, and the technical staff and academic members of the Civil Engineering Department at METU.

This study was funded by Scientific and Technological Research Council of Turkey (TÜBİTAK) under grant number 119M615.

TABLE OF CONTENTS

CHAPTERS

ABSTRACT v

ÖZ vii

ACKNOWLEDGMENTS x

TABLE OF CONTENTS xi

LIST OF TABLES xiv

LIST OF FIGURES xvi

1 INTRODUCTION 1

1.1 Steel-Concrete Composite Construction 1

1.2 Concept of Shear Connection in Composite Structures 3

1.3 Concept of Demountability in Shear Connections 5

1.4 Background of Demountable Shear Connectors 7

1.5 Objectives and Scope 32

1.6 Organization of the Thesis 34

2 PUSH-OUT TESTS 37

2.1 Test Setup 37

2.1.1 Details of Data Recording Instruments 41

2.2 Test Specimens 41

2.2.1 Design Parameters 42

2.2.2 Geometric and Material Properties 46

2.3 Test Results 49

2.3.1 Observed Failure Modes 50

2.3.2 Load-Slip Response 53

2.3.3 Recommendations for Capacity Prediction 80
3 PULL-OUT TESTS 83
3.1 Test Setup 83
3.1.1 Orientation of Data Recording Instruments 86
3.2 Test Specimens 86
3.2.1 Design Parameters 87
3.2.2 Geometric and Material Properties 89
3.3 Test Results 90
3.3.1 Observed Failure Modes 90
3.3.2 Behavior Under Tensile Load 93
4 BEAM BENDING TESTS 99
4.1 Test Setup 99
4.1.1 Details of Data Recording Instruments 101
4.2 Test Specimens 102
4.2.1 Design Parameters 102
4.2.2 Geometric and Material Properties 104
4.3 Test Results 108
4.3.1 Elastic Loading Tests 109
4.3.1.1 Load-Deflection Behaviors 109
4.3.1.2 Load-Slip Behaviors 113
4.3.1.3 Strain Distributions 122
4.3.2 Ultimate Loading Tests 129
4.3.2.1 Load-Deflection Behaviors 129
4.3.2.2 Load-Slip Behaviors 133

4.3.2.3 Mode of Failures 137
4.3.3 Comparison of Experimental Results with Predicted Capacities ... 139
4.3.3.1 Comparison of Elastic Deflections 139
4.3.3.2 Comparison of Capacities 142
4.3.4 Demountability 147
5 SUMMARY, CONCLUSION, AND RECOMMENDATIONS FOR FUTURE WORK 149
5.1 Summary 149
5.2 Conclusions 149
5.2.1 Conclusions related with Push-out Tests 149
5.2.2 Conclusions related with Pull-out Tests 150
5.2.3 Conclusions related with Beam Bending Tests 150
5.3 Recommendations for Future Work 151
REFERENCES 153

LIST OF TABLES

TABLES

Table 2.1: Experiment matrix for push-out specimens 45
Table 2.2: Specimen nomenclatures 45
Table 2.3: Angle section dimensions 47
Table 2.4: Material properties of angle sections and base plate 48
Table 2.5: Material properties of bolts 49
Table 2.6: Failure mode of each specimen 52
Table 2.7: Initial stiffness of each specimen 54
Table 2.8: Applied loads at 3, 6, 9, and 12 mm and ultimate load capacity 74
Table 2.9: Comparison with channel connectors 79
Table 2.10: Series 1 - average load, ST, and COV 80
Table 2.11: Series 2 - average load, ST, and COV 81
Table 2.12: Comparison of series – 6 mm 81
Table 2.13: Comparison of series – 3 mm 82
Table 2.14: Comparison of series – 9 mm 82
Table 3.1: Experiment matrix for pull-out specimens 88
Table 3.2: Specimen nomenclatures 88
Table 3.3: Concrete cone strength of specimens 91
Table 3.4: Comparison between capacities and errors 91
Table 3.5: Maximum load and displacements 98
Table 4.1: Experiment matrix for beam bending specimens 103
Table 4.2: Specimen nomenclatures 103
Table 4.3: IPE300 section dimensions 105
Table 4.4: Material properties of I-section 106
Table 4.5: Back calculated degrees of composite actions 107
Table 4.6: Specimen 1 maximum and residual midspan deflections 112
Table 4.7: Specimen 2 maximum and residual midspan deflections 112

Table 4.8: Specimen 3 maximum and residual midspan deflections 113
Table 4.9: Specimen 4 maximum and residual midspan deflections 113
Table 4.10: Specimen 1 maximum and residual end slips 116
Table 4.11: Specimen 2 maximum and residual end slips 117
Table 4.12: Specimen 3 maximum and residual end slips 117
Table 4.13: Specimen 4 maximum and residual end slips 117
Table 4.14: Specimen 1 left half maximum and residual slips 118
Table 4.15: Specimen 1 right half maximum and residual slips 119
Table 4.16: Specimen 2 left half maximum and residual slips 119
Table 4.17: Specimen 2 right half maximum and residual slips 120
Table 4.18: Specimen 3 left half maximum and residual slips 120
Table 4.19: Specimen 3 right half maximum and residual slips 121
Table 4.20: Specimen 4 left half maximum and residual slips 121
Table 4.21: Specimen 4 right half maximum and residual slips 122
Table 4.22: Specimen 1 strain distributions 122
Table 4.23: Specimen 2 strain distributions 123
Table 4.24: Specimen 3 strain distributions 123
Table 4.25: Specimen 4 strain distributions 123
Table 4.26: NA (Neutral Axis) locations measured from the bottom flange 128
Table 4.27: Maximum and residual deflections of all specimens 132
Table 4.28: Maximum and residual end slips of all specimens 136
Table 4.29: Left half maximum and residual slips of all specimens 137
Table 4.30: Right half maximum and residual slips of all specimens 137
Table 4.31: Elastic loading - theoretical vs. experimental deflections with errors 141
Table 4.32: Maximum and permanent midspan deflections of specimens 144
Table 4.33: Modified maximum loads 145

LIST OF FIGURES

FIGURES

Figure 1.1: Example of a steel-concrete composite beam 2
Figure 1.2: Non-composite and composite beam (Loqman et al., 2018) 3
Figure 1.3: a) Non-composite, b) Fully-composite, c) Partially-composite beam comparison (Azad et al., 2017)..... 4
Figure 1.4: Example of a demountable shear connector (Biswas, 1986) 8
Figure 1.5: Used post-installed shear connectors: (a) Double nut bolt (DBLNB), (b) High-tension friction grip bolt (HTFGB), (c) Adhesive anchor (HASAA) Kwon et al. (2009)..... 8
Figure 1.6: Offered shear connectors: a) Friction-grip bolt, b) Bolt without embedded nut, c) Single embedded nut, d) Double embedded nut (Pavlović et al., 2013) 10
Figure 1.7: Demountable anchorage (Moynihan & Allwood, 2014) 11
Figure 1.8: Steel-precast concrete shear connections (Chen et al., 2014) 12
Figure 1.9: Shear connectors: (a) Type 1 blind bolt, (b) Type 2 blind bolt, (c) Traditional headed stud (Ban et al., 2015) 13
Figure 1.10: Shear connectors: (a) S1, (b)S2, (c)S3 (Dai et al., 2015)..... 14
Figure 1.11: Three types of connectors (Rehman et al., 2016) 14
Figure 1.12: Used shear connectors: (a) Headed stud (b) High-strength friction grip bolt (HSFGB) (Liu et al., 2016) 15
Figure 1.13: Offered blind bolts (BB) : (a) BB1, (b) BB2 (Pathirana et al., 2015). 17
Figure 1.14: Investigated connectors (Liu et al., 2017)..... 18
Figure 1.15: Innovative connector (Suwaed & Karavasilis, 2017) 19
Figure 1.16: Demountable steel-UHPC section (Wang et al.,2017) 20
Figure 1.17: Demountable shear connectors: (a) Friction bolts with cast in cylinders (P3), (b) Embedded coupler device (P15) (Odenbreit & Kozma, 2019)..... 21
Figure 1.18: Configurations of the connectors: (a) Type 1: Double-nut bolt, (b) Type 2: HSFGTB, (c) Type 3: Adhesive anchor, (d) Type 4: HSFGB, (e) Headed stud bolt, (f) Suggested novel bolted connector Yang et al. (2018)..... 22

Figure 1.19: Investigated bolted shear connectors (Ataei et al., 2019)..... 24
Figure 1.20: Suggested connector: (a) 3D view, (b) longitudinal view, and deformed shape (Feidaki et al., 2019) 25
Figure 1.21: Test setup and instrumentation (Sencu et al., 2019)..... 27
Figure 1.22: Connector types: (a) AJAX ONESIDE, (b) Machined demountable headed stud, (c) Lindapter hollo-bolt (Tan et al., 2019) 29
Figure 1.23: Beam with demountable connectors suggested (L. Wang et al., 2019) 30
Figure 1.24: WDSC: (a) Tube and stud, (b) Tube 3D cute, (c) cross-sectional view (Suwaed et al., 2022) 32
Figure 1.25: The proposed demountable shear connector 34
Figure 2.1: Test setup..... 38
Figure 2.2: Photos of the test setup: a) General view, b) Lateral support system, c) Clamping mechanism and loading plate, d) LVDTs..... 39
Figure 2.3: Orientation of LVDTs 41
Figure 2.4: Reinforcement layout 42
Figure 2.5: Bolts used (left – M20, right – M24)..... 43
Figure 2.6: Loading directions..... 44
Figure 2.7: Stress versus strain diagram for angles 48
Figure 2.8: Failure mode of specimen 2 (Bolt shear-off & cracking of concrete).. 50
Figure 2.9: Failure mode of specimen 5 (Tilting of connector)..... 51
Figure 2.10: Failure mode of specimen 9 (connector shear-off & crushing of concrete)..... 51
Figure 2.11: Load vs slip behavior of specimen 1 53
Figure 2.12: Effects of the bolt properties – L100x10..... 55
Figure 2.13: Effects of the bolt properties - L75x8..... 56
Figure 2.14: Effects of the bolt properties - L70x7..... 56
Figure 2.15: Effects of the bolt properties - L60x6..... 57
Figure 2.16: Effects of the bolt properties - L100x10..... 57
Figure 2.17: Effects of the bolt properties - L75x8..... 58

Figure 2.18: Effects of the bolt properties - L60x6 58
Figure 2.19: Effects of the angle size - M24 - 10.9 bolt 59
Figure 2.20: Effects of the angle size - M24 - 8.8 bolt 60
Figure 2.21: Effects of the angle size - M20 - 10.9 bolt 60
Figure 2.22: Effects of the angle size - M20 - 8.8 bolt 61
Figure 2.23: Effects of the angle size - M24 - 8.8 bolt 61
Figure 2.24: Effects of the angle size - M20 - 10.9 bolt 62
Figure 2.25: Effects of the angle size - M20 - 8.8 bolt 62
Figure 2.26: Specimen 13 (threads excluded) and specimen 21 (threads included) comparison 64
Figure 2.27: Specimen 2 (threads excluded) and specimen 22 (threads included) comparison 64
Figure 2.28: Specimen 3 (threads excluded) and specimen 23 (threads included) comparison 65
Figure 2.29: Specimen 4 (threads excluded) and specimen 24 (threads included) comparison 65
Figure 2.30: Specimen 1 (front loading) and specimen 17 (back loading) comparison 66
Figure 2.31: Specimen 5 (front loading) and specimen 18 (back loading) comparison 67
Figure 2.32: Specimen 9 (front loading) and specimen 19 (back loading) comparison 67
Figure 2.33: Specimen 17 (back loading) and specimen 20 (back loading) comparison 68
Figure 2.34: Specimen 2 (C1) and specimen 28 (C2) comparison 69
Figure 2.35: Specimen 3 (C1) and specimen 25 (C2) comparison 69
Figure 2.36: Specimen 4 (C1) and specimen 31 (C2) comparison 70
Figure 2.37: Specimen 6 (C1) and specimen 29 (C2) comparison 70
Figure 2.38: Specimen 7 (C1) and specimen 26 (C2) comparison 71
Figure 2.39: Specimen 8 (C1) and specimen 32 (C2) comparison 71

Figure 2.40: Specimen 14 (C1) and specimen 30 (C2) comparison 72
Figure 2.41: Specimen 15 (C1) and specimen 27 (C2) comparison 72
Figure 2.42: Specimen 16 (C1) and specimen 33 (C2) comparison 73
Figure 2.43: Loads at 3 mm slip of specimens with C1 concrete quality (angle size effect) 75
Figure 2.44: Loads at 6 mm slip of specimens with C1 concrete quality (angle size effect) 75
Figure 2.45: Ultimate capacities of specimens with C1 concrete quality (angle size effect) 76
Figure 2.46: Loads at 3 mm slip of specimens with C1 concrete quality (bolt property effect) 77
Figure 2.47: Loads at 6 mm slip of specimens with C1 concrete quality (bolt property effect) 77
Figure 2.48: Ultimate capacities of specimens with C1 concrete quality (bolt property effect) 78
Figure 2.49: Maximum slip displacement of each specimen..... 79
Figure 3.1: Test setup..... 84
Figure 3.2: Photos of the test setup: a) General view - 1, b) General view - 2, c) During test - 1, d) During test - 2..... 84
Figure 3.3: Supporting leg top view 85
Figure 3.4: Orientation of LVDTs 86
Figure 3.5: Reinforcement layout 87
Figure 3.6: Specimen 1 (L75-30-85-M24-10) 89
Figure 3.7: Failure mode - phase 1 92
Figure 3.8: Failure mode - phase 2 92
Figure 3.9: Specimen 1 - load vs. pull-out displacement..... 93
Figure 3.10: Specimen 2 - load vs. pull-out displacement..... 94
Figure 3.11: Specimen 3 - load vs. pull-out displacement..... 94
Figure 3.12: Specimen 4 - load vs. pull-out displacement..... 95
Figure 3.13: Specimen 5 - load vs. pull-out displacement..... 95

Figure 3.14: Specimen 6 - load vs. displacement 96
Figure 3.15: Applied load vs. pull-out displacement curves of all specimens 97
Figure 4.1: Test setup 99
Figure 4.2: Photos of the test setup: a) General view, b) Rotation prevention system and LVDTs, c) Loading instruments, d) Strain gauges 100
Figure 4.3: Orientation of LVDTs and strain gauges 101
Figure 4.4: Reinforcement layout 102
Figure 4.5: Stress versus strain diagram for I-sections 106
Figure 4.6: Technical drawings of specimens 108
Figure 4.7: Twist of concrete deck 109
Figure 4.8: Specimen 1 - L75-100-10-NT-E - applied load vs. midspan deflection 110
Figure 4.9: Specimen 2 - L75-50-10-NT-E - applied load vs. midspan deflection 110
Figure 4.10: Specimen 3 - L75-25-10-2T-E - applied load vs. midspan deflection 111
Figure 4.11: Specimen 4 - L100-25-8-NT-I - applied load vs. midspan deflection 111
Figure 4.12: Specimen 1 - L75-100-10-NT-E - applied load vs. end slips 114
Figure 4.13: Specimen 2 - L75-50-10-NT-E - applied load vs. end slips 114
Figure 4.14: Specimen 3 - L75-25-10-2T-E - applied load vs. end slips 115
Figure 4.15: Specimen 4 - L100-25-8-NT-I - applied load vs. end slips 115
Figure 4.16: Specimen 1 strain distribution at 1TL 124
Figure 4.17: Specimen 1 strain distribution at 2TL 124
Figure 4.18: Specimen 1 strain distribution at 3TL 125
Figure 4.19: Specimen 2 strain distribution at 1TL 125
Figure 4.20: Specimen 2 strain distribution at 2TL 125
Figure 4.21: Specimen 2 strain distribution at 3TL 126
Figure 4.22: Specimen 3 strain distribution at 1TL 126
Figure 4.23: Specimen 3 strain distribution at 2TL 126

Figure 4.24: Specimen 3 strain distribution at 3TL 127
Figure 4.25: Specimen 4 strain distribution at 1TL 127
Figure 4.26: Specimen 4 strain distribution at 2TL 127
Figure 4.27: Specimen 4 strain distribution at 3TL 128
Figure 4.28: Specimen 1 - L75-100-10-NT-E - applied load vs. midspan deflection 129
Figure 4.29: Specimen 2 - L75-50-10-NT-E - applied load vs. midspan deflection 130
Figure 4.30: Specimen 3 - L75-25-10-2T-E - applied load vs. midspan deflection 130
Figure 4.31: Specimen 4 - L100-25-8-NT-I - applied load vs. midspan deflection 131
Figure 4.32: Applied load vs. midspan deflection curves of all specimens..... 132
Figure 4.33: Specimen 1 - L75-100-10-NT-E - applied load vs. end slips..... 133
Figure 4.34: Specimen 2 - L75-50-10-NT-E - applied load vs. end slips..... 134
Figure 4.35: Specimen 3 - L75-25-10-2T-E - applied load vs. end slips..... 134
Figure 4.36: Specimen 4 - L100-25-8-NT-I - applied load vs. end slips..... 135
Figure 4.37: Applied load vs. average end slip curves of all specimens 136
Figure 4.38: Beam specimen failure: a) Permanent deflection, b) Yielding at midspan, c) Bolt shear-off, d) Concrete crushing and cracks 138
Figure 4.39: Mn vs. composite ratio 143
Figure 4.40: Applied load vs. composite ratio 144
Figure 4.41: Mn vs. composite ratio with experimental values 146
Figure 4.42: Applied load vs. composite ratio with experimental values..... 146
Figure 4.43: Demounting of a concrete deck from steel beam 147

CHAPTER 1

INTRODUCTION

1.1 Steel-Concrete Composite Construction

In civil engineering practice, steel and concrete are widely used materials. Steel and concrete have some advantages and disadvantages over each other. To illustrate, steel structures are generally lighter, stiffer, easy to fabricate and install, and more ductile. On the other hand, concrete structures are cheaper, more durable, strong against compression, and resistant to fire and weather conditions.

Composite construction is a comprehensive term used to define any structure that involves different materials. The main reasons to prefer composite construction are increased strength, aesthetics, and sustainability. Considering the properties mentioned above, the idea of composite construction comes into the civil engineering scheme. In civil engineering practice, the most common composite construction is the usage of steel and concrete together to utilize the compressive strength of concrete and the tensile strength of steel.

In composite construction, reinforced concrete is typically cast on top of profiled steel decking (re-entrant or trapezoidal), which eliminates the need for falsework and formwork. The depth of the slab varies from 100 mm to 300 mm. Slabs are most commonly made of concrete because of its mass and properties, which may be used to decrease floor deflections and vibrations while also providing fire protection and thermal storage. Additionally, the concrete slab supports the steel section laterally, which prevents the steel section’s most common failure mode of lateral-torsional buckling. Steel is utilized as the slab's supporting system because of its better strength-to-weight and stiffness-to-weight ratios, as well as its simplicity of handling. With the usage of steel and concrete together, the weight of the structure may be reduced by up to 25%, the span of the structure may be increased without the

need for intermediate columns compared to concrete structures, and the construction duration may be reduced.

An example of a steel-concrete composite beam is given in Figure 1.1. The concrete slab is reinforced and cast in-situ on the profiled metal deck. The connection between the concrete slab and the steel beam is provided by the shear connectors shown and will be explained in Chapter 1.2.

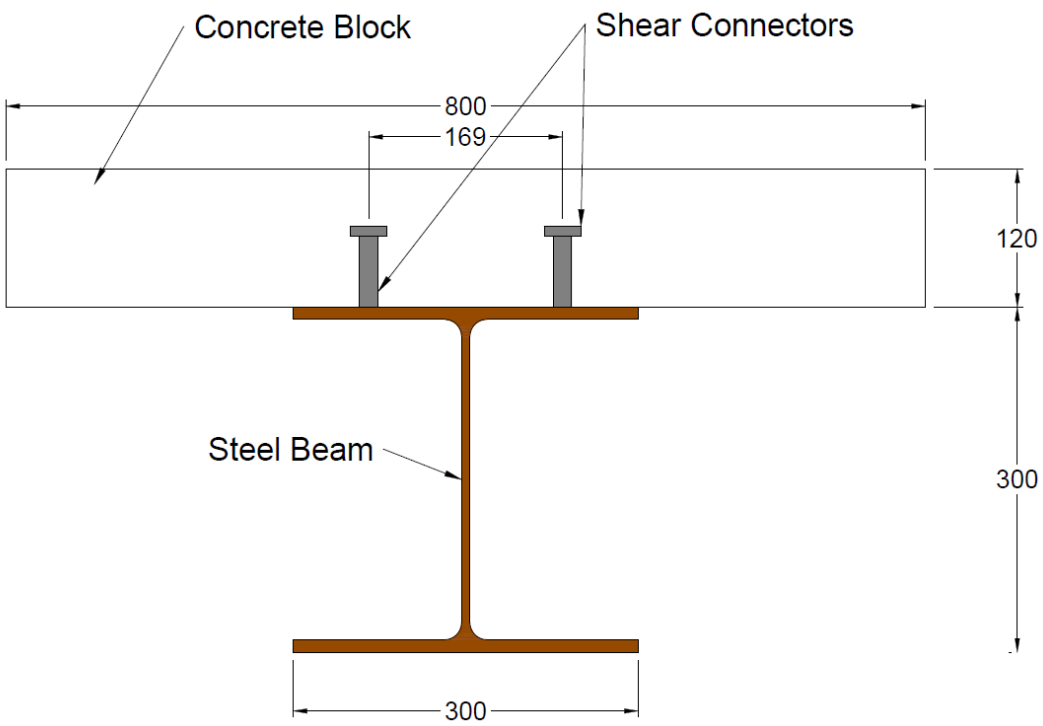

Figure 1.1: Example of a steel-concrete composite beam

Over a century ago, composite construction was first used in the design of both a building and a bridge in the United States. The use of steel and concrete for flexural elements was common in the early types of composite structures, and longitudinal slip between these elements was detected. The first kind of composite construction is composite steel-concrete beams. An American engineer devised a patent for shear connections at the top flange of a universal steel section to avoid longitudinal slipping in the United States. This was the start of the development of totally

composite steel and concrete systems and the concept of shear connection in composite structures.

1.2 Concept of Shear Connection in Composite Structures

The strength of composite structures depends on the contribution of the different materials included. In steel-concrete composite members, concrete contributes to compression, and steel contributes to tension capacity, as mentioned. Under bending, shear forces arise at the interface of these elements of the composite member. The shear forces between steel and concrete cause the slipping of materials from each other, which causes materials to act independently. When the members act independently, the capacity of the composite member cannot reach its maximum, and the member becomes non-composite. In order to prevent the slip, there is a need for connectors to carry the shear forces at the interface, as shown in Figure 1.2.

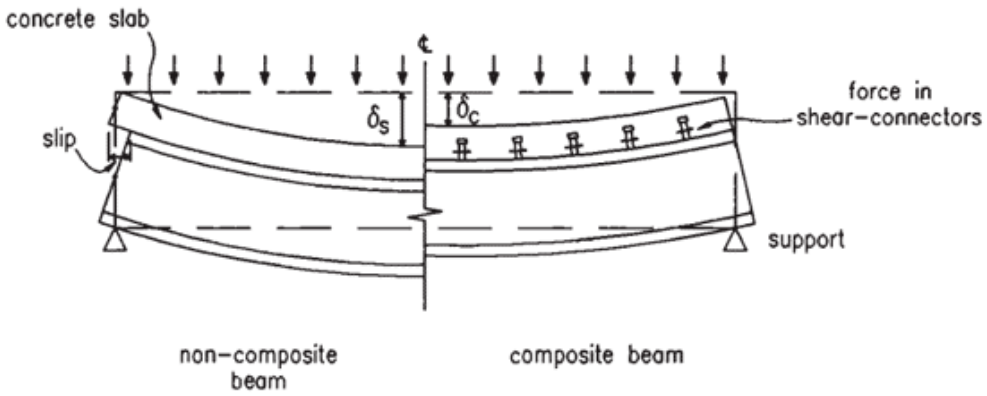

Figure 1.2: Non-composite and composite beam (Loqman et al., 2018)

The elements that connect steel and concrete and carry the shear forces are named shear connectors (also known as mechanical anchorages). The existence of shear connectors allows higher stiffness and higher load-carrying capacity in comparison to non-composite beams. As the slip between the materials decreases, the degree of the composite action increases, as shown in Figure 1.3. The degree of the composite action depends on the number of shear connectors included in the design, e.g.,

increasing the number of shear connectors increases the degree of composite action up to 100%.

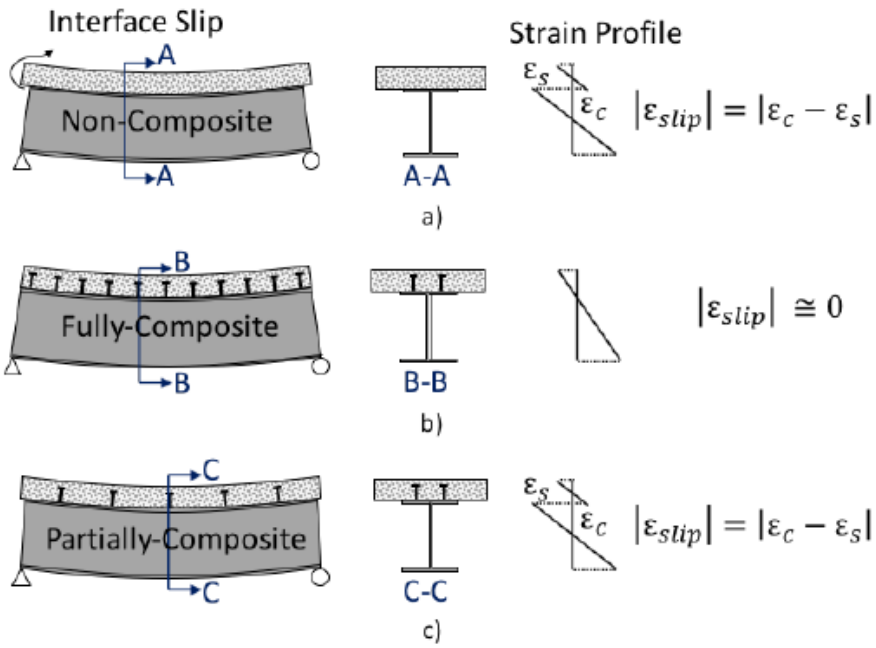

Figure 1.3: a) Non-composite, b) Fully-composite, c) Partially-composite beam comparison (Azad et al., 2017)

The main requirements that shear connectors have to fulfill are transferring the direct shear at their base, creating tensile links into the concrete, and being economical and available on the market. Due to the economic measures, partially-composite behavior is generally preferred over fully-composite behavior.

The load-carrying mechanism of shear connectors is similar to the dowel action observed in cracked reinforced concrete section reinforcements. Liberati et al. (2016) describe the dowel action as an action that is a complementary shear strength mechanism associated with reinforced cracked concrete. When cracks form and cut across longitudinal reinforcements, this shear-load transfer mechanism occurs, increasing the mechanical shear strength. The shear loads are then transferred to the reinforcements by the crack lips. As a result, there is local bending and shear at the reinforcements. Some structural components, such as beams with little or no shear

reinforcements, can benefit from the dowel action by increasing structural shear strength and post-peak ductility.

As mentioned by Tan et al. (2019), steel-concrete connections must resist uplift forces as well as shear forces in some applications, such as composite coupling beams and infill walls. As a result, experimental testing to determine the performance of steel-concrete connections under combined loading is required. To understand the behavior and load-carrying mechanism of shear connectors, push-out, pull-out, and beam bending experiments are needed. Definitions of push-out, pull-out, and beam bending experiments will be given in Chapter 2, Chapter 3, and Chapter 4, respectively.

1.3 Concept of Demountability in Shear Connections

To achieve composite action between steel section and concrete deck, mechanical anchorages are used in the steel-concrete interface. Although various types of anchorages have been developed to date, the traditional welded headed shear stud is the most common type of anchorage mainly employed in many composite components due to the advantages they offer.

Because of the damages that occurred to the concrete slab of composite beams caused by weather conditions and other external factors, there is a requirement for replacement of the concrete deck at certain intervals. Additionally, many medium-rise structures consisting of composite load-carrying systems in countries such as England and Australia, where composite systems are commonly used, have faced the need for demolition in the last ten years due to changes in urban land use. In terms of recycling, structural steel is a reusable building material, but due to the welded connection provided by the traditional headed studs, steel sections are linked to a concrete deck that cannot be easily disassembled and reused. Deconstruction of traditional composite beams is expensive, energy-intensive, and environmentally harmful.

The potential to maintain or support any activities without consumption of resources or production of wastes is called sustainability. Sustainability is important in civil engineering to reduce constructional carbon footprint and prevent climate change caused by material waste. In composite structures, sustainability can be applied by the reuse of steel members. However, the usage of traditional headed shear studs prevents the recyclability of steel members, which brings the idea of providing demountability at the connection of steel and concrete members. Demountability may be defined as having the ability to be removed from its setting, being designed to be dismantled or detached.

The need for demountable bridge decks is explained by Suwaed & Karavasilis (2017) and Eckelman et al. (2018). Many bridges in Europe are damaged by many external factors such as weather conditions and crashes, and the same is valid in the United States, where one-third of the 607,380 bridges need to be repaired. Bridge maintenance ensures the bridge's serviceability as well as the safety of its users by inspecting, repairing, reinforcing, or replacing the entire bridge or parts of it. Direct economic losses (e.g., material and labor expenses) as well as indirect socioeconomic losses (e.g., travel delays, longer travel distances, poor movement of commodities, and business interruption) occur from such activities. Indirect losses, which can be several times larger than direct losses depending on the kind of bridge and the scope of maintenance activities, are a major concern for bridge owners, decision-makers, and bridge engineers.

In recent years, a limited number of researches is done to study the use of high-strength bolts as composite member’s mechanical anchorages and to design innovative demountable anchorages. According to the findings of these studies, high-strength bolts have similar strengths as traditional welded headed studs and can be demounted. These anchorages, on the other hand, have several drawbacks, such as low stiffness, high cost, and difficulty in being used in modular construction, where a precast concrete deck is united with a steel section to reduce concrete placing operations on the building site. Further information related to this topic will be given in Chapter 1.4.

1.4 Background of Demountable Shear Connectors

The concept of demountable shear connectors started with the use of high-strength bolts as mechanical anchorages. The first experimental study about the issue is conducted by Dallam & Harpster (1968). In this study, friction-grip bolts were used as shear connectors in composite design without any attempt to provide demountability in composite beam tests. According to the results, friction-grip bolts succeeded in providing the necessary rigid connection between the concrete slab and steel girder and reserve capacity sufficient to develop the ultimate moment capacity needed in the fully-composite design. Consecutively, a research was conducted by Dallam (1969). The same anchorage system of Dallam & Harpster (1968) is used in push-out tests to record the load-slip behavior and measure the direct shear capacity of friction-grip bolts. In the design of push-out specimens, bolts were pretensioned. The major findings of the project are observation of no loss in prestress with time in high-quality concrete, measurement of the capacity of bolts about to be twice that of headed studs, and observation of practically zero slip in the service load range. Later on, Biswas (1986) focused on the rehabilitation of bridge decks, i.e., the repair or replacement of concrete decks used in highway bridges. The connection design shown in Figure 1.4 is applied to rehabilitate the Rondout Creek Bridge in New York. The offered connection design was composed of a high-strength bolt welded to a steel girder and can be demounted by screwing off the nut that is located over the concrete deck.

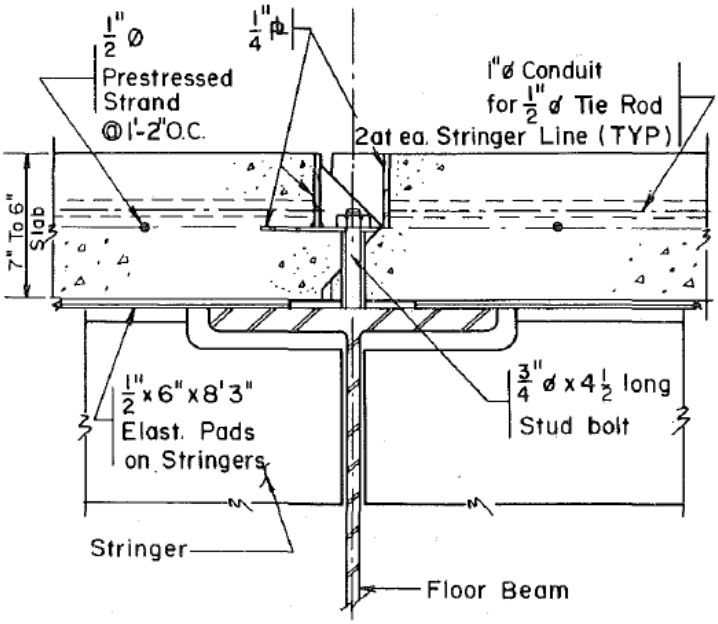

Figure 1.4: Example of a demountable shear connector (Biswas, 1986)

Studies about the retrofitting of the bridges are continued with research by Kwon et al. (2009) and a case study of the same bridge by Kwon et al. (2010)a. In these studies, the main focus was developing composite action in existing non-composite bridge girders. While developing the composite action, shear connectors were designed to be suitable for demountability. Thus, an increase in load-carrying capacity and the ability to replace the concrete deck were granted. Three different post-installed shear connectors were used in retrofitting bridge girders, are shown in Figure 1.5.

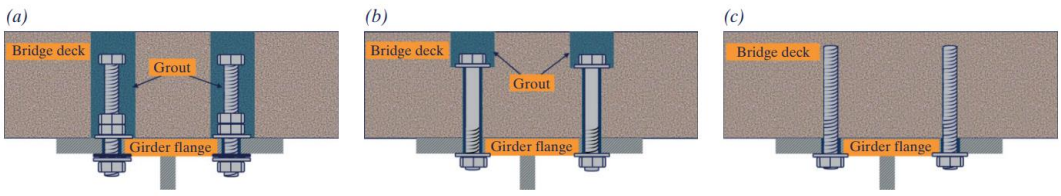

Figure 1.5: Used post-installed shear connectors: (a) Double nut bolt (DBLNB), (b) High-tension friction grip bolt (HTFGB), (c) Adhesive anchor (HASAA) Kwon et al. (2009)

DBLNB and HASAA type connectors used ASTM-A193 (2004) B7 threaded rods for transferring the shear forces; meanwhile, HTFGB type connectors used ASTM-A325 (1986) high-strength bolts. In all types, top flanges of the steel beams were drilled, connectors were pretensioned, and holes were filled with grout. The findings of these studies show that adding a minimal number of post-installed anchorages may greatly increase the stiffness and strength of existing non-composite bridges. Using partial composite design principles and mechanical anchorages with high fatigue strength, the number of post-installed shear connectors required to strengthen a girder may be reduced. The behavior of the shear connectors shown in Figure 1.5 under static and fatigue loading and the experimental behavior of retrofitted bridges were investigated by Kwon et al. (2010)b and Kwon et al. (2011). Direct-shear push-out and single-point loading beam bending experiments were conducted. According to experiment results, the shear strength of the connectors is higher than the shear strength of the traditional headed studs, and the capacity is approximately one-half of their tensile strength. The fatigue strength of investigated shear connectors is higher than the traditional headed shear stud. Application of post-installed shear connectors with only a 30% degree of composite (i.e., shear-connection ratio) action increases the load-carrying capacity of the girders on the order of 40-50% compared to non-composite girders. Consecutively, a parametric finite element (FE) study related to offered shear connectors was conducted by Kwon et al. (2012). ABAQUS (2012) finite element software was used in the development of the models. The considered variables of the study were beam depth, span length, and degree of composite action. The results showed that a minimum 30% shear-connection ratio is needed for satisfactory behavior.

In the following research related to demountable shear connectors, four new connectors were offered by Pavlović et al. (2013), and the application of the offered connectors with prefabricated decks was investigated by Pavlović et al. (2014). The offered connectors are shown in Figure 1.6. Push-out experiments and finite element analysis with ABAQUS (2012) software were conducted to investigate the behavior of connectors.

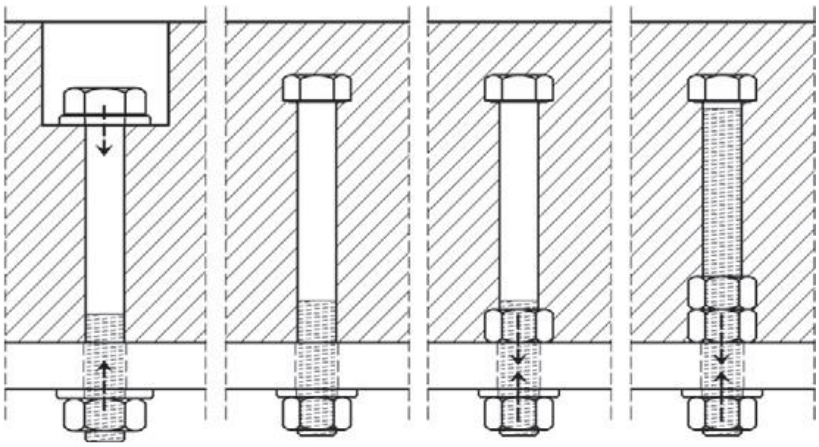

Figure 1.6: Offered shear connectors: a) Friction-grip bolt, b) Bolt without embedded nut, c) Single embedded nut, d) Double embedded nut (Pavlović et al., 2013)

According to the result of the studies, the initial stiffness of the connectors is reduced to 50% compared to traditional welded studs. Slips at the failure of the connectors are above 6 mm, which fulfills the ductility requirements given in the codes. In addition, observations show the suitability of connectors for use with prefabricated concrete slabs.

Load-carrying mechanism of the demountable shear connectors was studied by Rowe & Bradford (2013). A simple physical model was constructed to illustrate the concept. The characteristics of the mechanism were found to be initially being enforced by full shear interaction; after exceedance of the frictional resistance by interface shear, parts of the beam have zero interaction, and with the start of bolt bearing against their holes, parts of the beam have partial shear interaction. The mechanism was assessed and compared with the experiments.

Moynihan & Allwood (2014) investigated the behavior of an alternative demountable anchorage. The anchorage is a machined form of the traditional headed stud, as shown in Figure 1.7.

Figure 1.7: Demountable anchorage (Moynihan & Allwood, 2014)

Three composite beams were prepared with a length of 2 m, 10 m, and 5m and tested in three-, six- and four-point bending, respectively. After achieving service loads, the specimens with 2- and 10-meter lengths were disassembled and reassembled to prove the demountable behavior. The results show that the load-carrying capacity of all three beams is higher than the predicted capacity using Eurocode 4 (2011).

Composite girders with steel and precast members connected using through-bolt shear connectors were studied by Chen et al. (2014). Effect of bolt diameter, bolt pretension, and steel-concrete contact surface properties were investigated under static loading to understand the girder behavior. The connection types and shear connectors are shown in Figure 1.8. A finite element model was constructed to simulate the load-slip response of a full-scale bridge girder using the experimental data obtained from push-out tests. As a result, the through-bolt connectors showed lower initial slip load but approximate ductility and peak load-carrying capacity compared to the traditional headed studs. The initial slip and ultimate load of the connector can be increased with the application of higher pretension forces. The change of contact surface properties between steel and concrete did not show any effect. The FE analysis demonstrated that the offered shear connectors could be used in the composite girder design, and the number of connectors needed can be reduced compared to headed studs.

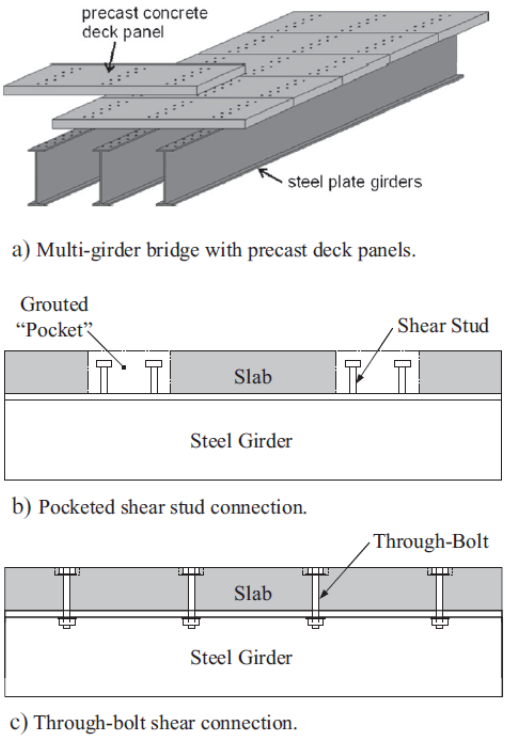

Figure 1.8: Steel-precast concrete shear connections (Chen et al., 2014)

The use of blind bolt connectors as mechanical anchorages was investigated by Ban et al. (2015), Henderson et al. (2015)a, and Henderson et al. (2015)b. To understand the time-dependent behavior under sustained loads, four long-term full-scale beam and short-term push-out specimens with the blind bolt shear connectors, shown in Figure 1.9, were tested. A three-dimensional FE model was constructed, and the long-term effects were simulated by defining a viscoelastic response. According to the results, the FE model was found adequate for predicting time-dependent behavior. The initial stiffness value of connectors was found to be lower than the traditional headed studs; however, in a time-dependent manner, this is beneficial to some extent. For composite beams with blind bolts, greater bolt-to-hole clearance can significantly lower the deflection ratio over time. Additionally, the time-dependent deflection of composite beams may be reduced with the existence of compressive reinforcement.

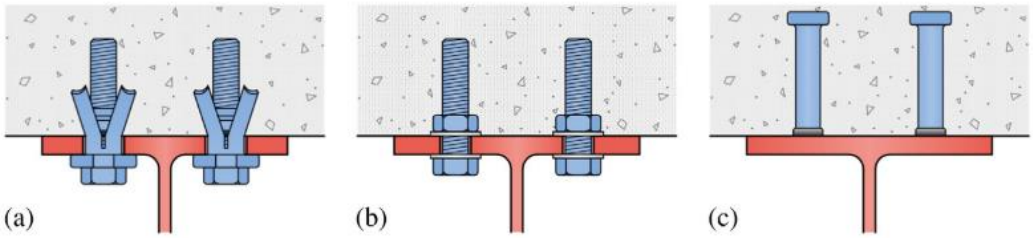

Figure 1.9: Shear connectors: (a) Type 1 blind bolt, (b) Type 2 blind bolt, (c) Traditional headed stud (Ban et al., 2015)

The dynamic behavior of the proposed connectors was studied with material tests, push-out tests, and full-scale beam tests. The results of push tests inferred that the two shear connection types had varying stiffness values, with the Type 1 connector having a higher stiffness value than both the Type 2 and the welded headed stud. The stiffness values of Type 1 and Type 2 connectors are comparable to the value of traditional headed studs. Also, with the increase in stiffness of connectors, the natural frequency decreases. The specimens were modeled with a Timoshenko beam model with damping and an uncertain boundary condition. The results obtained from the model matched with experimental results.

Afterward, the studies related to the usage of a machined form of traditional headed studs as demountable shear connectors continued. A parametric study related to measuring the change in shear load-carrying capacity with the change of concrete strength and stud collar size was conducted by Dai et al. (2015). The tested specimens, which consist of the connectors shown in Figure 1.10, were easily demounted without any exceptions. The findings of the study showed that when the concrete quality changes from C20 to C60, the shear load-carrying capacity of connections with lower stud collar diameters increases considerably. Only, for the types of anchorages with concrete strengths less than C30, the shear capacity of connections may be limited by concrete slab crushing-splitting; otherwise, the shear load-carrying capacity of the offered demountable shear connectors is limited by stud collar strength, but still, concrete strength has a significant impact on ductility. An FE model was produced to estimate the capacity change with the effect of parameters. It was found that the produced FE model is applicable, and the simple

calculation methods provided in Eurocode 4 (2011), AISC (2016), and ACI are usable.

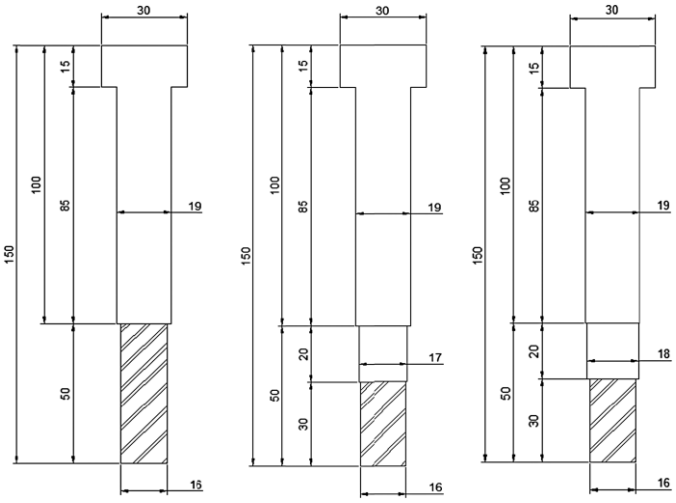

Figure 1.10: Shear connectors: (a) S1, (b)S2, (c)S3 (Dai et al., 2015)

The change of load-carrying capacity of demountable anchorages with the inclusion of profiled decking was studied by Rehman et al. (2016), Lam et al. (2017), and Rehman et al. (2018). A fully-threaded bolt and machined headed studs were used as shear connectors, as shown in Figure 1.11.

Figure 1.11: Three types of connectors (Rehman et al., 2016)

The use of the profiled deck is beneficial since it is the main alternative to formwork needed for cast-in-place concrete. Push-out tests conducted by Rehman et al. (2016) show that the ductility of the proposed demountable connections is high, and shear capacity and the behavior are similar to traditional headed studs, despite the lower initial stiffness. The arrangement of connectors is important to predict the behavior. The inclusion of a single connector per deck trough provides full-shear resistance; meanwhile, ductility increases with the inclusion of two connectors. The main failure modes of the connectors are fracture and crushing of the concrete. Full-scale beam bending tests conducted by Lam et al. (2017) and Rehman et al. (2018) show similar results, which are observations of low initial stiffness but high ductility. The initial stiffness of beam specimens may be increased by lowering the hole tolerance or increasing the bolt pretension. The ultimate capacity of the specimens can be predicted by plastic theory and is very close to composite slabs with traditional headed studs, which are not demountable.

The sustainability of structures with demountable shear connectors may be enhanced with the use of precast slabs with geopolymers. This idea was studied by Liu et al. (2015) and Ataei et al. (2016) experimentally and by Liu et al. (2016) numerically.

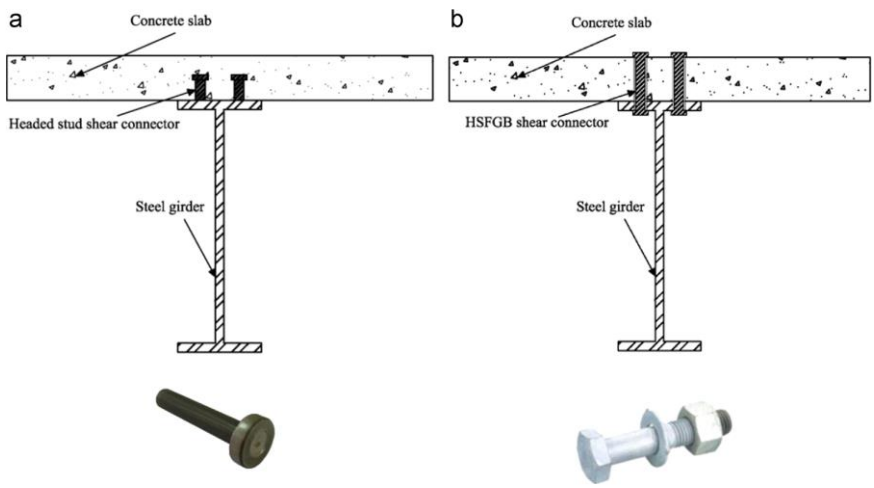

Figure 1.12: Used shear connectors: (a) Headed stud (b) High-strength friction grip bolt (HSFGB) (Liu et al., 2016)

The main parameters elucidated to investigate the ultimate strength and the load-slip characteristics of offered geopolymer concrete decked composite elements with HSFGB connections, shown in Figure 1.12, were the change in bolt pretension, hole clearance in the steel flange, bolt diameter and tensile strength, and the compressive strength of the concrete slab. The traditional headed studs were also tested similarly to HSFGB connectors to compare the data obtained for validation. The results of push-out tests and their numerical simulation with the models developed using ABAQUS (2012) software showed that the load-slip response of the HSFGB anchorages has three different regimes compared to traditional headed studs. Due to the pretensioned connection, the slip nearly dissipated during the early stages of loading. After the friction at the steel-concrete interface caused by the pretension of connection was overcome, the clearance between the prefabricated holes and the bolts caused substantial slip. The third behavior regime emerged once the bolt started to bear against the surface of the opening in the slab. According to the parametric study, the diameter and tensile capacity of the anchorage have an important impact on the shear load-carrying capacity of HSFGB connectors. According to beam tests, beams with HSFGB have slightly less load-carrying capacity but higher ductility than beams with conventional connections. The rotation and slip deflections of beams with precast panels localize the transfer of compression in the slab and, as a result, produce longitudinal splitting at loads exceeding the service load range. The constructed finite element model showed that the ultimate strength of the beam increases when the bolt spacing is reduced (i.e., increased number of bolts in the span). The strong shear resistance and slip capacity of the HSFGB shear connectors result in a composite beam with a low degree of shear connection having a substantially greater ultimate strength than its non-composite equivalent, with considerable ductility. Increasing the diameter of the prefabricated hole while having a fixed bolt size reduces the rigidity and ultimate load of the beam, especially for beams with excessive loads. The anchorages should be placed near the supports to optimize the performance of composite beams with oversized holes.

The bridge deck strengthening with the use of blind bolt shear connectors was studied by Pathirana et al. (2015) and Pathirana et al. (2016)b. Under retrofitting conditions, the load-slip behavior of blind-bolt and welded stud connections in grout was studied by Pathirana et al. (2016)a. The connection design used in these studies is shown in Figure 1.13.

Figure 1.13: Offered blind bolts (BB) : (a) BB1, (b) BB2 (Pathirana et al., 2015)

To investigate the feasibility of retrofitting the existing bridges with the use of blind bolt connectors, three composite and four non-composite specimens were prepared. Then, the three non-composite beams were retrofitted with the offered connections BB1, BB2, and traditional shear stud (as a control specimen). The results showed that in both normal and retrofitted scenarios, the BBs resisted much higher shear loads than the traditional headed stud. Approximately 85% of the slip capacity of the headed studs is obtained after the yielding of the connector; yet, BBs demonstrate much of their slip response without yielding. The specimen retrofitted with the headed stud showed lower load-carrying capacity compared with the normal composite beam with headed studs; meanwhile, both the retrofitted and normal specimens with BBs showed comparably similar strength and ductility. The use of BB2 connectors produces relatively lower stiffness compared with the other two beams. The parametric push-out study related to load-slip behavior of BBs showed that ultimate shear carrying capacity might be increased with the increase of the compressive strength of the grout. The embedded length of BBs is also important to determine the capacity. With the increase of the embedded length of the connectors,

BBs develop more shear capacity, although traditional headed studs show no appreciable change.

The inelastic moment redistribution after strengthening of existing non-composite girders using the connector shown in Figure 1.5c was studied by Liberati et al. (2016). Fatigue tests, shakedown tests, and ultimate-strength tests were conducted on retrofitted specimens. According to the results, post-installing shear connections and allowing for moment redistribution in continuous bridges can result in significant strength increases of up to 60%. Even at composite ratios below 30%, experimental testing of large-scale reinforced girders with post-installed shear connections revealed robust structural performance under elastic, fatigue, and ultimate strength loading.

The studies related to geopolymer concrete decked composite slabs with demountable connectors continued with research by Liu et al. (2017). In this study, different types of demountable connections, shown in Figure 1.14, were investigated both experimentally and numerically.

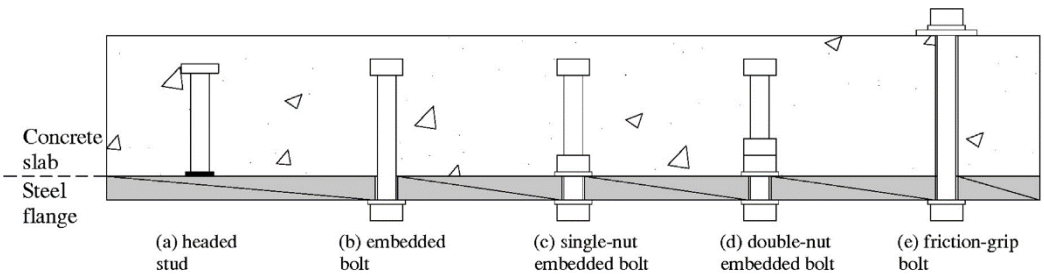

Figure 1.14: Investigated connectors (Liu et al., 2017)

All of the composite beam structural components, as well as their interactions, were modeled, and material non-linearity was considered in the model. The study was conducted using the quasi-static FE analysis tool of ABAQUS (2012) and its dynamic explicit technique. The findings of the FE analysis were compared to experimental data, revealing that the numerical model created is capable of precisely describing the behavior of the sustainable composite beams. The ultimate strengths of composite beams improve as the degree of partial shear connection increases,

according to parametric research based on FE modeling. Composite beams with larger diameter bolt shear connectors were preferred among those with the same degree of shear connection because of their favorable ductile performance and ease of manufacturing compared to a higher number of bolts with smaller sizes. The composition of the slab, whether it is geopolymer or ordinary concrete, had minimal effect on the reaction of the beam. The ultimate strength increased marginally when the concrete strength increased significantly as the steel yield strength increased. The parametric experiments revealed that, except for extremely tiny gaps, gaps between precast concrete panels during composite beam assembly should be avoided to prevent the considerable reductions in initial stiffness.

An innovative type of demountable shear connectors was presented by Suwaed & Karavasilis (2017) and Suwaed & Karavasilis (2018), as shown in Figure 1.15. High-strength bolts are used in the design of the connector, which are fastened to the top flange of the steel beam using a specific locking nut design that prevents bolts from slipping within their holes.

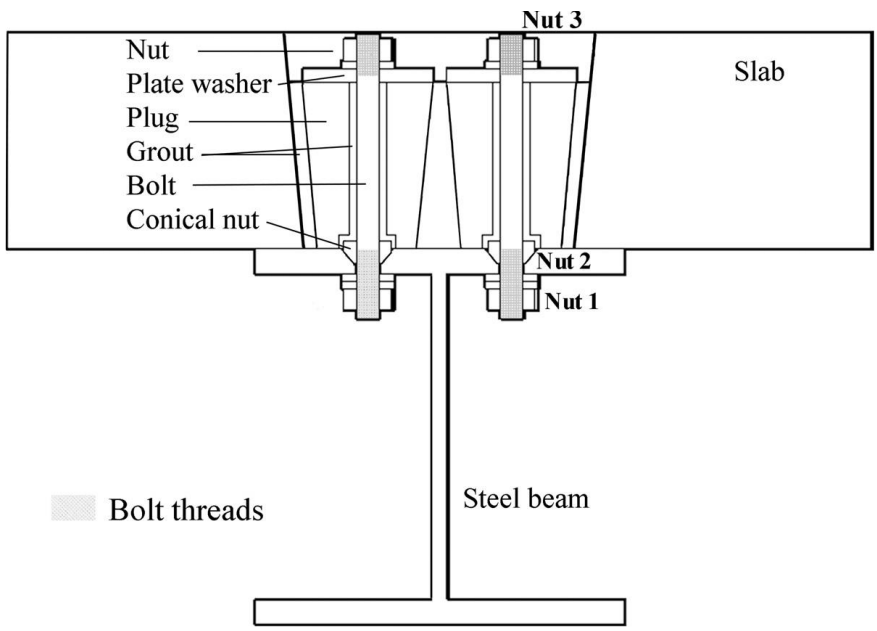

Figure 1.15: Innovative connector (Suwaed & Karavasilis, 2017)

The repetitive two series of push-out tests were conducted to illustrate the behavior of the connectors fully. The experiments showed that the locking nut shear connectors (LNSC) are suitable for disassembly. Compared to traditional head studs or previously suggested bolted shear connections, the LNSC has a very high shear resistance and stiffness, reducing the needed number of shear connectors and slab pockets. The LNSC has a high ductility which provides a large slip capacity of up to 14 mm. The frictional resistance can be raised by 29% when the bolt preload is increased by 40%.

The quality of the concrete used in the design of structures depends on the importance and type of the structure. Yi et al. (2012) explain that because of its superior safety, serviceability, durability, and economic advantages, ultra-high-performance concrete (UHPC) is now required to construct super-span bridges and mega-height high-rises. The behavior and the load-carrying capacity of the demountable headed stud shear connectors in the steel-UHPC composite structure were investigated by J. Y. Wang et al. (2017). A machined form of traditional welded headed studs was used as the demountable headed studs, and a cross-section of the composite body is given in Figure 1.16. The main parameters of the study were the stud diameter and the aspect ratio.

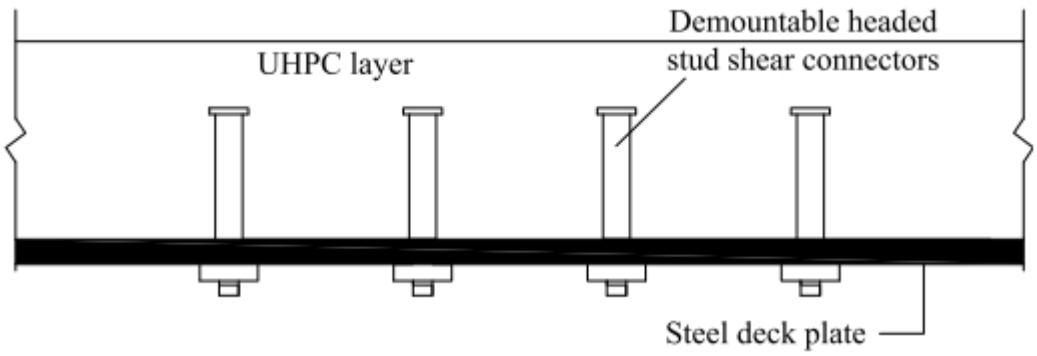

Figure 1.16: Demountable steel-UHPC section (Wang et al.,2017)

The failure modes observed during the experiments were UHPC breakout and stud fracture. The failure modes were found to be closely connected to the aspect ratio, with tensile failure owing to UHPC breakout occurring in specimens with an aspect

ratio of less than 1.5. It was found that the load-carrying capacity of the anchorages used was lower than the expected values, which caused the stud fracture. Investigation of the codes used showed that AASHTO (2014) LRFD, and Eurocode 4 (2011) overestimate the capacity of the demountable headed studs by 29% and 9%, respectively, whereas the Chinese code underestimates its value by 1%. The ultimate strength of the shear connections increases as the aspect ratio increases for specimens with the same stud collar diameter. The ductility of the demountable anchorages was higher than that of traditional welded ones, although it was still less than the Eurocode 4 (2011) ductility standard for shear connectors in regular strength concrete, which is 6 mm.

A novel demountable shear connection type was offered by Kozma et al. (2019) and Odenbreit & Kozma (2019). The components of the connection offered are prestressed and epoxy resin injection bolts, solid slabs, and composite slabs with profiled decking, as shown in Figure 1.17.

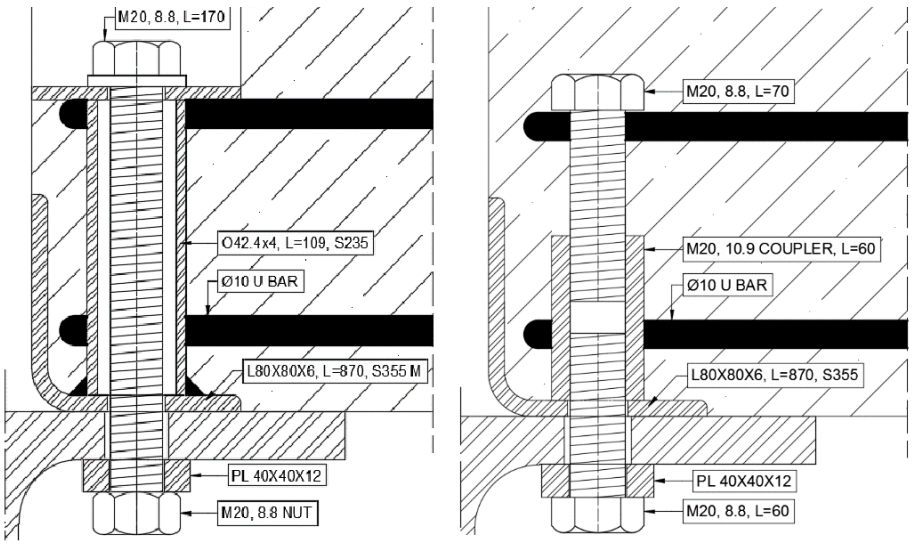

Figure 1.17: Demountable shear connectors: (a) Friction bolts with cast in cylinders (P3), (b) Embedded coupler device (P15) (Odenbreit & Kozma, 2019)

Fifteen push-out tests were conducted to investigate the behavior of the offered connectors experimentally. The results show that offered connections are robust and adequate for usage in the composite structure design. The position of the bolt affects

the load-slip curves. A strip of the solid slab above the flange is adequate to prevent the profiled steel sheeting from compromising the shear connection behavior. Larger hole tolerances can be represented with epoxy resin without resulting in a decrease in load-bearing capability where the application of connection to large deck components necessitates it.

An innovative demountable shear connector that consists of a short bolt, a long bolt, and a coupler was suggested by Yang et al. (2018). In this study, static push-out tests were implemented to understand the failure mode and the behavior of the suggested connection. Existing demountable connections suggested in the literature and traditional headed studs were also tested to compare the behavior and shear performance.

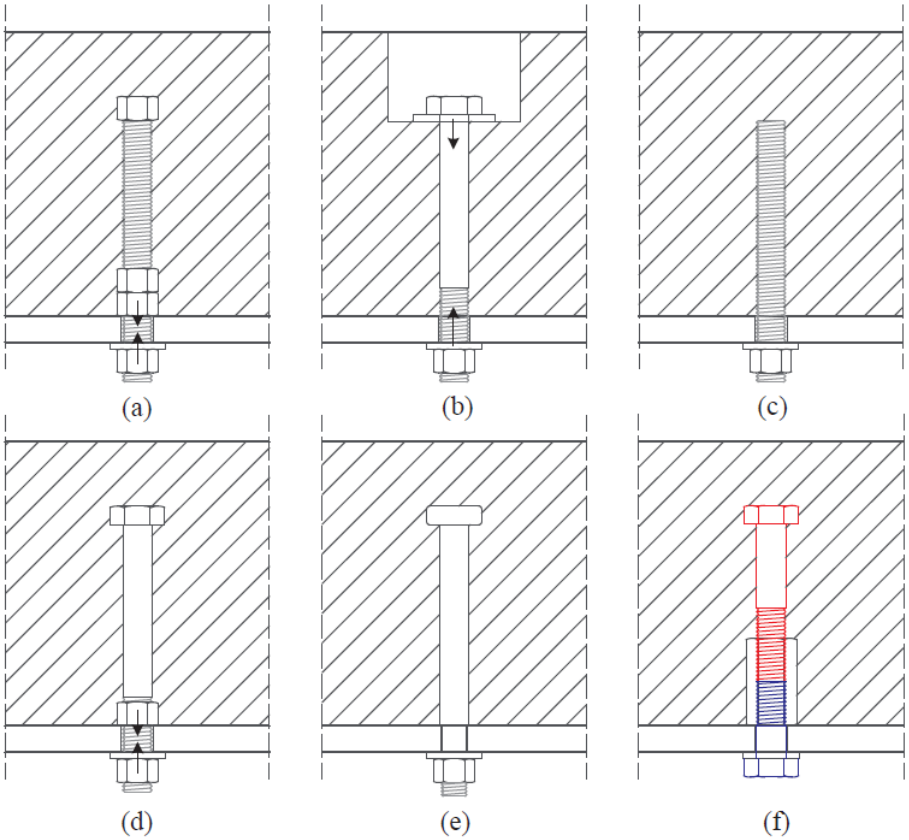

Figure 1.18: Configurations of the connectors: (a) Type 1: Double-nut bolt, (b) Type 2: HSFGTB, (c) Type 3: Adhesive anchor, (d) Type 4: HSFGB, (e) Headed stud bolt, (f) Suggested novel bolted connector Yang et al. (2018)

Four sets of bolted connection specimens with three diameters and two strength categories were used to investigate the shear performance of the suggested connector. Four sets of bolted connection specimens were evaluated and compared to 22 mm welded stud connector specimens in terms of failure mechanism, shear carrying capacity, load-slip curve, and shear stiffness. According to the study results, the short bolts were sheared off in four sets of bolted connection specimens. Following the fracture of the short bolts for each specimen, there were just a few minor cracks under the coupler with no local concrete crushing problem. The coupler embedded in the concrete increases the contact area between the bolt shank and the ambient concrete, lowering the local compressive stress of the concrete under the coupler. Grade 8.8 M22 bolted connection had approximately the same shear bearing capacity as a 22 mm conventional headed stud, while grade 8.8 M27 bolted connector has about 1.6 times the capacity of a 22 mm headed stud. Each bolted connection studied in this research has a shear capacity of 0.8 times the characteristic tensile strength of the bolt. The slip capacity of each bolted connection increases as the bolt diameter increases, while the grade of the bolts is kept at 8.8. Grade 8.8 M27 bolted connections have an average peak slip of 5.77 mm, which is closer to the minimum slip requirement of 6 mm.

The cyclic behavior of the existing bolted demountable connections suggested in the literature was investigated by Ataei et al. (2019). The connectors were subjected to a low-cycle high-amplitude loading regime. The performance of the mechanical anchorages in steel-concrete composite connections was evaluated in terms of ductility, strength degradation, and absorbed energy under cyclic loading circumstances. Nine steel-concrete composite connection specimens, shown in Figure 1.19, were tested. Three monotonic tests on a steel-concrete composite connection were performed to assess yield slip, yield load, ultimate slip, and ultimate shear strength capability. The size and strength of the anchorages were the parameters investigated.

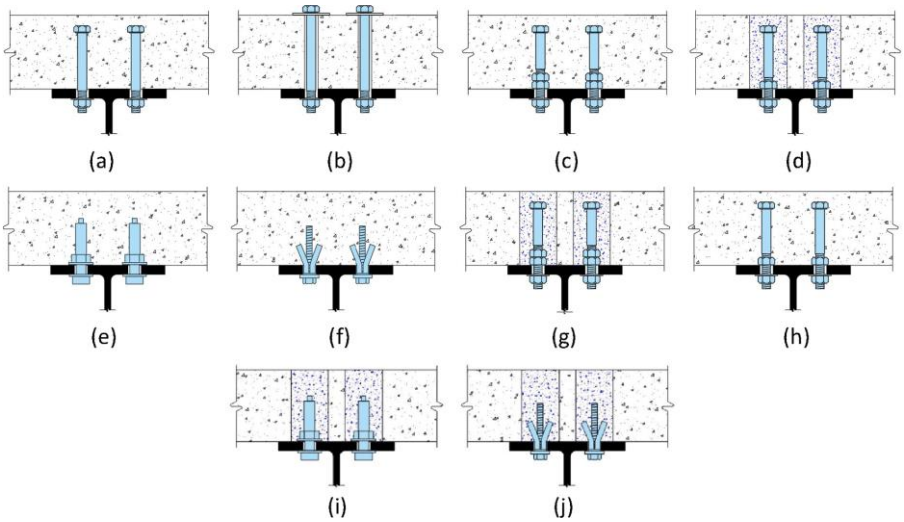

Figure 1.19: Investigated bolted shear connectors (Ataei et al., 2019)

The main failure modes observed during the experiments are fracture of the anchorage, concrete crushing, and deformation of the beam flange. Under monotonic loading, the anchorage size massively affects the behavior and capacity of the connection. With the increase of the diameter and the strength of the anchorage, the hysteric loop area may be increased. The connections with the anchorage grade higher than 8.8 have a behavior of decreasing strength degradation with the increase of the slip. Connectors with larger sizes provide higher ductility and energy dissipation. Additionally, increasing the connector size and strength enhances the initial stiffness.

Static and fatigue performances of through-bolt shear connectors were investigated by Balkos et al. (2019) with three beam bending experiments. Two beam specimens were tested under fatigue; however, beams did not fail under fatigue which shows that the fatigue resistance of through-bolt connectors is higher than the conventional welded studs. The effect of the fatigue test was a reduction of the pretension of the connections. The behavior of the beam specimens with through bolts is similar to the push-out specimens; on the other hand, beam specimens feature a higher initial slip load and a higher slip displacement value at bolt fracture.

A new innovative type of a demountable shear connector was suggested by Feidaki et al. (2019). The suggested connector, shown in Figure 1.20, is made up of a steel square hollow tube that is welded to a steel plate and fastened to the top flange of the steel section with four high-strength bolts. Precast hollow-core unit (HCU) slabs are used to construct the composite section with suggested shear connectors, which uses a yielding device called the yielding pocket (YP). The suggested design offers high initial stiffness, eliminates the need for hole tolerance, and provides a significant amount of ductility that is higher than the code requirements. The structural performance of the connector was investigated with push-out tests, and an FE model was constructed to simulate the behavior. The constructed model was used to conduct a parametric study.

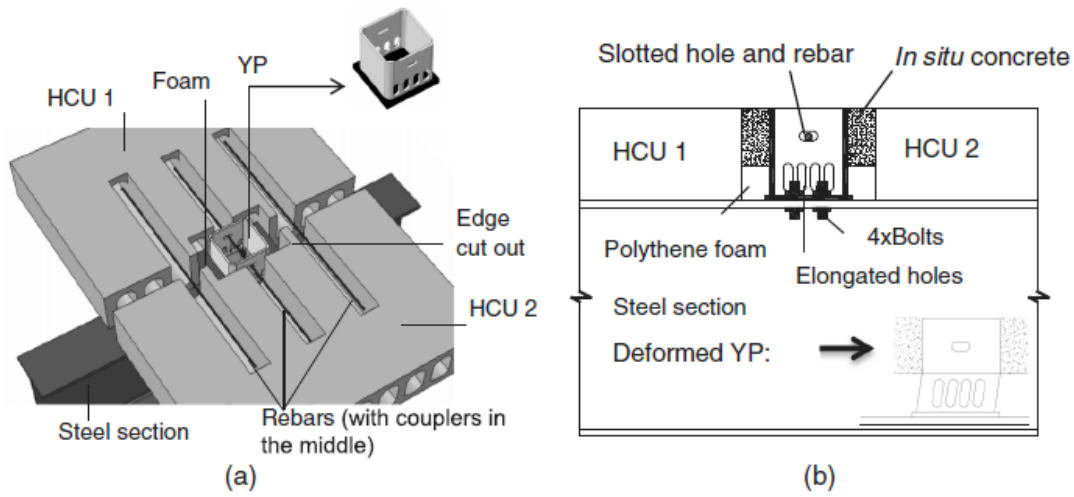

Figure 1.20: Suggested connector: (a) 3D view, (b) longitudinal view, and deformed shape (Feidaki et al., 2019)

According to experiments and numerical study results, the specimens designed for ductility can undergo slipping of 30 mm; meanwhile, the specimens of failure mode of concrete shear cracking can achieve a slip level of 6 mm, which is the ductile slip limitation stated by Eurocode 4 (2011). The main failure modes of the connection proposed are yielding of YP and vertical strips and the shear cracking of concrete HCU. The cast-in-place concrete required to fill the voids shown in Figure 1.20a

does not affect the stiffness of the connection, but it is required to provide the shear flow, and it has a significant effect on the ductility.

A numerical study related to optimizations that may be done aiming at the composite structures while providing demountable construction was conducted by Girão Coelho et al. (2019) using the experimental data presented by Rehman et al. (2016). In this study, the idea of the optimal span-to-depth ratio for composite beams with demountable shear connectors was investigated to optimize the weight of the beams and shear connector distributions over the span. Three shear connections were studied in terms of their influence on total composite beam stiffness in the range of 9 to 15m spans using a basic pseudo-plastic model and finite element modules. The ideal span-to-depth ratio of symmetrical and asymmetrical beams was estimated and compared to similar beams with traditional headed studs. The findings of the study underline the need to avoid the plasticity in the steel beam to provide reusability. Since the shear connectors used in the experimental study have lower initial stiffness compared to traditional studs, the anchorage distribution should be closer to the shear force variation along the beam so that the design can be optimized and end slip can be minimized. The optimal span-to-depth ratio (L/h) for demountable composite beams may be taken as 24 for unpropped composite beams with traditional welded headed studs, 22 for unpropped demountable composite beams, 28 for propped demountable composite beams.

The elastic behavior of composite beams with tapered steel sections and demountable shear connectors suggested by Kozma et al. (2018), shown in Figure 1.17, was investigated experimentally and numerically by Nijgh et al. (2019). The performance of different configurations of resin-injected bolt-coupler shear connections was investigated in this study to maximize the favorable effects of composite action while reducing the number of shear connectors. The study results successfully proved the demountability and reusability of a composite flooring system made up of tapered steel beams and prefabricated concrete decks joined by resin-injected bolt-coupler shear connections. The number of anchorages required to achieve the deflection or elastic-slip requirement in the applicable limit stated by

codes for a simply supported tapered composite beam can be reduced by relocating those anchorages closer to the supports.

The performance and behavior of the demountable shear connectors suggested previously, shown in Figure 1.7, at ambient and high temperatures were investigated by Sencu et al. (2019). A total of 21 push-out experiments, using the test setup shown in Figure 1.21, were conducted to understand the effects of varying nominal temperature levels of 20, 100, 300, 450, and 600 °C, perpendicular and parallel orientations of the steel decking with respect to the steel beam section, two different embedded shear connector lengths and two different compressive strengths of concrete. The testing of the specimens was conducted mainly under the steady-state condition where the environmental temperature is changed before the loading of the specimens until failure. Additionally, a few specimens were tested under the transient state condition where the environmental temperature was changed after the application of the loads equal to obtained capacities of steady-state tests.

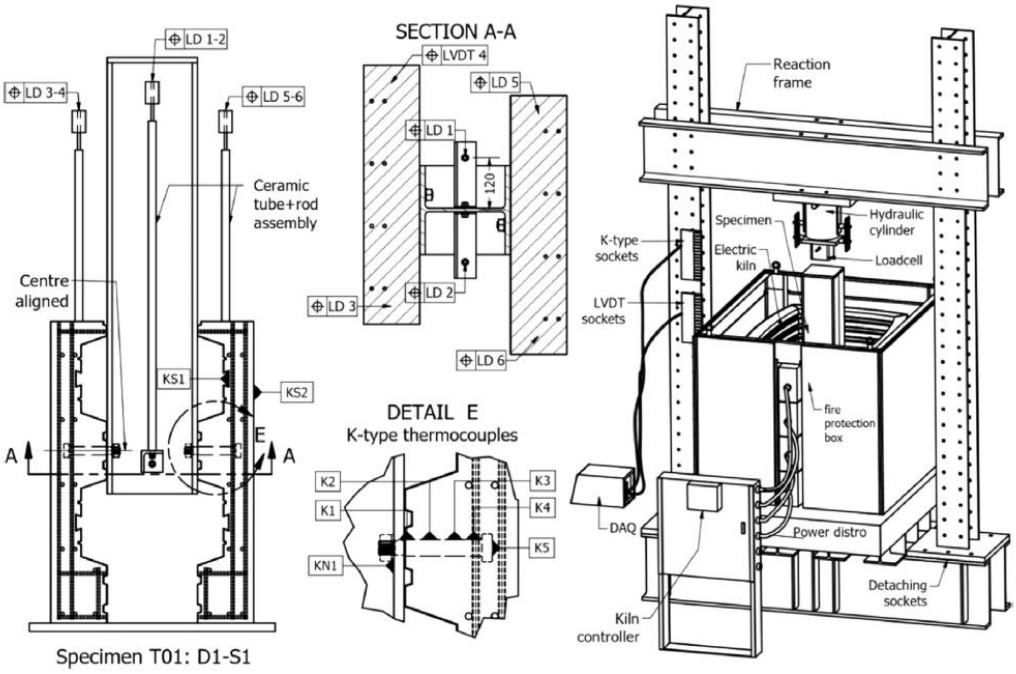

Figure 1.21: Test setup and instrumentation (Sencu et al., 2019)

According to the results of the experiments, at ambient, low elevated, and high temperatures, the connectors passed the slip ductility limit of 6 mm. In most cases with elevated temperatures, connectors showed very ductile behavior with a slip capacity higher than 20 mm. The failure modes changed according to the temperature, i.e., with a temperature level less than 400 °C, concrete crushing together with shear stud fracture was observed, while, at temperatures higher than 400 °C, the failure mode was stud fracture. Changing the connector embedded length did not provide any capacity improvement for specimens with the same concrete strength. Transient state tests showed that increasing the temperature of the environment after loading results in failure at a temperature less than the equivalent steady-state tests. In contrast, the equations given in the Eurocode 4 (2012) (Part 1.2) for estimation of the load-carrying capacity considering the temperature effects overestimated the capacity obtained from transient state tests. The capacity obtained in the case of perpendicular deck sheeting was too low.

An experimental study on demountable shear connectors subjected to combined shear and tension was conducted by Tan et al. (2019). Experiments were conducted on three types of connectors, shown in Figure 1.22, that were exposed to combined shear and tensile loads. Pull-out tests were performed to assess the tensile strength of each type of steel-concrete connection. The relationship between shear and tension loading was then determined using a series of modified push tests.

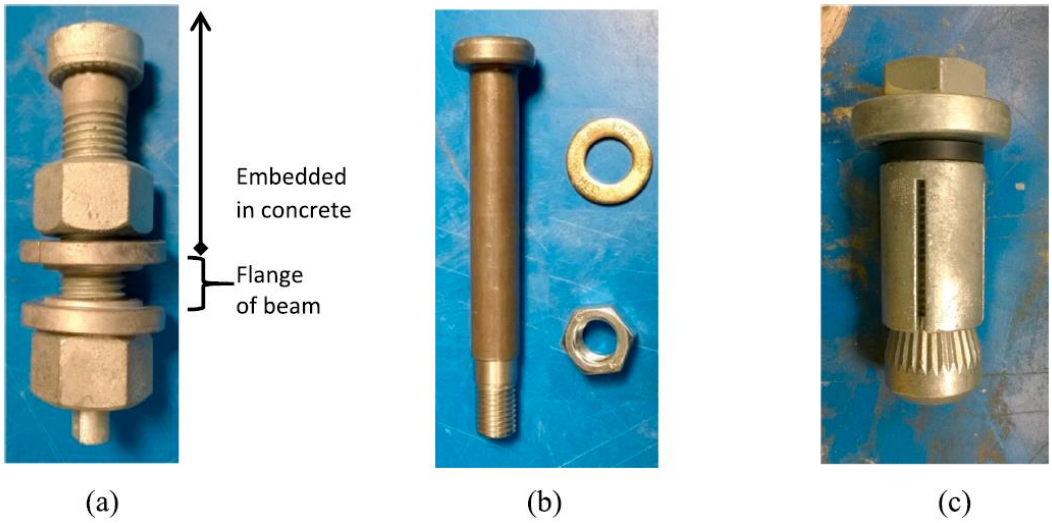

Figure 1.22: Connector types: (a) AJAX ONESIDE, (b) Machined demountable headed stud, (c) Lindapter hollo-bolt (Tan et al., 2019)

According to the results, demountable headed studs have higher ductility under pure shear than AJAX and Hollo-bolts. The shear capacity of the connectors is reduced significantly when it is combined with the tension where demountable headed studs show the lowest and Hollo-bolts show the highest reduction. The failure mode of connectors is dependent on material strength which results in connectors with higher strength, AJAX and Hollo-bolt, to show the concrete breakout type of failure and the connector with lower strength, stud, to show the fracture of the connector type of failure. AJAX connector has the highest shear resistance, whereas headed stud has the highest tensile resistance. Since the tensile resistance of AJAX and Hollo-bolt connectors is low, they are not suitable for composite walls.

A demountable clamping connector was suggested by L. Wang et al. (2019) and L. Wang et al. (2020), as shown in Figure 1.23. The pretension in the bolts was provided with a specified turn-of-the-nut system. To investigate the strength and ductility of the anchorages, nine push-out tests were conducted. The main parameters considered were bolt diameter, reinforcement layout, loading protocol, use of shims, and number of cast-in channels.

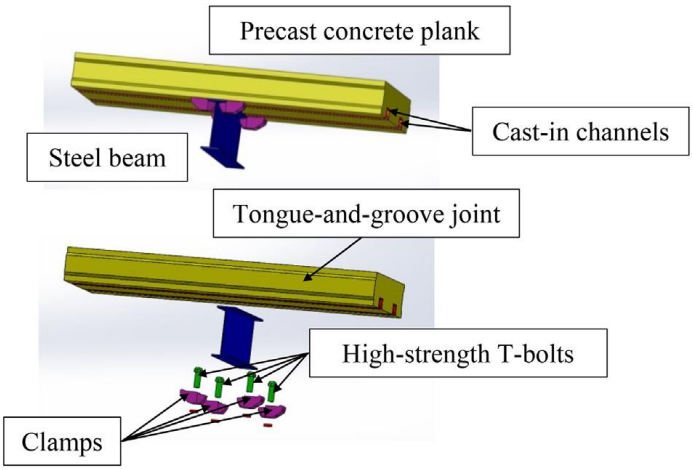

Figure 1.23: Beam with demountable connectors suggested (L. Wang et al., 2019)

The amount of the pretension provided to T-bolts was determined by pretension tests, and 1.5 turns of nut rotation were suggested for M24 and M20 bolts. The connection system with both M24 and M20 bolts showed no strength degradation and allowed large rotations at typical slip demand, e.g., an ultimate slip of 8.9 mm. However, at larger slips, e.g., 127 mm, the strength of M20 clamps declined gradually; meanwhile, M24 clamps preserved approximately 80% of their strength. Under cyclic loading, the clamps showed high energy-dissipating capacity, although strength reduction was observed. The load-carrying capacity was not affected by the shims. The initial stiffness and the ultimate slip capacity of the clamps are higher than the traditional headed studs with similar sizes. The local cracks occurred on the surface of the concrete caused by friction, and the change in reinforcement layout did not affect the formation of the cracks. The increase of the channels cast into the planks hastened the crack formation slip but did not affect the capacity of M24 clamps. The cyclic shear strength of the clamps is estimated to be 80% of the monotonical shear strength.

A numerical study was performed by Langarudi & Ebrahimnejad (2020) to simulate the behavior of a demountable shear connection system, shown in Figure 1.11. The effects of factors such as concrete strength, different positions, heights, and diameters of the shear connectors, the kind and thickness of the steel deck, and the influence of the reinforcing arrangement on the behavior of these connectors were

investigated. According to the results, the shear capacity and the ductility of demountable connectors are higher than the welded connectors, while initial stiffness is lower; but, the capacity and the stiffness of the connectors may be increased with the increase of the concrete strength. An increase in both the diameter and the amount of the connectors provides higher capacity and stiffness. The capacity and the stiffness of the slabs are also dependent on the type of the profiled deck used. The placement of connecters in a staggered position slightly affects the behavior; however, the position of the studs, whether strong or weak, affects the behavior since the capacity reduction of weak positioned connectors is sharp. The main failure modes are the tear out of the connector and the concrete fracture.

A novel welded demountable shear connector (WDSC) was proposed by Suwaed et al. (2022). In the design of the connector, a steel tube was bolted to a compatible machined traditional headed stud and filled with grout, while the headed stud was welded on the steel section, as shown in Figure 1.24. The main parameters considered in this experimental study were the thickness of the tube, the inclusion of the grout fill, and the strength of the concrete. Additionally, a numerical study was conducted for further parametric studies.

According to the results, the WDSC showed higher shear strength and similar initial stiffness compared with the headed stud. The failure mode of all specimens exhibited ductile shear failure at the root of the stud shank and crushing of the concrete gradually, but the failures occurred after a slip level of 6 mm.

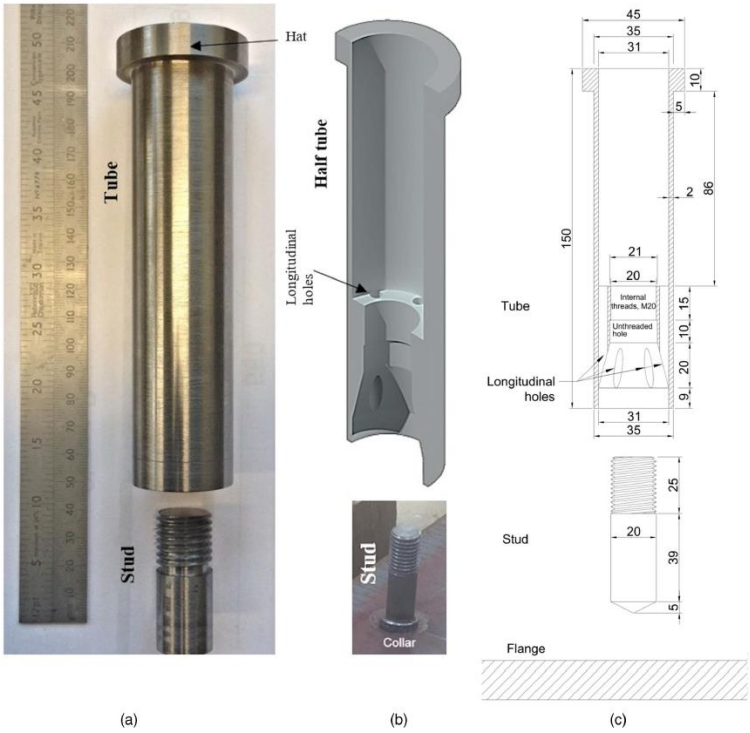

Figure 1.24: WDSC: (a) Tube and stud, (b) Tube 3D cute, (c) cross-sectional view (Suwaed et al., 2022)

According to the parametric study, the shear strength of the connection system was affected primarily by the strength of the concrete and the yield strength of the tube, while the yield strength and the thickness of the tube had less effect. Additionally, the existence of the grout fill affected the initial stiffness and the shear strength; however, the shear strength of the grout did not affect the behavior and capacities.

1.5 Objectives and Scope

As indicated in Chapter 1.4, providing a demountable shear connection between the steel and concrete members in the design of composite structures is essential to reduce the direct and indirect costs that may arise because of the need for a replacement of the concrete deck and ensure a sustainable design to reduce constructional carbon footprint and prevent climate change caused by material waste. To overcome the problems stated, a novel demountable shear connector is proposed.

The proposed bolted angle shear connector is shown in Figure 1.25. The connector is composed of two angle sections and a high-strength bolt, all of which are conventional elements used in steel construction. The lower angle section is larger in size when compared with the upper angle section. This is the main element that resists the shear forces developed at the steel-concrete interface. A bolt hole is introduced into the horizontal leg of the lower angle section. A high-strength bolt is used to fasten the angle section to the flange of a steel beam, as shown in Figure 1.25. The sizes of the bolt holes introduced into the angle section and the flange of the beam depend on the bolt size. While standard hole sizes recommended in AISC (2016) can be adopted, the bolt holes can be of the same size as the diameter of the bolt. A smaller angle section is welded to the upper part of the vertical leg of the larger angle section. The upper angle provides tension resistance to the connector. The two connectors can be welded together using fillet welds. The same geometry obtained by welding two angle sections can be produced by bending a steel plate as well. However, this requires an automated production line to produce these connectors in mass quantities. The welding process can be avoided by making use of the cold bending operation. In this study, the investigation of the proposed connection has been conducted in three phases in which the first phase focuses on push-out tests to determine the shear load-carrying capacity, the second phase focuses on pull-out tests to determine the tensile load-carrying capacity, and the third phase focuses on full-scale composite beam tests to determine the feasibility and applicability.

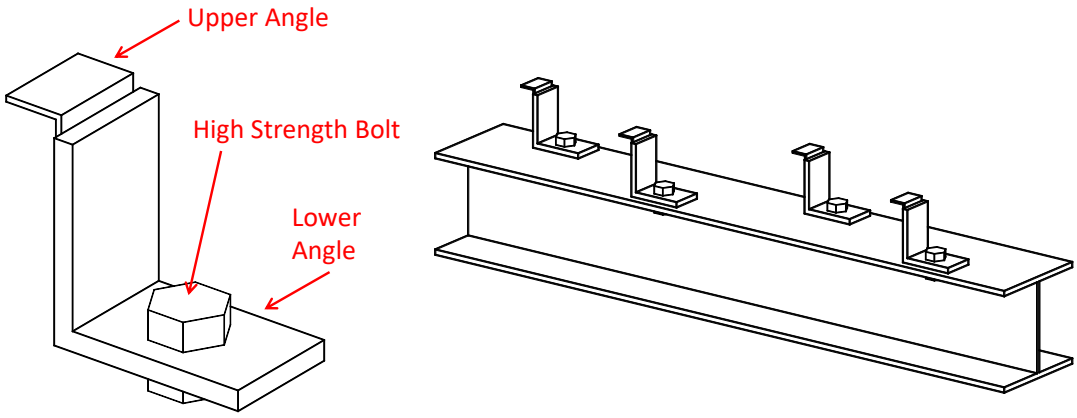

Figure 1.25: The proposed demountable shear connector

1.6 Organization of the Thesis

This thesis covers five chapters. The first chapter is the Introduction, and the remaining four chapters pursue the first chapter. An explanation of the remaining four chapters is given below:

In Chapter 2, the push-out experiments conducted on the connection are explained in detail. The experiment matrix, parameters considered, test setup, and results of the experiments are given. The results are used in the design of beam specimens which are explained in Chapter 4.

In Chapter 3, the pull-out experiments conducted on the connection are explained in detail. The experiment matrix, parameters considered, test setup, and results of the experiments are given. According to the data obtained from these experiments, the possibility of splitting between concrete slab and steel beam is determined.

In Chapter 4, the full-scale beam bending experiments that are conducted on beams designed with the proposed connector are explained in detail. The experiment matrix, degrees of composite action considered, test setup, and results of the experiments are given. These experiments demonstrate the feasibility and the applicability of the

proposed connectors and prove that the proposed demountable shear connector is a strong alternative for the traditional headed studs.

Lastly, Chapter 5 summarizes the experimental study conducted, discusses the results, and includes guidance for the future work that may be conducted on this subject.

CHAPTER 2

PUSH-OUT TESTS

In this chapter, an experimental investigation of the proposed shear connectors is made via push-out tests conducted at the Structural Mechanics Laboratory of the Department of Civil Engineering at Middle East Technical University. These tests are the first phase of the experimental study and aim to understand the behavior and the load-slip response of the connectors.

2.1 Test Setup

The test setup developed by Arıkoğlu et al. (2020) was used in the testing program with some modifications. The technical drawings of the test setup are given in Figure 2.1, and the photos are indicated in Figure 2.2. The test setup was designed to conduct a push-out test on a typical connector, which is embedded into a concrete block. The setup was configured as a self-contained system that does not require any reaction wall or a vertical support system. A HEA360 I-section main beam was supported at its ends by HEB200 sections. A reaction block was attached to the HEA360 section. The loading was applied by making use of a 600 kN capacity hydraulic jack. The stationary end of the hydraulic jack was attached to the reaction block. The applied load was measured by making use of a 1000 kN capacity load cell which is mounted on the non-stationary end of the hydraulic jack. The load was transferred from the load cell to a 40 mm diameter ball bearing, which was used to reduce the bending effects on the hydraulic jack. The ball bearing was in contact with a 40 mm thick and 160 mm wide steel plate which was used to uniformly distribute the loading to the surface of the concrete block.

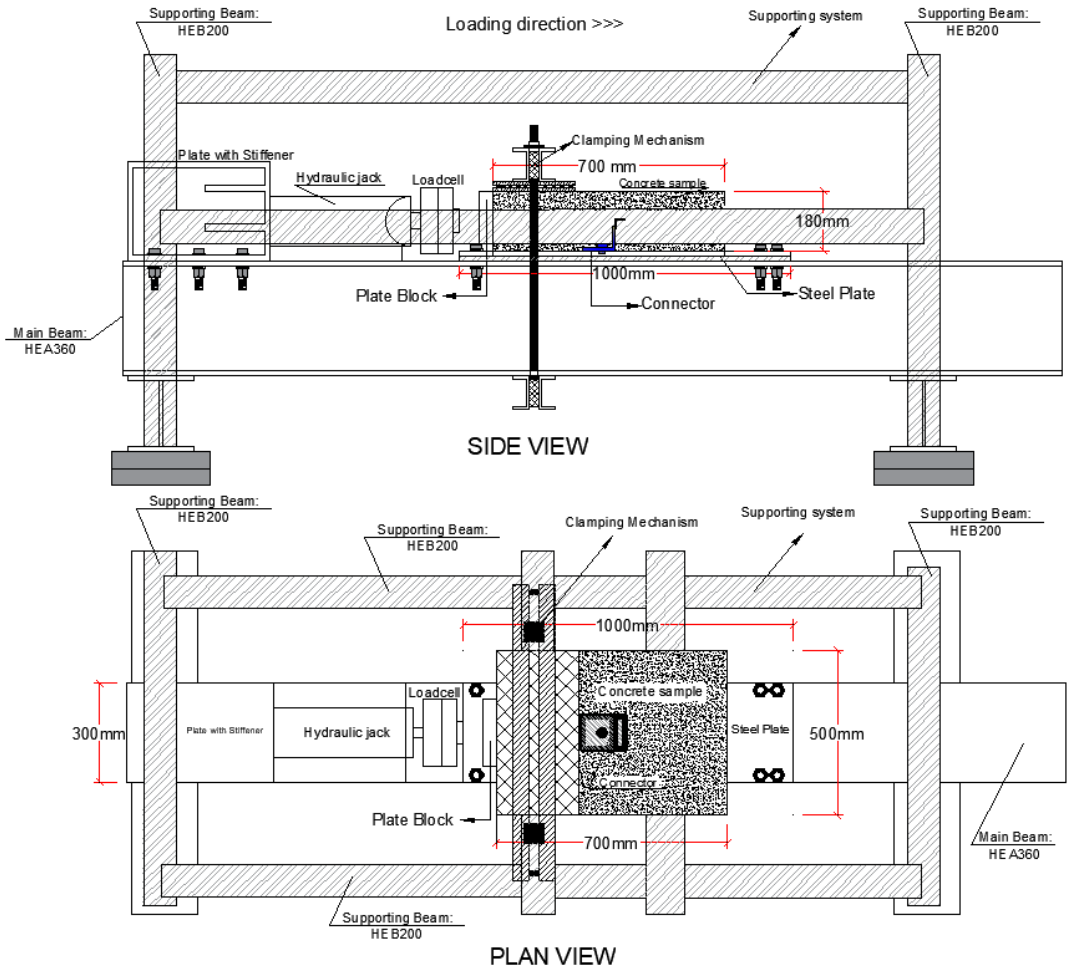

Figure 2.1: Test setup

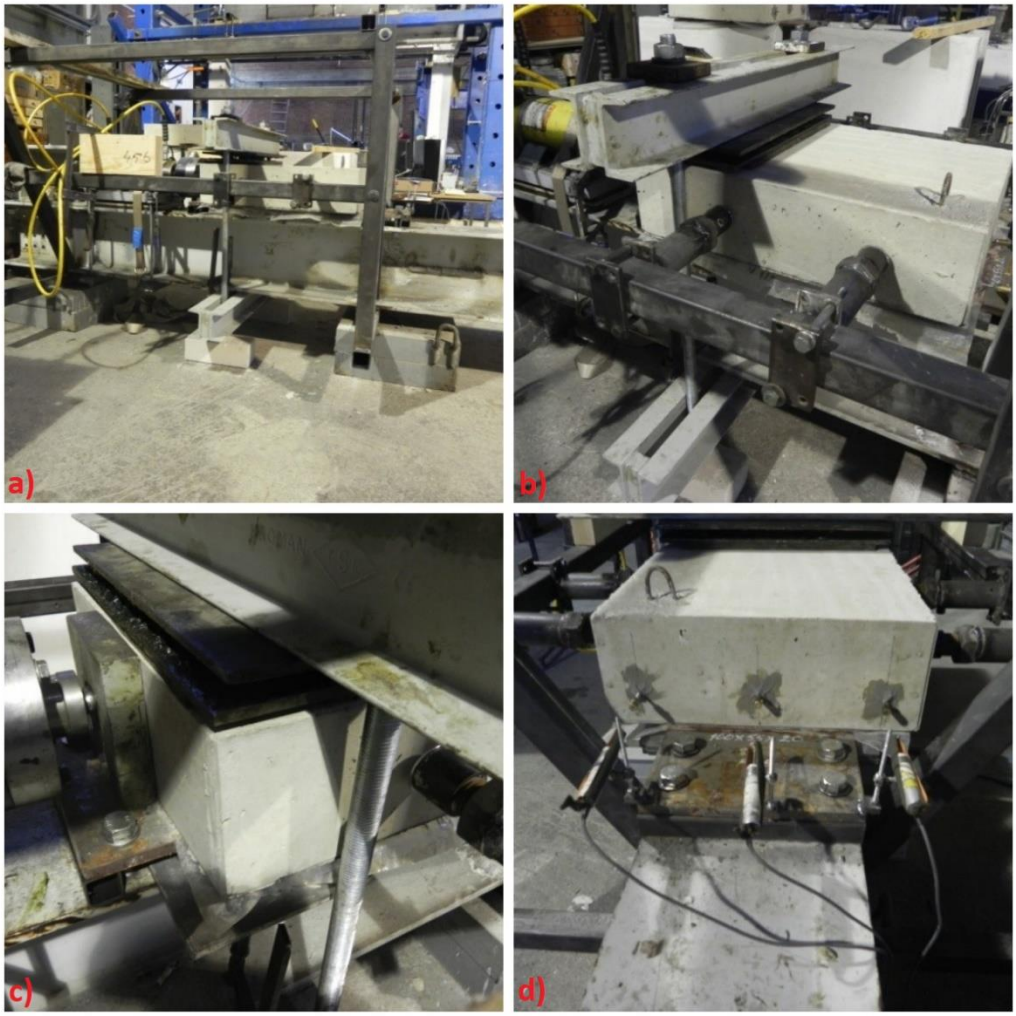

Figure 2.2: Photos of the test setup: a) General view, b) Lateral support system, c) Clamping mechanism and loading plate, d) LVDTs

A typical test specimen consists of a steel base plate, a connector attached to the base plate, and a concrete block. The high-strength bolt used in the proposed connector extends below the bottom of the base plate. In other words, there needs to be a clearance between the top flange of the HEA360 I-section and the base plate. Two hollow structural sections of size 50x2 mm were placed in between the base plate and the flange of the HEA360 section to provide this clearance. Six M22 bolts were used to fasten the base plate to the flange of the HEA360 main beam.

Separation of the concrete block from the steel surface is common in most push-out tests due to the eccentricity between the loading axis and the reaction axis of the

connectors (steel-concrete interface). Restraint systems can be provided to reduce the amount of separation. A clamping mechanism, shown in Figure 2.1 and Figure 2.2, was used to prevent the uplifting of the concrete block. The clamping mechanism was self-contained and consisted of two built-up sections and two 36 mm steel rods. The built-up sections were fabricated by back-to-back channel sections with a spacing of 50 mm in between. One of the built-up sections was placed above the concrete block, and the other one was in contact with the bottom flange of the HEA360 section. Two steel rods were placed in between the channel sections and slightly tightened. Any uplift demand of the concrete block results in axial forces to be developed in the rods which are transmitted to the built-up sections. The use of a clamping mechanism can lead to frictional resistance being developed at the surface of contact between the built-up section and the concrete block. A roller mechanism was employed to lower the amount of frictional resistance. As shown in Figure 2.2, the roller mechanism consists of two steel plates and ball bearing that were placed in between these plates. The surfaces of the steel plates were greased to allow for the free movement of the concrete block.

There can be an eccentricity between the axis of the hydraulic jack and the axis of the bolt used in the proposed connector. This eccentricity can produce a torsional loading on the connector. Welded connectors such as channels have resistance against the accidental torsional loads. On the other hand, the bolted angle shear connector cannot provide any torsional resistance. This, in turn, can result in the rotation of the concrete block in the horizontal plane. An external self-contained restraining frame system was attached to the HEA360 section to prevent the rotation of the concrete block. Hollow structural sections were used for this framing. Two roller bearings were employed on each side of the concrete block, as shown in Figure 2.2. These bearings prevented any out-of-plane movement of the concrete block.

2.1.1 Details of Data Recording Instruments

The applied load and the slip at the interface of the steel base plate and concrete block were monitored during a typical test. Three LVDTs were placed at the back end of the specimen, as shown in Figure 2.2. Two of the LVDTs were used to measure the slip at the edges of the concrete block, while the other LVDT was used to measure the slip at the center; the locations of the LVDTs are given in Figure 2.3. The amount of concrete block rotation can be directly calculated by making of these three independent readings.

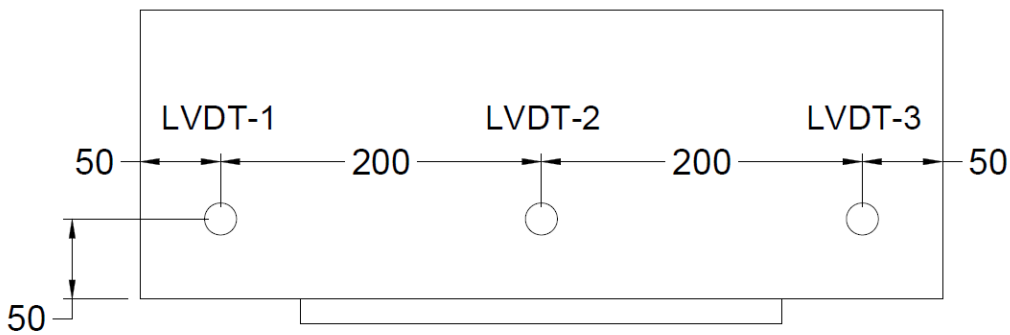

Figure 2.3: Orientation of LVDTs

2.2 Test Specimens

The push-out experiments conducted in the literature, e.g., in Figure 1.21, were constructed with two concrete blocks on both sides of the steel I-section connected with mechanical anchorages. However, in this study, a different test setup with a similar working mechanism was used. Thus, the design of the test specimens was different when compared with the ones in the literature.

The concrete blocks used in test specimens had 500 mm width, 700 mm length, and 180 mm thickness. Six 8 mm diameter bars in the long direction and four 8 mm diameter bars in the short direction were used as steel reinforcement. These were

placed symmetrically at the top and bottom surfaces, as shown in Figure 2.4. Bolted angle shear connectors were fastened to 15 mm thick base plates, all of which were ordered from the same batch. A total of 33 specimens were designed and the parameters considered are given in Section 2.2.1. A plastic sheet was placed above the base plate to prevent the bonding of concrete to the base plate and to eliminate friction at the interface.

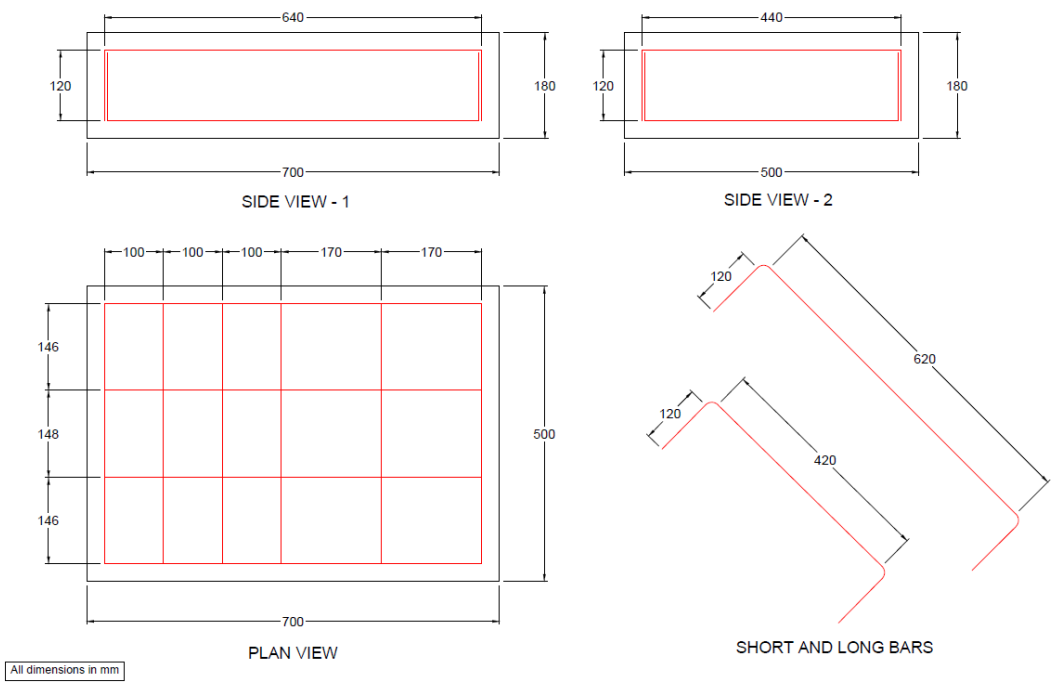

Figure 2.4: Reinforcement layout

2.2.1 Design Parameters

The size of the angle section, bolt diameter, bolt grade, concrete strength, loading direction, and bolt thread conditions were considered the prime variables. Detailed tabulated information about the specimens is given in Table 3.1. European angle sections L100×10, L75×8, L70×7, and L60×6 with 50 mm width were used in the testing program. The leg size of the channel section was selected considering typical concrete deck thicknesses used in composite construction. M20 and M24 high-strength bolts with 8.8 and 10.9 grades were considered. The bolts conformed to

EN14399 (2009) specification. The length of the bolts was 55 mm, and according to EN14399 (2009), the entire bolt length should be threaded for such short bolts. The bolts, shown in Figure 2.5, were specially produced to have a 15 mm unthreaded portion and a 40 mm threaded portion. This enabled to have two different thread conditions for the critical shear plane.

Figure 2.5: Bolts used (left – M20, right – M24)

Two different concrete compressive strengths were considered. The first 24 specimens employed relatively higher strength concrete when compared with the rest of the specimens. The nomenclature used for identifying the specimens is as follows: the first entry is used for the size of the angle section where L100 is for L100×10, L75 is for L75×8, L70 is for L70×7, and L60 is for L60×6, the second entry is used for the bolt diameter where M20 and M24 stand for 20 mm and 24 mm bolt diameters, respectively, the third entry is for the bolt strength where 8 and 10 stand for 8.8 and 10.9 grade bolts, respectively, the fourth entry is used for the loading direction, as shown in Figure 2.6, and thread condition where F, B, E, I stand for “front,” “back,” “excluded” and “included,” respectively, and the fifth entry stands for concrete compressive strength where C1 and C2 stand for batch 1 and batch 2, respectively.

For example, specimen 12 L70-M20-8-FE-C1 is a specimen with an L70×7 angle section, M20 8.8 grade bolt, loaded in the front direction, threads are excluded from

the shear plane, and the concrete compressive strength is equal to the strength of batch 1. The list of all nomenclatures is given in Table 3.2.

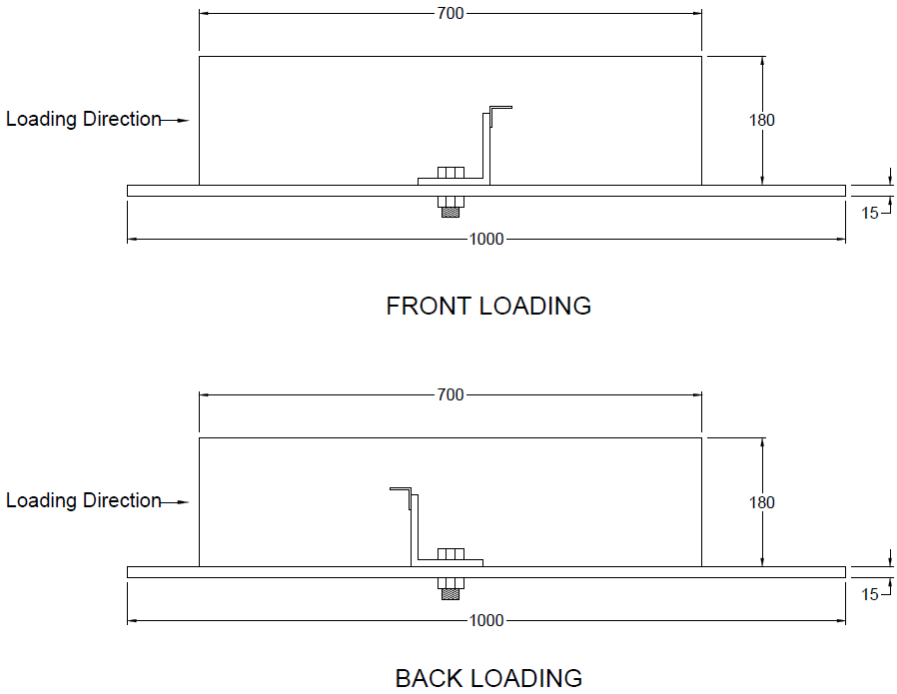

Figure 2.6: Loading directions

Table 2.1: Experiment matrix for push-out specimens

Specimen #	Serie #	L Shape Size (mm)	Bolt Grade	Bolt diameter (mm)	Loading Direction	Threads in Shear Plane
1	1	100	10.9	24	Front	Excluded
2	1	100	8.8	24	Front	Excluded
3	1	100	10.9	20	Front	Excluded
4	1	100	8.8	20	Front	Excluded
5	1	75	10.9	24	Front	Excluded
6	1	75	8.8	24	Front	Excluded
7	1	75	10.9	20	Front	Excluded
8	1	75	8.8	20	Front	Excluded
9	1	70	10.9	24	Front	Excluded
10	1	70	8.8	24	Front	Excluded
11	1	70	10.9	20	Front	Excluded
12	1	70	8.8	20	Front	Excluded
13	1	60	10.9	24	Front	Excluded
14	1	60	8.8	24	Front	Excluded
15	1	60	10.9	20	Front	Excluded
16	1	60	8.8	20	Front	Excluded
17	1	100	10.9	24	Back	Excluded
18	1	75	10.9	24	Back	Excluded
19	1	70	10.9	24	Back	Excluded
20	1	100	10.9	24	Back	Excluded
21	1	60	10.9	24	Front	Included
22	1	100	8.8	24	Front	Included
23	1	100	10.9	20	Front	Included
24	1	100	8.8	20	Front	Included
25	2	100	10.9	20	Front	Excluded
26	2	75	10.9	20	Front	Excluded
27	2	60	10.9	20	Front	Excluded
28	2	100	8.8	24	Front	Excluded
29	2	75	8.8	24	Front	Excluded
30	2	60	8.8	24	Front	Excluded
31	2	100	8.8	20	Front	Excluded
32	2	75	8.8	20	Front	Excluded
33	2	60	8.8	20	Front	Excluded

Table 2.2: Specimen nomenclatures

Specimen #	Nomenclature	Specimen #	Nomenclature	Specimen #	Nomenclature
1	L100-M24-10-FE-C1	2	L100-M24-8-FE-C1	3	L100-M20-10-FE-C1
4	L100-M20-8-FE-C1	5	L75-M24-10-FE-C1	6	L75-M24-8-FE-C1
7	L75-M20-10-FE-C1	8	L75-M20-8-FE-C1	9	L70-M24-10-FE-C1
10	L70-M24-8-FE-C1	11	L70-M20-10-FE-C1	12	L70-M20-8-FE-C1
13	L60-M24-10-FE-C1	14	L60-M24-8-FE-C1	15	L60-M20-10-FE-C1
16	L60-M20-8-FE-C1	17	L100-M24-10-BE-C1	18	L75-M24-10-BE-C1
19	L70-M24-10-BE-C1	20	L100-M24-10-BE-C1	21	L60-M24-10-FI-C1
22	L100-M24-8-FI-C1	23	L100-M20-10-FI-C1	24	L100-M20-8-FI-C1
25	L100-M20-10-FE-C2	26	L75-M20-10-FE-C2	27	L60-M20-10-FE-C2
28	L100-M24-8-FE-C2	29	L75-M24-8-FE-C2	30	L60-M24-8-FE-C2
31	L100-M20-8-FE-C2	32	L75-M20-8-FE-C2	33	L60-M20-8-FE-C2

In all specimens, L30×3 angle sections were welded to the lower angle section, as shown in Figure 1.25. Bolt holes were introduced into the base plate and the angle sections by making use of a drill bit. The size of the holes was equal to the bolt diameter. In other words, there was no tolerance between the bolt hole and the bolt.

The first 16 specimens were designed to examine the effect of angle size, bolt size, and bolt strength on the behavior of connectors loaded in the front direction. The proposed connectors are expected to be used in conditions where the threads are excluded from the shear plane to maximize the ultimate strength of the connector. Therefore, the threads were excluded from the shear plane in all of the specimens except four. Specimens 17 through 20 were designed to examine the effect of loading direction where these specimens were loaded in the opposite direction (back) when compared with the other specimens. It should be noted that specimens 17 and 20 were identical and were used to investigate the repeatability of results. Specimens 21 through 24 were used to investigate the thread condition where the threads were included from the shear plane. This was accomplished by inserting the bolts upside down. In other words, the nut was in contact with the angle section, and the bolt head was in contact with the base plate. Specimens 25 through 33 were similar to specimens 1 through 16. The angle sizes of L100×10, L75×8, and L60×6 were considered without L70×7 to reduce the number of specimens. The concrete compressive strength employed in specimens 25 through 33 was lower than its counterpart.

2.2.2 Geometric and Material Properties

The geometric properties of the angle sections were measured with a caliper and reported in Table 2.3. The dimension conformed to the EN10056-2 (1993) standard. Tensile tests were conducted on the coupons extracted from the L-shapes and the base plate according to EN10002 (2001). The measured material properties, i.e., yield strength, ultimate strength, and percent elongation, are indicated in Table 2.4.

Table 2.3: Angle section dimensions

L100x10				
L_{upper}	t_{upper}	L_{lower}	t_{lower}	
100.70	10.14	100.11	10.22	
101.06	10.08	100.41	10.24	
100.64	10.12	100.77	10.28	
100.80	10.11	100.43	10.25	Average
L75x8				
L_{upper}	t_{upper}	L_{lower}	t_{lower}	
76.64	7.51	76.18	8.11	
76.73	7.49	76.22	8.02	
76.12	7.50	76.63	7.81	
76.50	7.50	76.34	7.98	Average
L70x7				
L_{upper}	t_{upper}	L_{lower}	t_{lower}	
70.79	6.93	70.22	7.26	
70.62	6.87	70.30	7.26	
70.32	6.90	70.05	7.26	
70.58	6.90	70.19	7.26	Average
L60x6				
L_{upper}	t_{upper}	L_{lower}	t_{lower}	
59.77	5.98	60.33	6.08	
59.60	5.97	60.46	6.09	
59.92	5.95	60.27	6.09	
59.76	5.97	60.35	6.09	Average

Table 2.4: Material properties of angle sections and base plate

Specimen Name	$F_{y,0.2}$	F_u	%E
	MPa	MPa	-
$L100x10_{N1}$	348.59	492.53	-
$L100x10_{N2}$	350.83	496.33	33.42
L100x10 - Average	349.71	494.43	33.42
$L75x8_{N1}$	355.91	516.38	28.30
$L75x8_{N2}$	354.81	524.12	28.73
L75 - Average	355.36	520.25	28.52
$L70x7_{N1}$	332.37	434.82	30.75
$L70x7_{N2}$	332.43	432.85	34.37
L70x7 - Average	332.40	433.83	32.56
$L60x6_{N1}$	348.34	485.58	30.61
$L60x6_{N2}$	347.50	485.15	29.07
L60x6 - Average	347.92	485.36	29.84
Base Plate	338.37	431.22	27.18

The stress-strain responses obtained from the coupon tests are given in Figure 2.7.

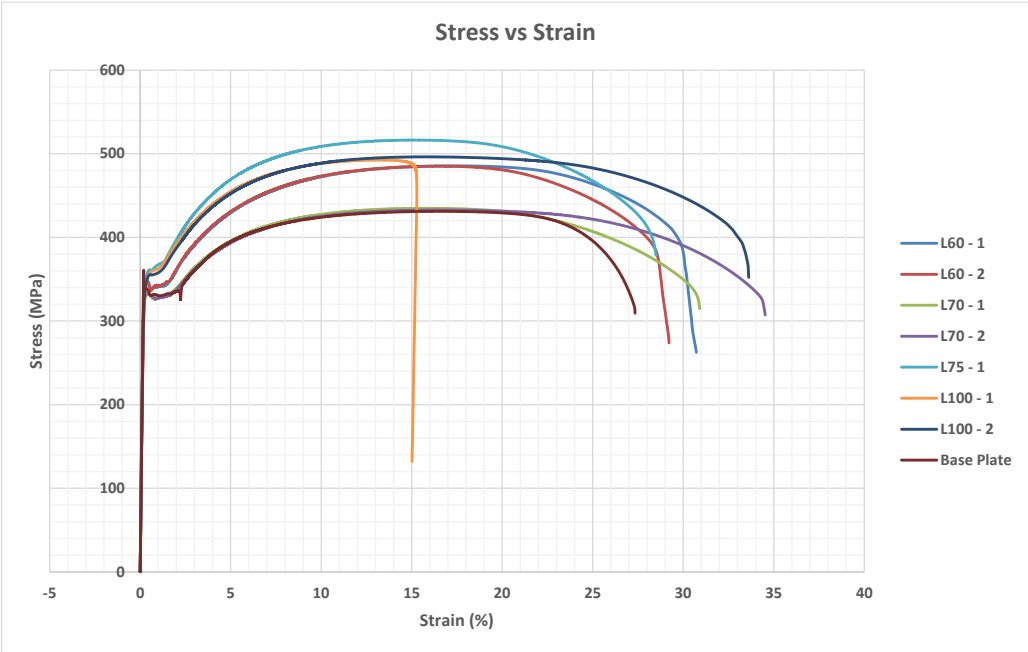

Figure 2.7: Stress versus strain diagram for angles

The bolts were subjected to tensile testing at the manufacturer's testing facility. Two specimens were tested for each bolt grade and diameter. The average ultimate tensile strengths of the bolts are reported in Table 2.5.

Table 2.5: Material properties of bolts

Specimen Name	$F_{y,0.2}$	F_u
	Mpa	Mpa
M20x55 - 8.8 -Test 1	794.2	885.7
M20x55 - 8.8 -Test 2	801.9	885.4
M20x55 - 8.8 -Average	798.0	885.6
M20x55 - 10.9 -Test 1	1010.3	1097.1
M20x55 - 10.9 -Test 2	1005.6	1114.2
M20x55 - 10.9 - Average	1008.0	1105.7
M24x55 - 8.8 -Test 1	894.3	963.1
M24x55 - 8.8 -Test 2	867.0	953.9
M24x55 - 8.8 - Average	880.7	958.5
M24x55 - 10.9 -Test 1	1033.7	1136.1
M24x55 - 10.9 -Test 2	915.8	1108.0
M24x55 - 10.9 - Average	974.8	1122.1

Cylinder samples were taken during concrete placement and kept at the same laboratory conditions as push-out specimens. The 28th compressive strengths were 39.1 MPa and 28.7 MPa for batch 1 and batch 2, respectively.

2.3 Test Results

A total of 33 specimens, explained in Table 4.1, were tested. The conducted experiments had a single phase, and specimens were loaded to failure.

While conducting the experiments of specimen 1, hydraulic jack shutdown itself. Therefore, the loading of specimen 1 was completed in more than one stage, similar to cyclic loading.

2.3.1 Observed Failure Modes

Observed failure modes of the specimens are given in Table 2.6. The main failure modes considered were bolt shear-off, cracking of concrete block, crushing of concrete, tilting of connector, and connector shear-off. The explanation of the failure modes is given below:

- Bolt shear-off: Rupture of the bolt due to shear forces
- Cracking of concrete block: Observation of cracks with lengths greater than 5 cm
- Crushing of concrete: Total loss of the load-carrying capacity of the concrete block supporting the connector
- Tilting of connector: Bending of the connector edge
- Connector shear-off: Rupture of the connector due to shear forces

The failure modes are illustrated as given in Figure 2.8, Figure 2.9, and Figure 2.10.

Figure 2.8: Failure mode of specimen 2 (Bolt shear-off & cracking of concrete)

Figure 2.9: Failure mode of specimen 5 (Tilting of connector)

Figure 2.10: Failure mode of specimen 9 (connector shear-off & crushing of concrete)

Table 2.6: Failure mode of each specimen

Specimen #	Nomenclature	Observed Failure Mode
1	L100-M24-10-FE-C1	Bolt shear-off - Cracking of concrete block
2	L100-M24-8-FE-C1	Bolt shear-off - Cracking of concrete block
3	L100-M20-10-FE-C1	Bolt shear-off
4	L100-M20-8-FE-C1	Bolt shear-off
5	L75-M24-10-FE-C1	Tilting of connector - Crushing of concrete
6	L75-M24-8-FE-C1	Tilting of connector - Cracking of concrete block
7	L75-M20-10-FE-C1	Tilting of connector - Cracking of concrete block - Bolt shear-off
8	L75-M20-8-FE-C1	Bolt shear-off
9	L70-M24-10-FE-C1	Crushing of concrete - Connector shear-off
10	L70-M24-8-FE-C1	Crushing of concrete - Connector shear-off
11	L70-M20-10-FE-C1	Crushing of concrete - Connector shear-off
12	L70-M20-8-FE-C1	Bolt shear-off - Tilting of connector
13	L60-M24-10-FE-C1	Crushing of concrete - Connector shear-off
14	L60-M24-8-FE-C1	Crushing of concrete - Tilting of connector
15	L60-M20-10-FE-C1	Crushing of concrete - Connector shear-off
16	L60-M20-8-FE-C1	Bolt shear-off - Tilting of connector
17	L100-M24-10-BE-C1	Crushing of concrete
18	L75-M24-10-BE-C1	Crushing of concrete - Connector shear-off
19	L70-M24-10-BE-C1	Crushing of concrete - Connector shear-off
20	L100-M24-10-BE-C1	Crushing of concrete
21	L60-M24-10-FI-C1	Tilting of connector - Crushing of concrete
22	L100-M24-8-FI-C1	Bolt shear-off
23	L100-M20-10-FI-C1	Bolt shear-off
24	L100-M20-8-FI-C1	Bolt shear-off
25	L100-M20-10-FE-C2	Crushing of concrete - Connector shear-off
26	L75-M20-10-FE-C2	Crushing of concrete - Tilting of connector
27	L60-M20-10-FE-C2	Crushing of concrete - Connector shear-off
28	L100-M24-8-FE-C2	Crushing of concrete - Tilting of connector
29	L75-M24-8-FE-C2	Crushing of concrete - Tilting of connector
30	L60-M24-8-FE-C2	Crushing of concrete - Tilting of connector
31	L100-M20-8-FE-C2	Bolt shear-off
32	L75-M20-8-FE-C2	Crushing of concrete - Bolt shear-off
33	L60-M20-8-FE-C2	Crushing of concrete - Tilting of connector

In general, as a result of decreasing the angle size from L100x10 to L60x6, the failure evolved from bolt shear-off to a situation where the concrete block was crushed and the connector edge was bent. However, observed failure modes and the reported ultimate load-carrying capacities might not represent the real behavior or the practical usable strength of the specimens since specimens underwent very high deformations during experiments. As mentioned before, the steel-concrete

composite beams encounter very low slip deformations. Thus, loads carried at slip displacements of 3, 6, 9, and 12 mm were reported to predict the connector capacity depending on the degree of composite action. Additionally, full-scale beam bending tests are required to determine the failure modes that might be expected in practice.

2.3.2 Load-Slip Response

In order to present the data in an effective manner, specimens were grouped according to the angle sizes, i.e., L100x10, L75x8, L70x7, and L60x6, and bolt properties, i.e., M24 grade 10.9, M24 grade 8.8, M20 grade 10.9, and M20 grade 8.8. Thus, the load-slip behavior of specimens is presented in groups.

As mentioned, specimen 1 experienced problems during loading. To show the whole behavior of specimen 1, load-slip values of both the first and the second loadings are considered in Figure 2.11. However, in grouped graphs, only the first loading was considered.

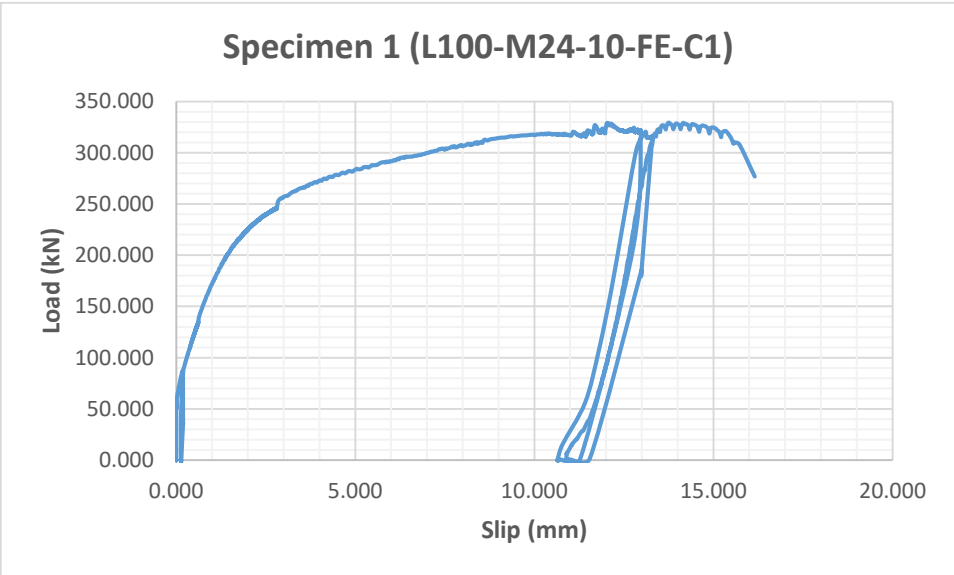

Figure 2.11: Load vs slip behavior of specimen 1

To understand the load-slip behavior of the specimens at the very start, i.e. around 1 mm slip, initial stiffness values were calculated and given in Table 2.7.

Table 2.7: Initial stiffness of each specimen

Specimen #	Nomenclature	Initial Stiffness (kN/mm)
1	L100-M24-10-FE-C1	171.7
2	L100-M24-8-FE-C1	137.5
3	L100-M20-10-FE-C1	63.0
4	L100-M20-8-FE-C1	72.1
5	L75-M24-10-FE-C1	131.5
6	L75-M24-8-FE-C1	117.3
7	L75-M20-10-FE-C1	91.0
8	L75-M20-8-FE-C1	127.5
9	L70-M24-10-FE-C1	141.5
10	L70-M24-8-FE-C1	115.0
11	L70-M20-10-FE-C1	103.8
12	L70-M20-8-FE-C1	89.1
13	L60-M24-10-FE-C1	122.3
14	L60-M24-8-FE-C1	143.9
15	L60-M20-10-FE-C1	80.2
16	L60-M20-8-FE-C1	114.2
17	L100-M24-10-BE-C1	112.1
18	L75-M24-10-BE-C1	115.8
19	L70-M24-10-BE-C1	122.6
20	L100-M24-10-BE-C1	100.5
21	L60-M24-10-FI-C1	72.7
22	L100-M24-8-FI-C1	127.5
23	L100-M20-10-FI-C1	40.3
24	L100-M20-8-FI-C1	83.2
25	L100-M20-10-FE-C2	84.4
26	L75-M20-10-FE-C2	91.7
27	L60-M20-10-FE-C2	97.8
28	L100-M24-8-FE-C2	126.6
29	L75-M24-8-FE-C2	122.6
30	L60-M24-8-FE-C2	114.6
31	L100-M20-8-FE-C2	60.1
32	L75-M20-8-FE-C2	88.5
33	L60-M20-8-FE-C2	96.6

According to the results, in general, the initial stiffness against slip decreased with the decrease of the angle size, bolt diameter, bolt grade, and concrete quality.

To examine the effects of the change of bolt properties, the slip displacement of the specimen groups, according to the angle sizes, under applied shear loads were considered. All of the considered groups had front loading direction, threads excluded from the shear plane, and the concrete quality of C1. The load-slip graph of each specimen is given in Figure 2.12, Figure 2.13, Figure 2.14, and Figure 2.15 for L100x10, L75x8, L70x7, and L60x6, respectively.

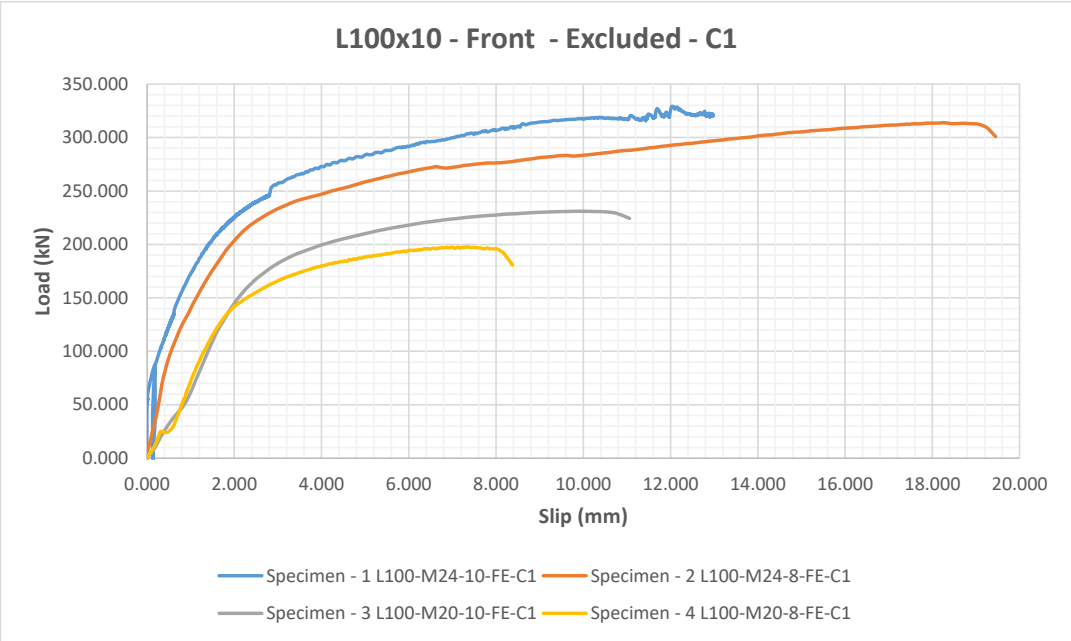

Figure 2.12: Effects of the bolt properties – L100x10

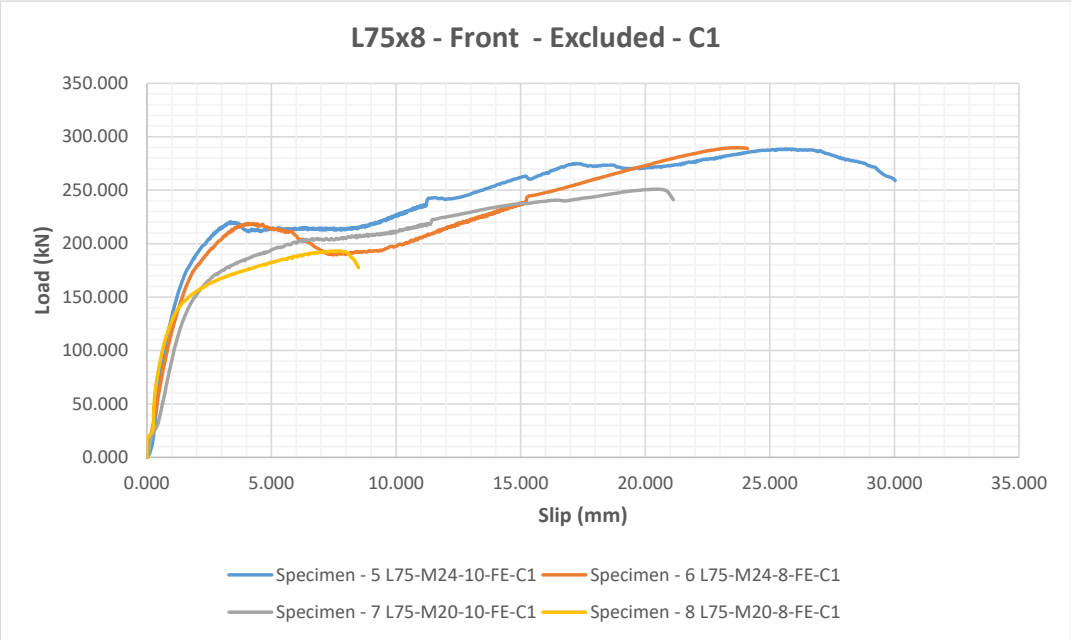

Figure 2.13: Effects of the bolt properties - L75x8

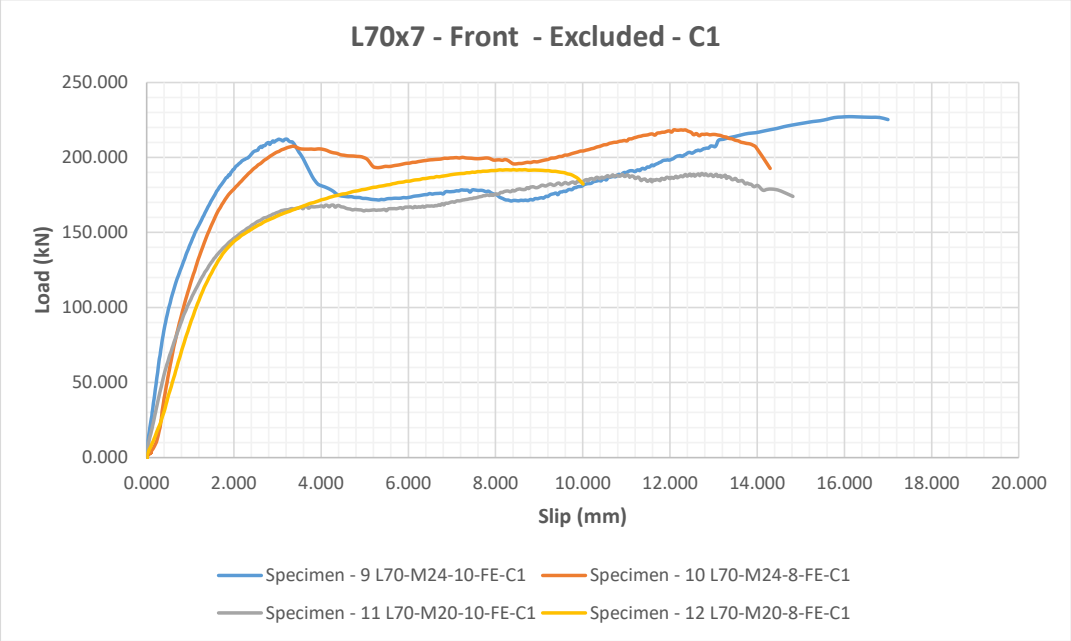

Figure 2.14: Effects of the bolt properties - L70x7

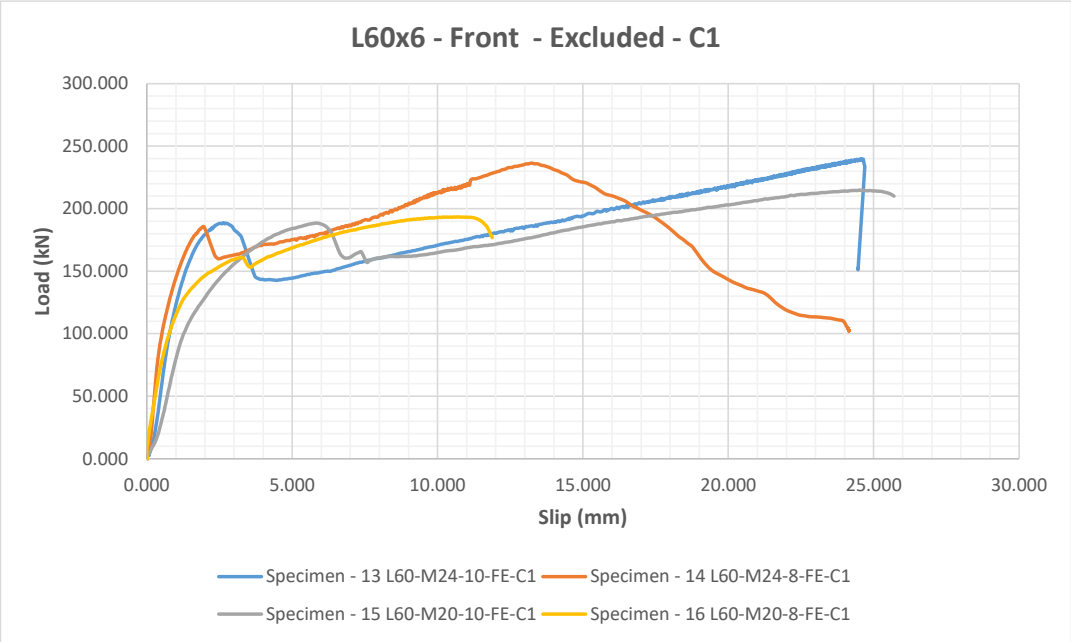

Figure 2.15: Effects of the bolt properties - L60x6

The load-slip graph of each specimen with C2 quality concrete is given in Figure 2.16, Figure 2.17, and Figure 2.18for L100x10, L75x8, and L60x6, respectively.

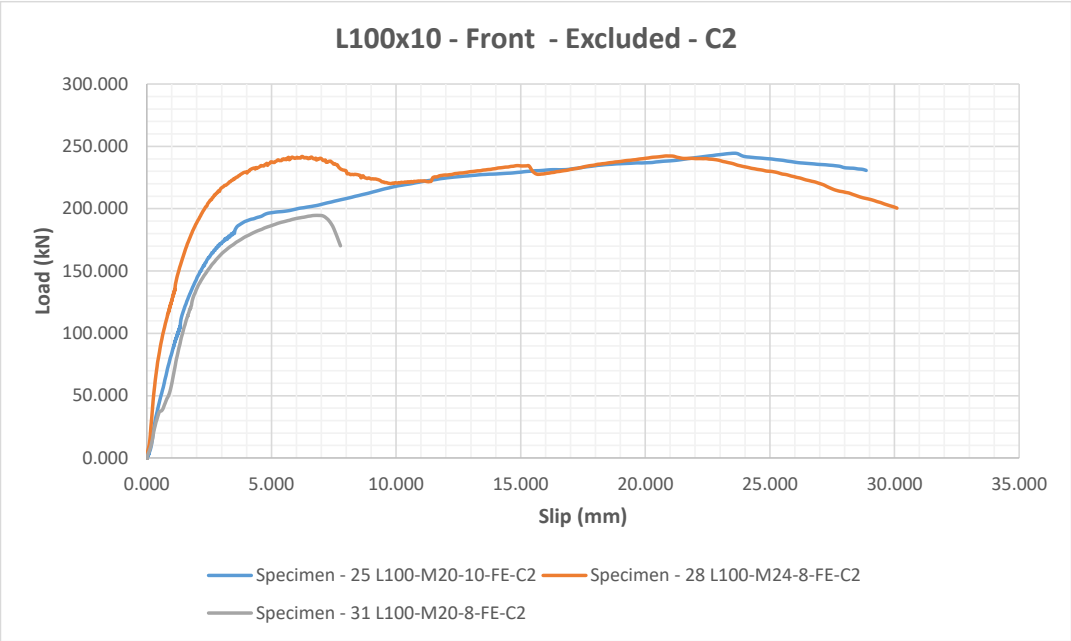

Figure 2.16: Effects of the bolt properties - L100x10

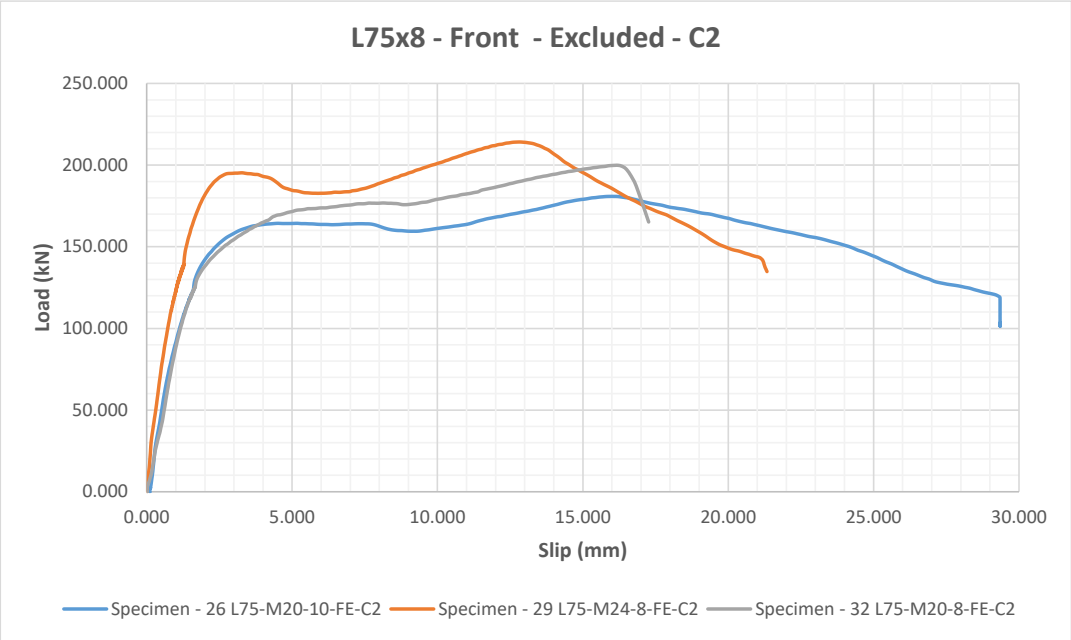

Figure 2.17: Effects of the bolt properties - L75x8

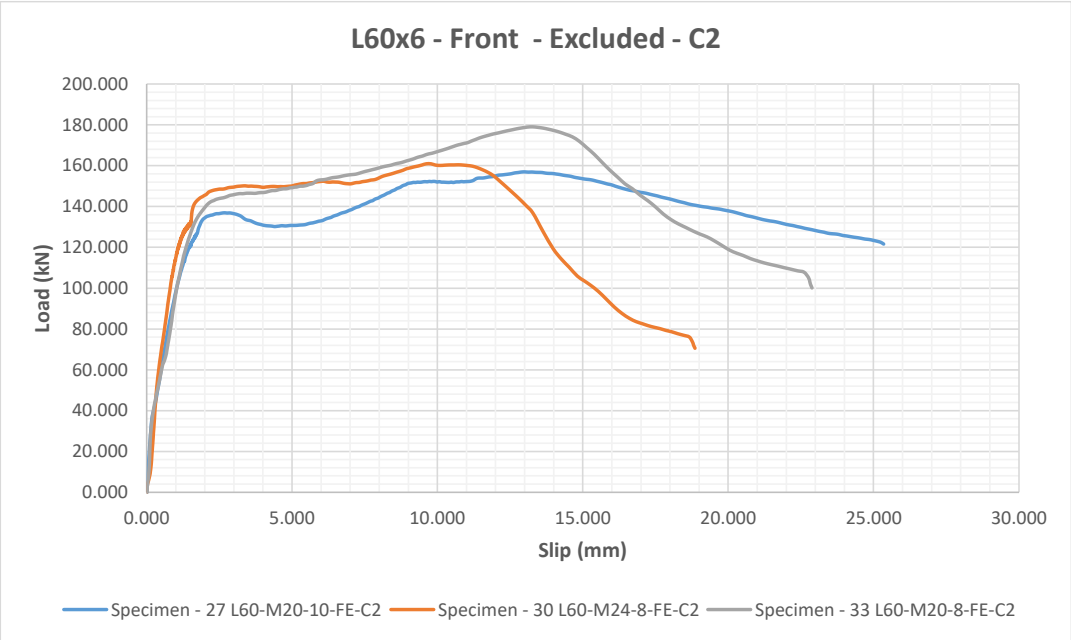

Figure 2.18: Effects of the bolt properties - L60x6

According to the results, providing bolts with higher diameter and grade increased the initial stiffness, load-carrying, and slip capacities. In other words, M24 bolts provided higher initial stiffness than the M20 bolts, and grade 10.9 bolts provided

higher initial stiffness than the grade 8.8 bolts in most of the cases, as shown in Table 2.7. Additionally, load-carrying and slip capacities increased with the increase of the bolt capacity, which is related to bolt grade and diameter.

To examine the effects of the change of angle size, the slip displacement of the specimen groups, according to the bolt sizes and grades, under applied shear loads were considered. All of the considered groups had front loading direction, excluded threads from the shear plane, and the concrete quality of C1. The load-slip graph of each specimen is given in Figure 2.19, Figure 2.20, Figure 2.21, and Figure 2.22 for M24 grade 10.9, M24 grade 8.8, M20 grade 10.9, and M20 grade 8.8 bolts, respectively.

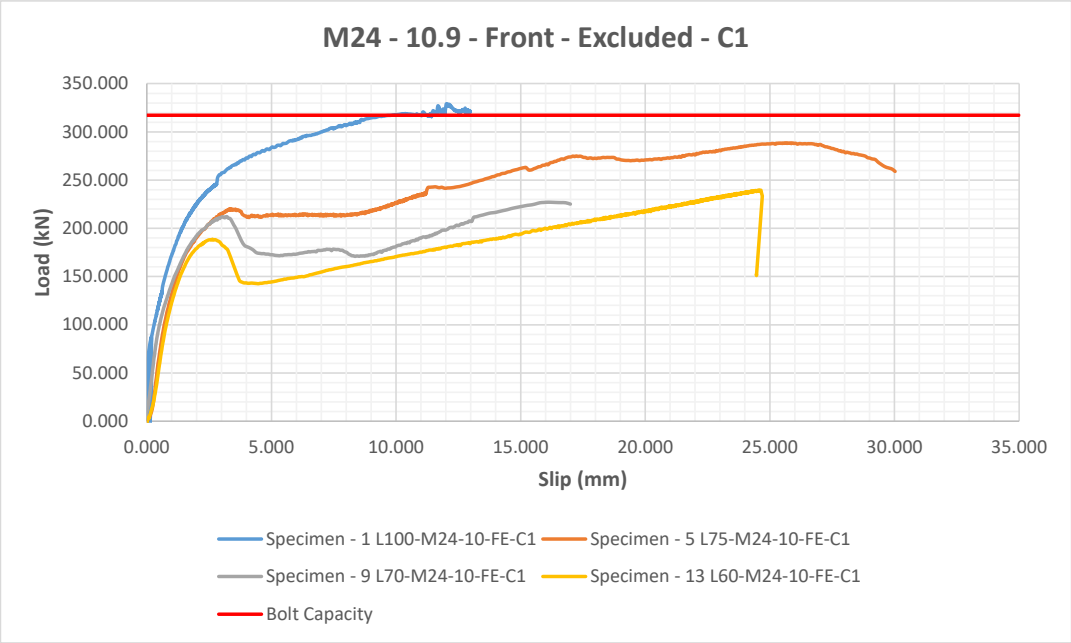

Figure 2.19: Effects of the angle size - M24 - 10.9 bolt

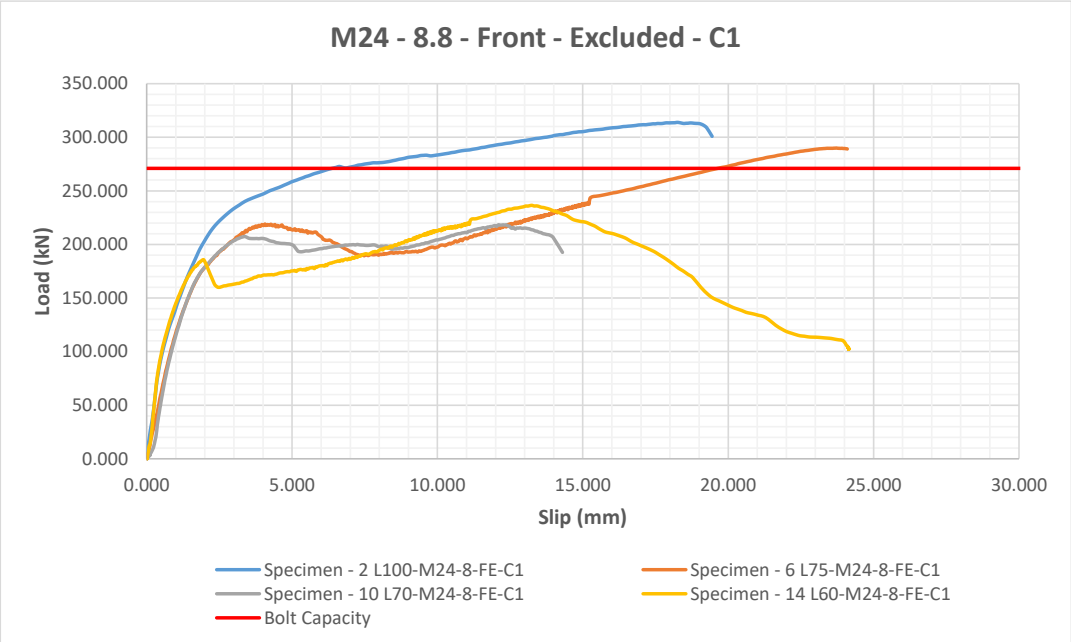

Figure 2.20: Effects of the angle size - M24 - 8.8 bolt

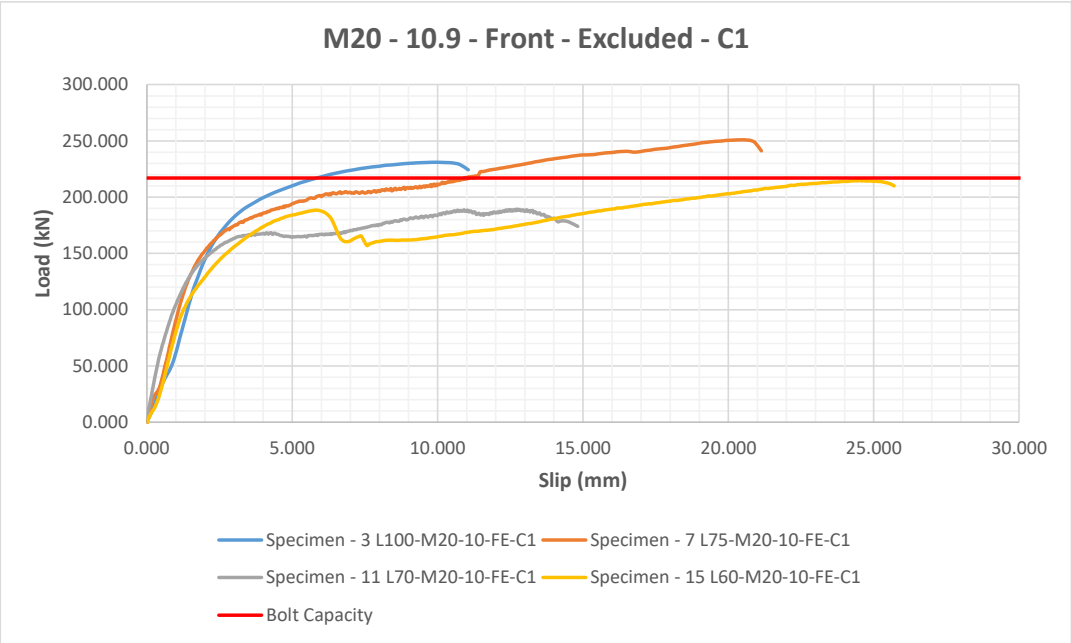

Figure 2.21: Effects of the angle size - M20 - 10.9 bolt

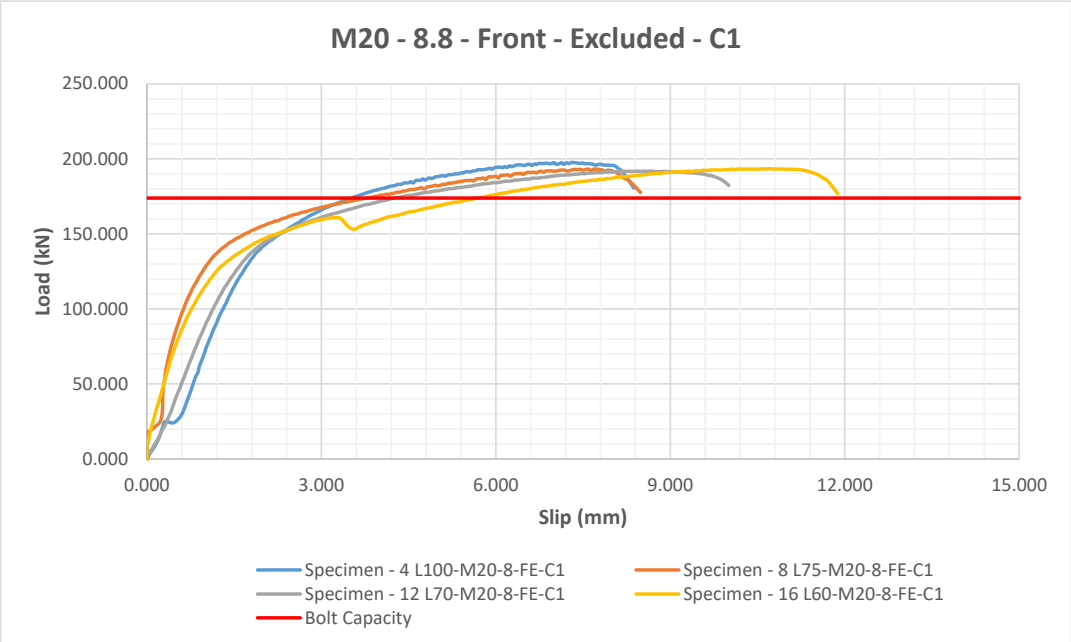

Figure 2.22: Effects of the angle size - M20 - 8.8 bolt

The load-slip graph of each specimen with C2 quality concrete is given in Figure 2.23, Figure 2.24, and Figure 2.25 for M24 grade 8.8, M20 grade 10.9, and M20 grade 8.8 bolts, respectively.

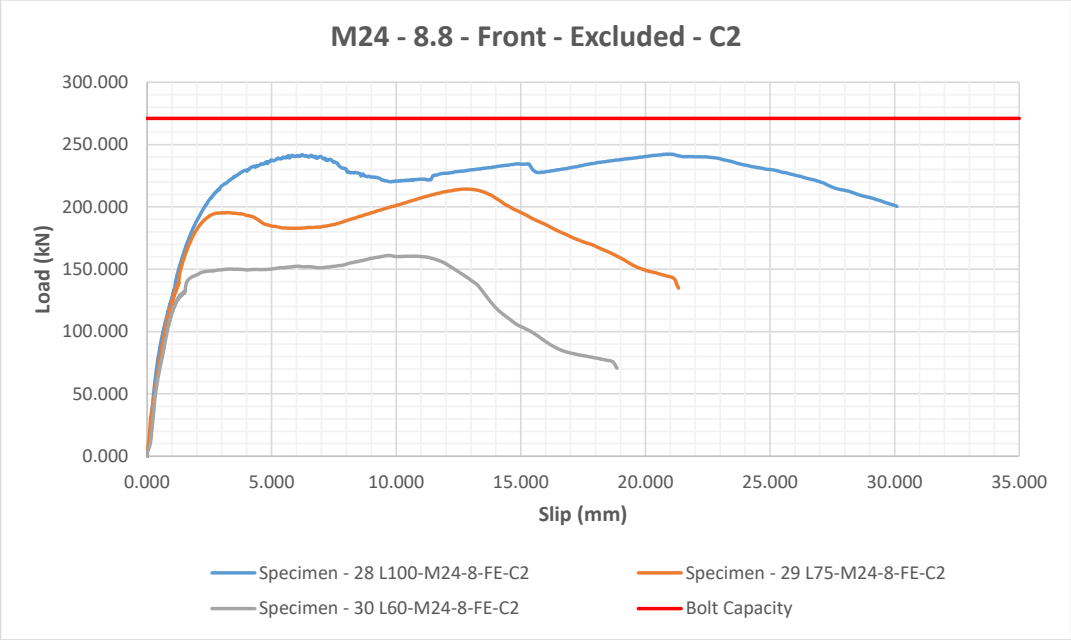

Figure 2.23: Effects of the angle size - M24 - 8.8 bolt

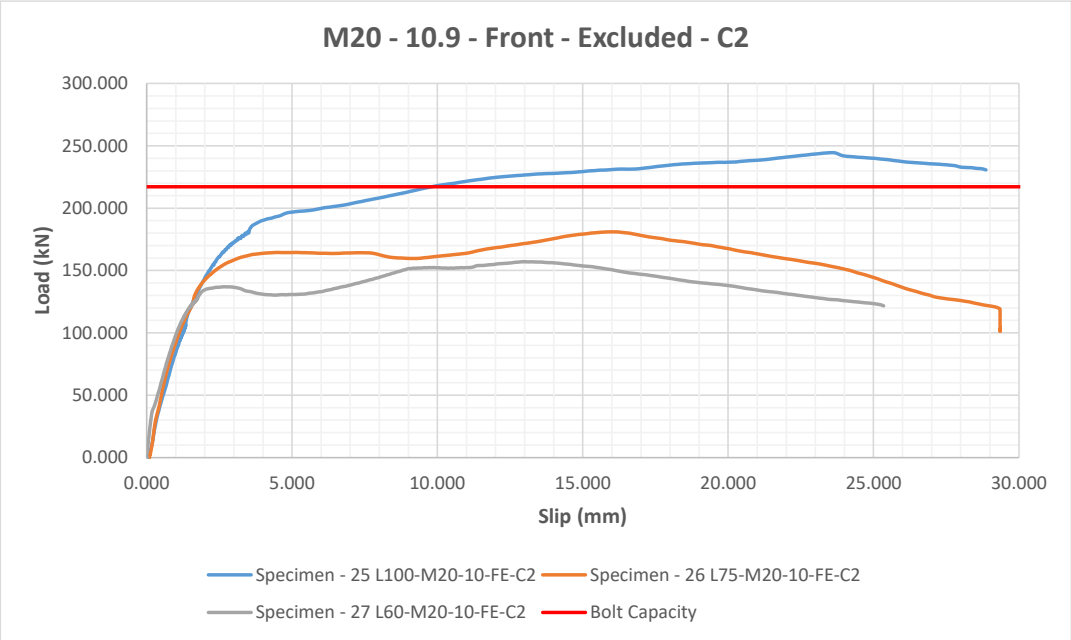

Figure 2.24: Effects of the angle size - M20 - 10.9 bolt

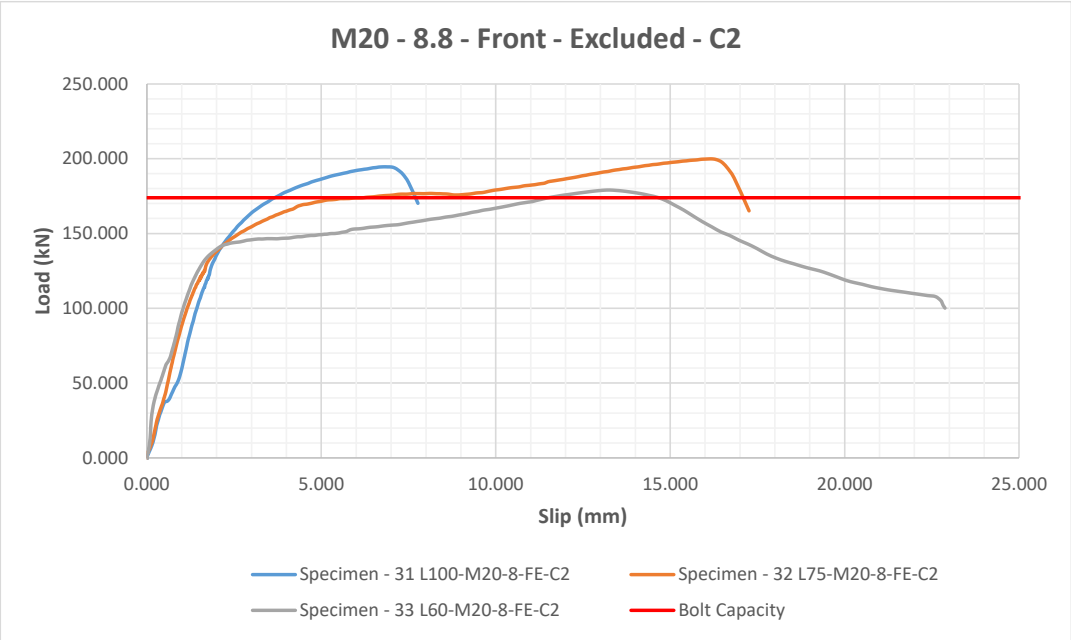

Figure 2.25: Effects of the angle size - M20 - 8.8 bolt

The bolt capacities given in the graphs were calculated using Equation 2.1, given in AISC (2016). The group effect capacity reducing factor of 0.9 was not considered since connectors contained single bolts.

$$R_{n-bolt} = 0.625 * F_{u-bolt} * A_b \tag{2.1}$$

Where R_n is the shear load-carrying capacity of the bolt, F_u is the ultimate tensile strength of the bolt, given in Table 2.5, and A_b is the area of the bolt.

Using Equation 2.1, the capacity of the bolts was calculated as given below.

$$R_{n-M24-10.9} = 0.625 * 1122.1 * \frac{24^2 * \pi}{4} = 317266.3\ N = 317.27\ kN$$

$$R_{n-M24-8.8} = 0.625 * 958.5 * \frac{24^2 * \pi}{4} = 271009.5\ N = 271.01\ kN$$

$$R_{n-M20-10.9} = 0.625 * 1105.7 * \frac{20^2 * \pi}{4} = 217103.7\ N = 217.10\ kN$$

$$R_{n-M20-8.8} = 0.625 * 885.6 * \frac{20^2 * \pi}{4} = 173878.2\ N = 173.88\ kN$$

According to the results, providing larger angle sizes increased the initial stiffness. The load-carrying capacity of the connectors was also increased since the area that transfers the applied load to the concrete block increased with the increase in the angle size; however, with the increase of the applied load, bolt capacities were exceeded, which resulted in bolt shear-off and caused slip capacity reduction. In other words, with larger angle sizes, the thickness of the connector and the concrete contact area increased. Hence, the initial stiffness against slip increased. A higher contact area between the connector and the concrete block retarded the crushing of the concrete block, which allowed higher loads. Nevertheless, retardation of the concrete crushing resulted in higher shear forces in the steel-concrete interface that caused bolt shear-off. The bolts with relatively lower capacity, i.e., M20 grade 8.8 bolts in this study, failed in small slip values since the stiffness against slip was high.

To strengthen the behavior explained above, the comparison graphs of the specimens with threads included in the shear plane and threads excluded from the shear plane are given in Figure 2.26, Figure 2.27, Figure 2.28, and Figure 2.29.

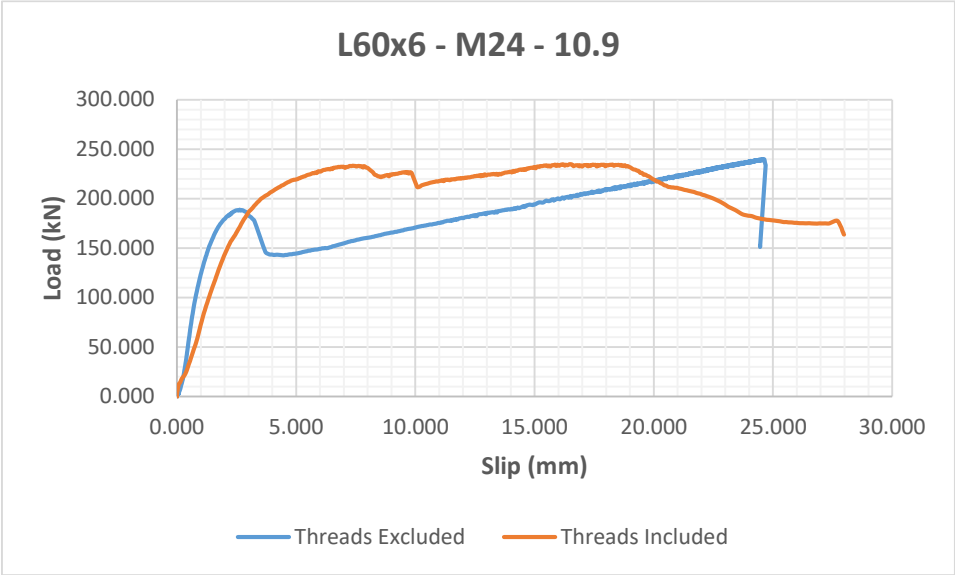

Figure 2.26: Specimen 13 (threads excluded) and specimen 21 (threads included) comparison

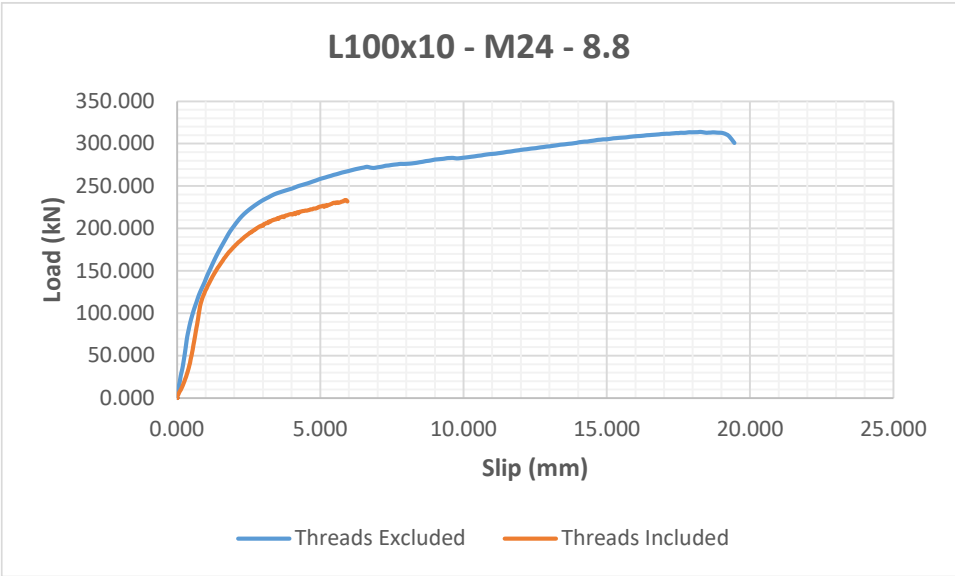

Figure 2.27: Specimen 2 (threads excluded) and specimen 22 (threads included) comparison

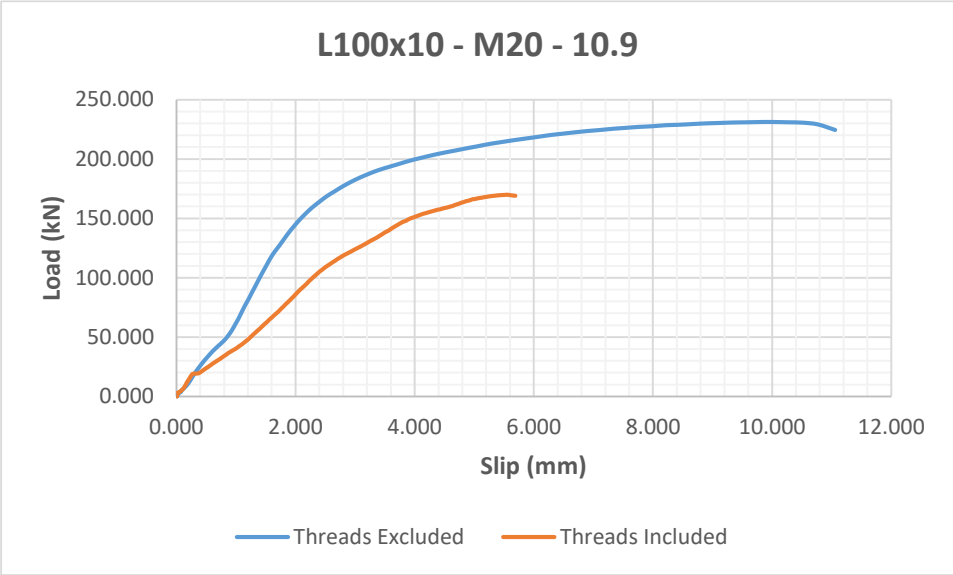

Figure 2.28: Specimen 3 (threads excluded) and specimen 23 (threads included) comparison

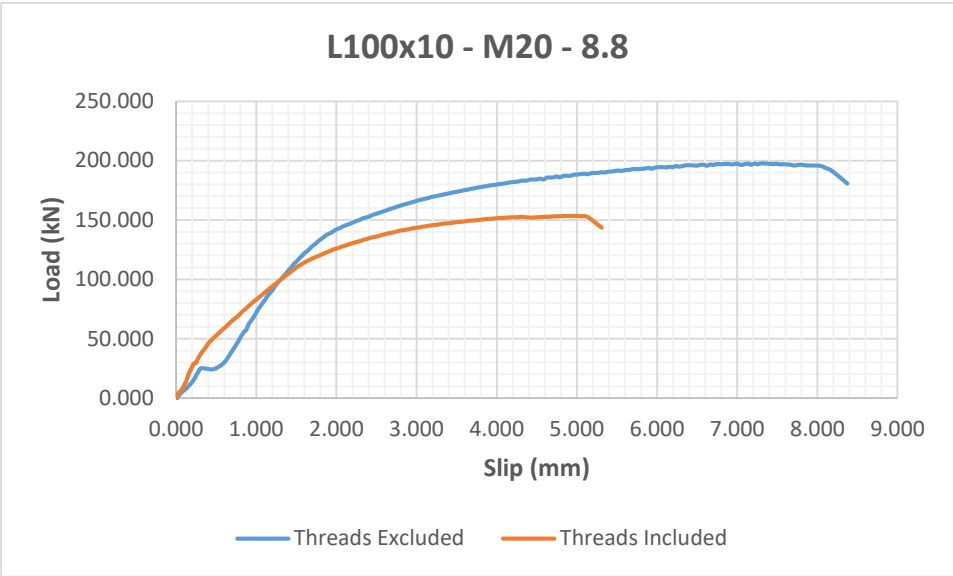

Figure 2.29: Specimen 4 (threads excluded) and specimen 24 (threads included) comparison

With the inclusion of threads in the shear plane, the load-carrying capacity of the bolts reduced by 20%, according to AISC (2016). Since the connectors used in specimens 2, 3, 4, 22, 23, and 24, shown in Figure 2.27, Figure 2.28, and Figure 2.29, were L100x10 with high stiffness, capacity reduction of the bolts caused by the

inclusion of threads in shear plane reduced the slip and load-carrying capacities. However, the connecters used in specimens 13 and 21, shown in Figure 2.26, were L60x60 with lower stiffness, and the load-carrying and slip capacities of specimens were similar.

To observe the effects of the loading direction, the comparison graphs of the specimens with front and back loadings are given in Figure 2.30, Figure 2.31, and Figure 2.32. In order to double-check the investigation of the behavior of the back loading, the comparison of repetitive specimens 17 and 20 were compared and given in Figure 2.33.

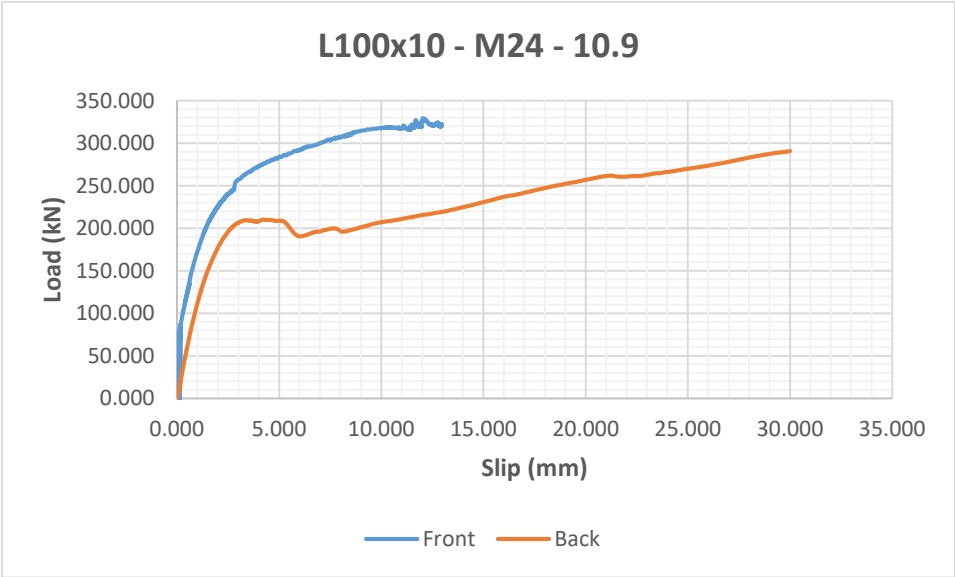

Figure 2.30: Specimen 1 (front loading) and specimen 17 (back loading) comparison

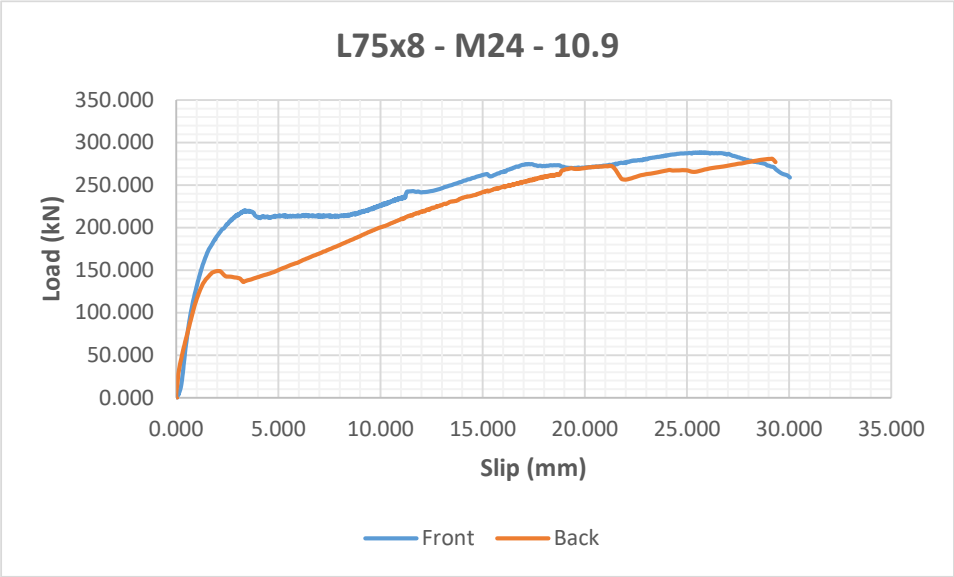

Figure 2.31: Specimen 5 (front loading) and specimen 18 (back loading) comparison

Figure 2.32: Specimen 9 (front loading) and specimen 19 (back loading) comparison

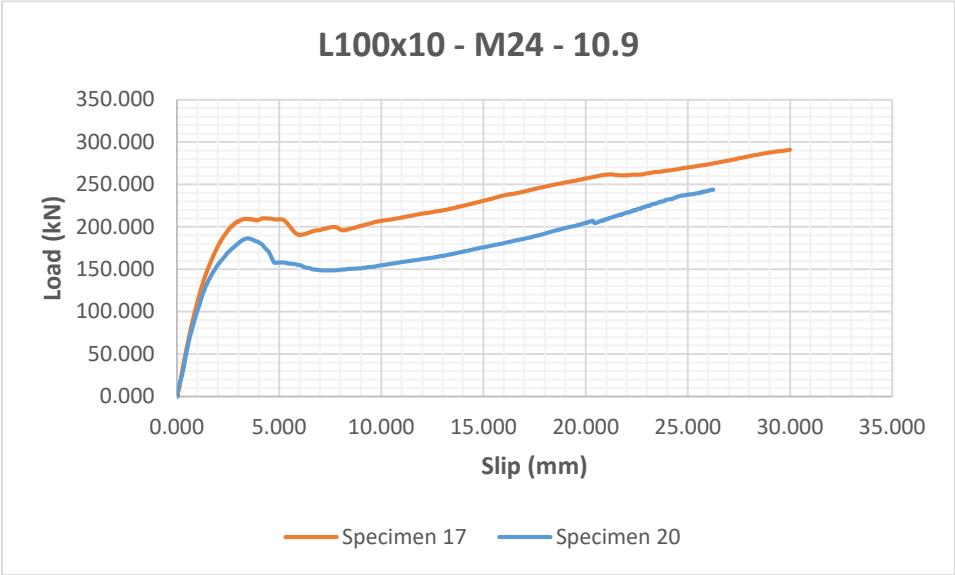

Figure 2.33: Specimen 17 (back loading) and specimen 20 (back loading) comparison

According to the results, back loading caused a decrease in initial stiffness. In larger angle sizes, i.e., L100x10 and L75x8, load-carrying capacity decreased with the change of the loading direction; meanwhile, in smaller angle sizes, i.e., L70x7 and L60x6, load-carrying, and slip capacities did not show any significant change.

The differences in capacities between companion specimens were around 20%, according to Figure 2.33. This can be attributable to the local variations of concrete strength.

To ease the understanding of the interpretations regarding the change of load-carrying behavior of specimens with the change of concrete quality, the load versus slip displacement graphs of the identical specimens with different concrete qualities are given in Figure 2.34, Figure 2.35, Figure 2.36, Figure 2.37, Figure 2.38, Figure 2.39, Figure 2.40, Figure 2.41, and Figure 2.42 for L100x10, L75x8, and L60x6 with the combinations of the bolts M24 grade 8.8, M20 grade 10.9, M20 grade 8.8, respectively.

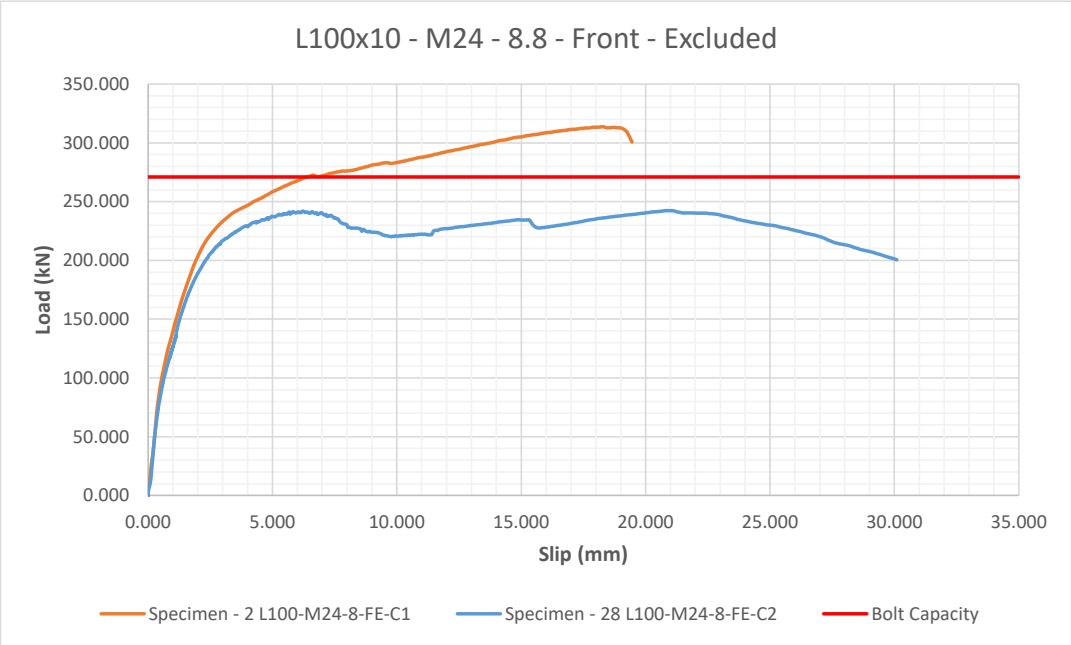

Figure 2.34: Specimen 2 (C1) and specimen 28 (C2) comparison

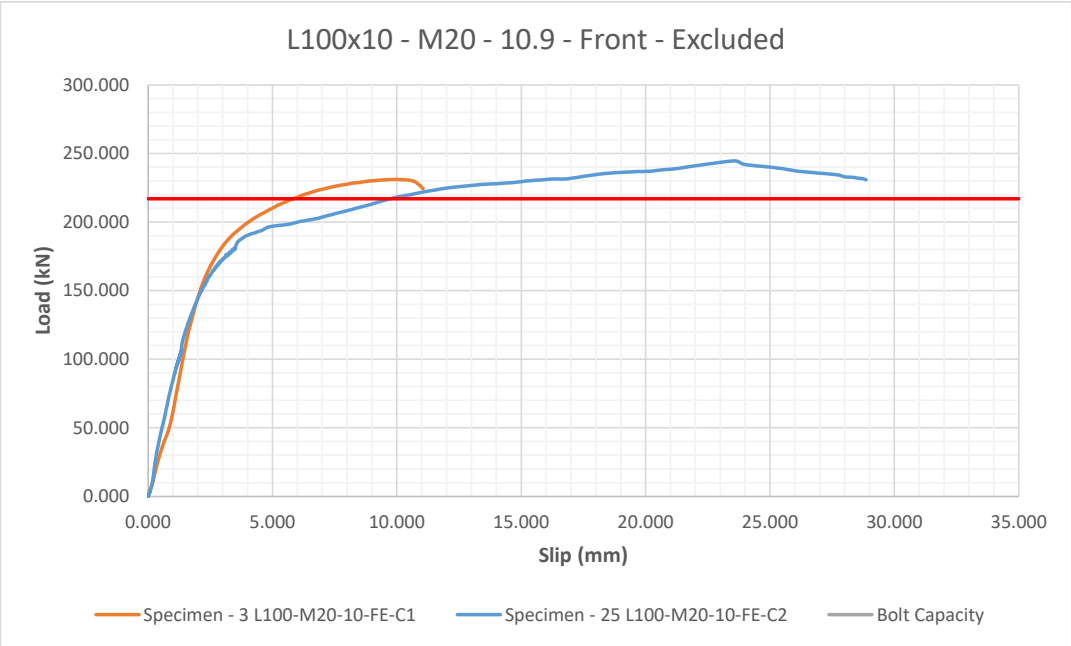

Figure 2.35: Specimen 3 (C1) and specimen 25 (C2) comparison

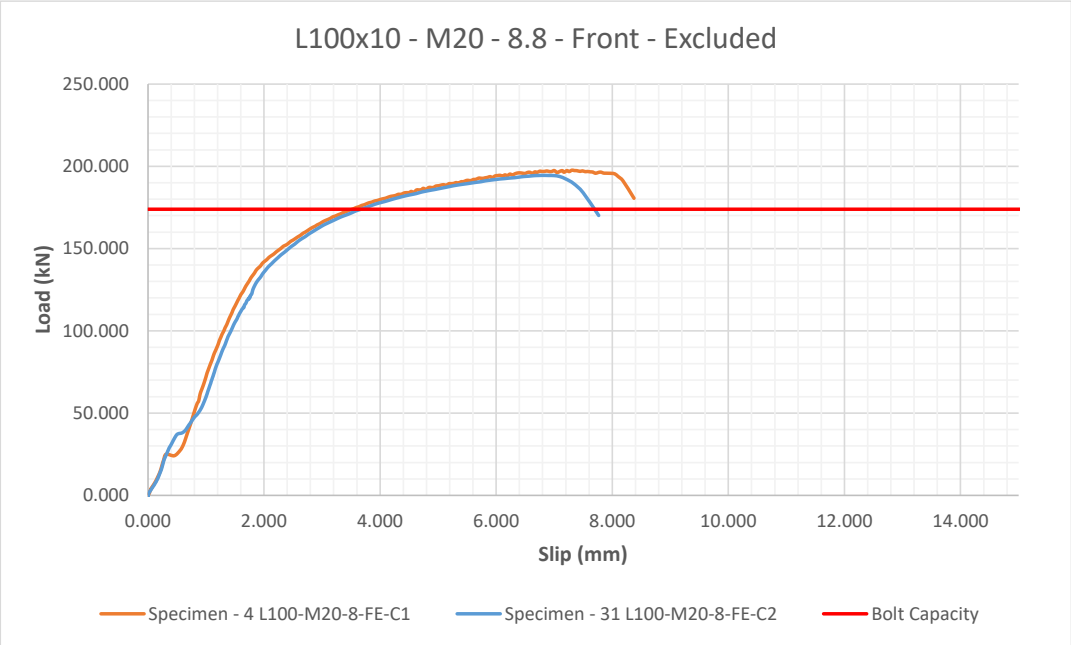

Figure 2.36: Specimen 4 (C1) and specimen 31 (C2) comparison

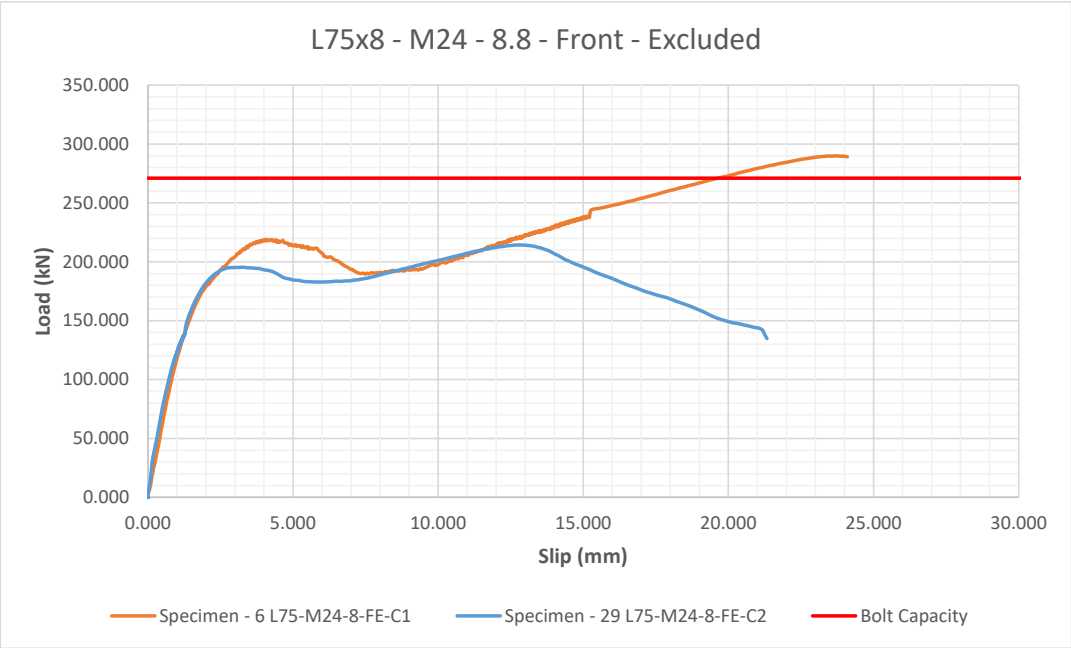

Figure 2.37: Specimen 6 (C1) and specimen 29 (C2) comparison

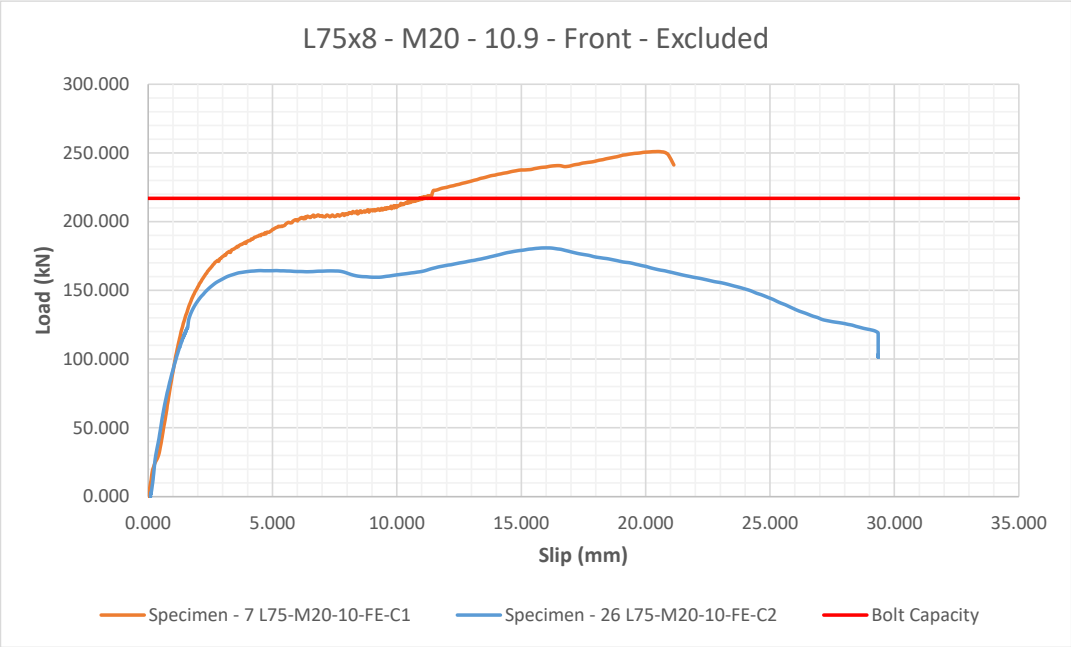

Figure 2.38: Specimen 7 (C1) and specimen 26 (C2) comparison

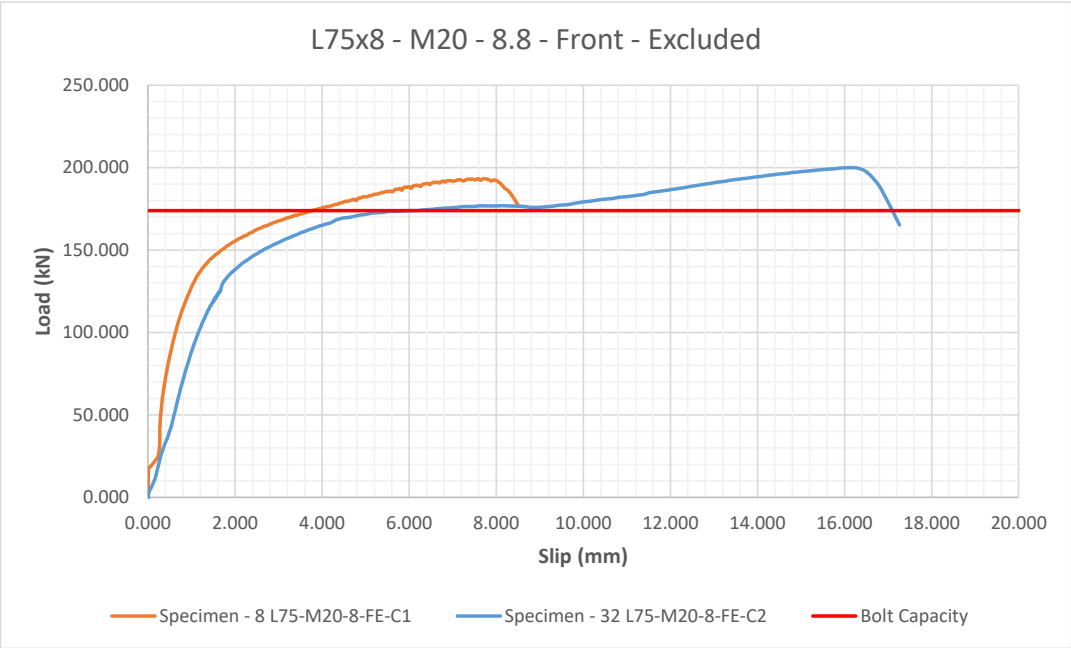

Figure 2.39: Specimen 8 (C1) and specimen 32 (C2) comparison

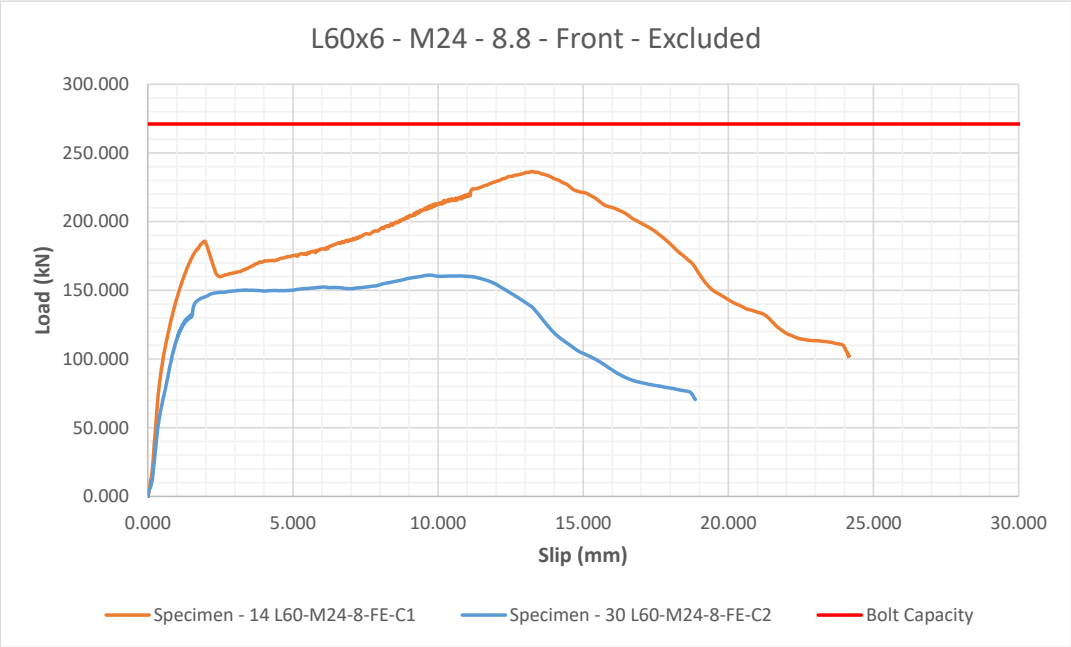

Figure 2.40: Specimen 14 (C1) and specimen 30 (C2) comparison

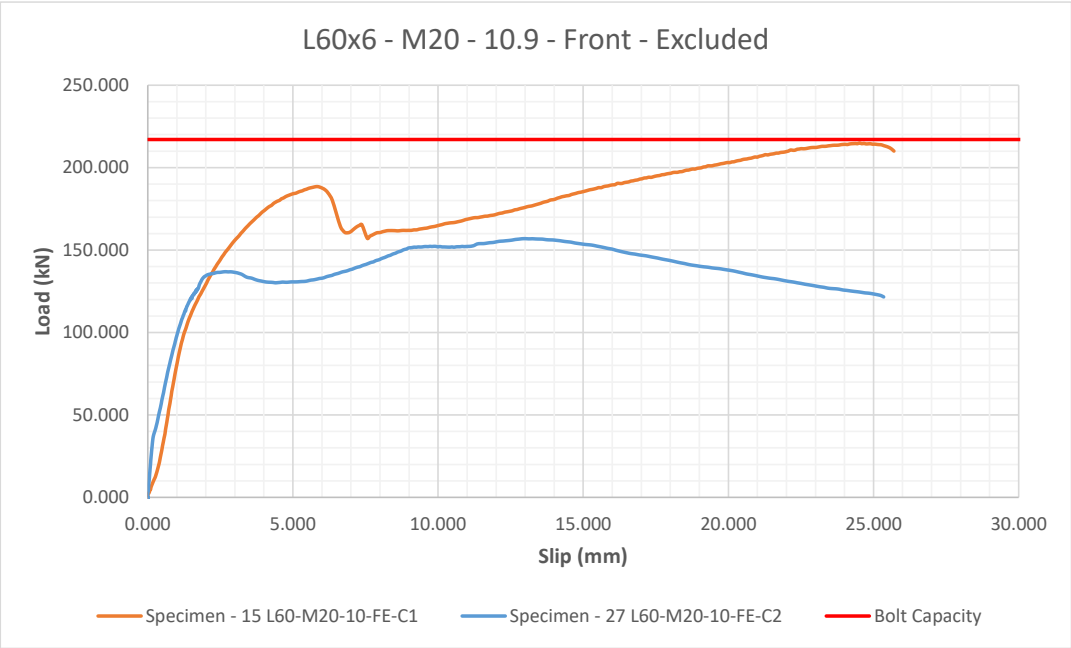

Figure 2.41: Specimen 15 (C1) and specimen 27 (C2) comparison

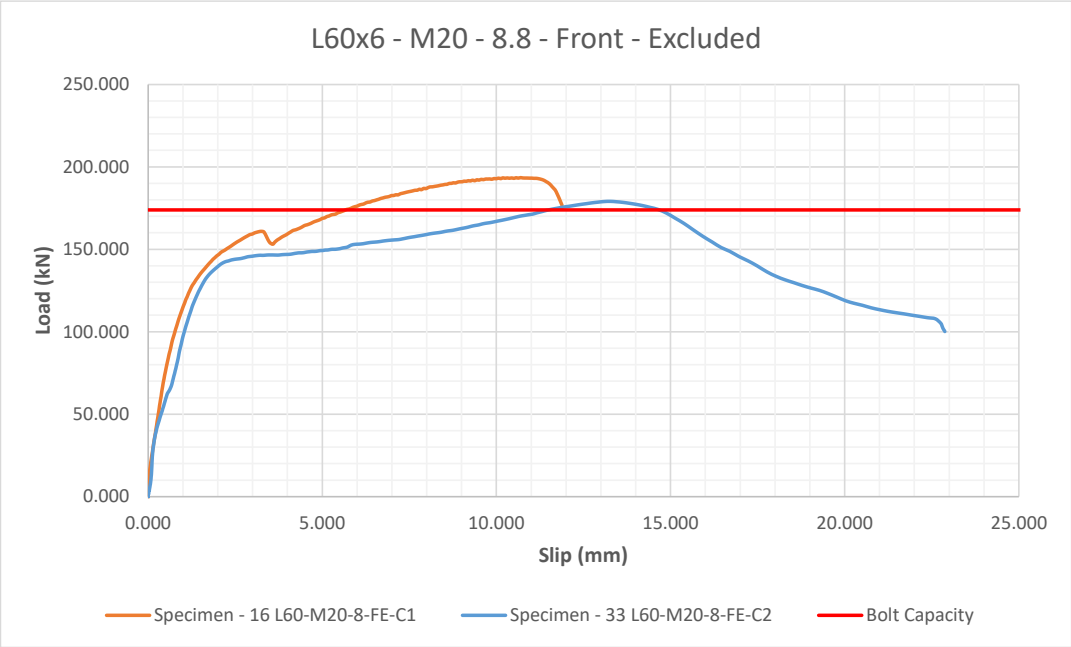

Figure 2.42: Specimen 16 (C1) and specimen 33 (C2) comparison

M24 grade 10.9 bolts were not included in the design of the specimens in the second batch since the second batch specimens were planned to be tested with lower concrete quality, and the capacity provided by M24 grade 10.9 bolts would be unnecessarily high. However, since the capacity difference between the concrete batches was around 35%, the concrete crushing was predominant for the second batch specimens. Therefore, the ductility and slip displacement capacity of the specimens of the second batch was higher. Additionally, the specimens with higher concrete quality had higher load-carrying capacity.

As mentioned, Eurocode 4 (2011) requires a minimum slip capacity of 6 mm as a ductility limitation. However, the composite beams with high degrees of composite action, i.e., more than 75%, are generally expected to show a slip demand of less than 6 mm; meanwhile, beams with low degrees of composite action, i.e., less than 33%, can undergo slip levels of 12 mm. Thus, the applied loads at 3, 6, 9, and 12 mm slip displacements and the maximum load-carrying capacity of specimens were determined. The determined load values are given in Table 2.8.

Table 2.8: Applied loads at 3, 6, 9, and 12 mm and ultimate load capacity

Specimen #	Nomenclature	Bolt Capacity (kN)	3 mm Capacity (kN)	6 mm Capacity (kN)	9 mm Capacity (kN)	12 mm Capacity (kN)	Maximum Capacity (kN)
1	L100-M24-10-FE-C1	317.3	257.6	291.9	314.7	327.1	329.4
2	L100-M24-8-FE-C1	271.0	236.6	268.2	281.5	292.6	313.8
3	L100-M20-10-FE-C1	217.1	184.3	218.6	230.3	-	231.1
4	L100-M20-8-FE-C1	173.9	166.2	194.4	-	-	197.7
5	L75-M24-10-FE-C1	317.3	215.2	213.5	217.7	241.8	288.6
6	L75-M24-8-FE-C1	271.0	204.7	206.7	193.0	215.0	290.0
7	L75-M20-10-FE-C1	217.1	174.9	200.4	207.8	225.0	251.0
8	L75-M20-8-FE-C1	173.9	167.8	188.4	-	-	193.2
9	L70-M24-10-FE-C1	317.3	211.6	173.3	172.8	198.4	227.1
10	L70-M24-8-FE-C1	271.0	204.0	196.1	197.4	216.8	218.3
11	L70-M20-10-FE-C1	217.1	163.3	166.8	180.7	185.8	189.3
12	L70-M20-8-FE-C1	173.9	161.4	184.1	191.5	-	191.8
13	L60-M24-10-FE-C1	317.3	182.5	149.2	165.6	180.1	239.5
14	L60-M24-8-FE-C1	271.0	163.0	180.1	204.5	229.7	236.5
15	L60-M20-10-FE-C1	217.1	156.4	187.4	161.9	171.9	214.9
16	L60-M20-8-FE-C1	173.9	159.8	176.2	190.9	-	193.4
17	L100-M24-10-BE-C1	317.3	207.1	190.7	201.5	215.9	300.9
18	L75-M24-10-BE-C1	317.3	140.7	160.0	190.1	219.4	280.8
19	L70-M24-10-BE-C1	317.3	153.0	181.6	206.4	218.1	248.9
20	L100-M24-10-BE-C1	317.3	181.1	154.3	151.0	161.9	243.8
21	L60-M24-10-FI-C1	253.8	187.1	227.2	223.9	220.4	234.8
22	L100-M24-8-FI-C1	216.8	205.0	231.8	-	-	233.5
23	L100-M20-10-FI-C1	173.7	124.7	-	-	-	169.9
24	L100-M20-8-FI-C1	139.1	143.8	-	-	-	153.6
25	L100-M20-10-FE-C2	217.1	172.7	199.9	213.3	224.8	244.6
26	L75-M20-10-FE-C2	217.1	159.2	163.8	159.6	168.4	180.9
27	L60-M20-10-FE-C2	217.1	136.2	133.2	151.4	155.4	157.0
28	L100-M24-8-FE-C2	271.0	217.3	241.3	223.9	227.0	242.4
29	L75-M24-8-FE-C2	271.0	195.2	182.8	195.6	212.4	214.2
30	L60-M24-8-FE-C2	271.0	149.8	152.4	159.0	152.4	160.9
31	L100-M20-8-FE-C2	173.9	164.3	192.3	-	-	194.5
32	L75-M20-8-FE-C2	173.9	154.6	173.8	176.0	186.7	199.9
33	L60-M20-8-FE-C2	173.9	146.0	153.1	162.8	176.0	179.0

To examine the effects of angle size on load-carrying capacity before reaching the ductility limitation, resistances at 3 mm and 6 mm slip for specimens with C1 concrete quality are given in Figure 2.43 and Figure 2.44,respectively.

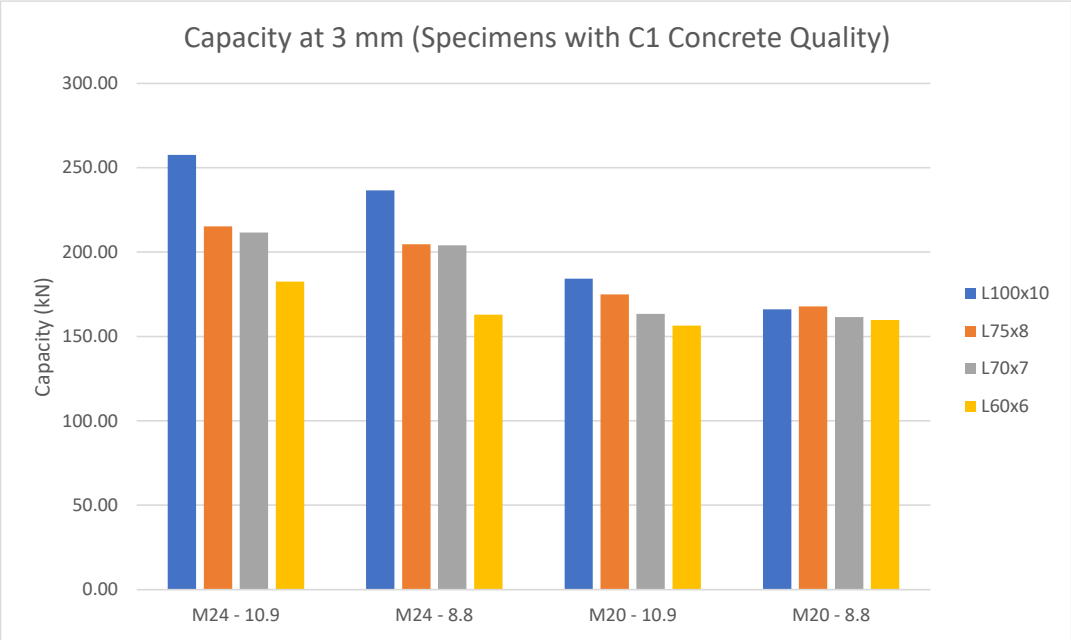

Figure 2.43: Loads at 3 mm slip of specimens with C1 concrete quality (angle size effect)

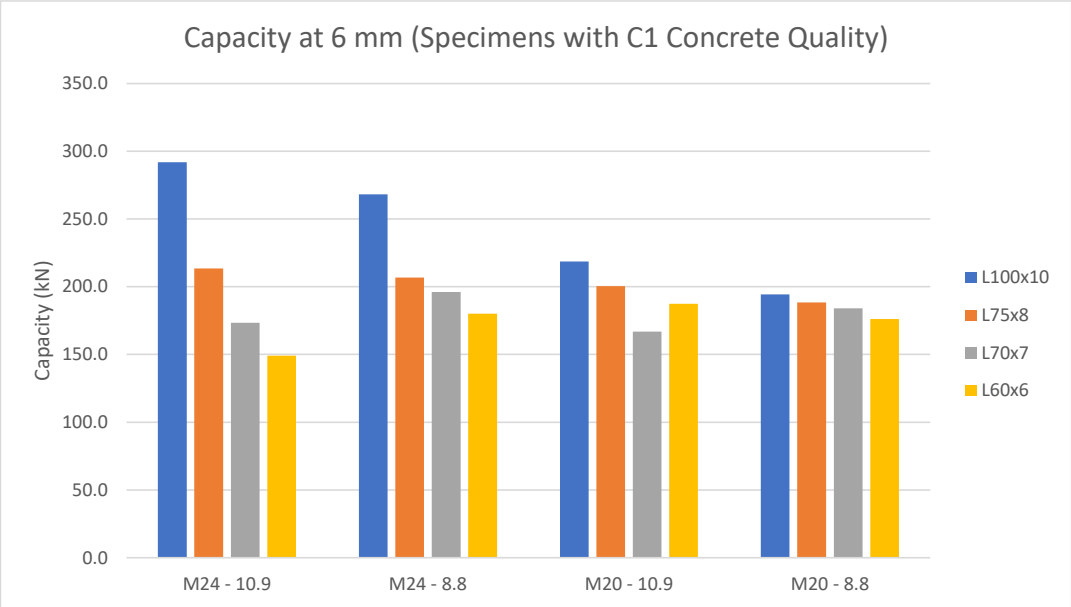

Figure 2.44: Loads at 6 mm slip of specimens with C1 concrete quality (angle size effect)

According to the figures, in short, the load-carrying capacity of the specimens at 3 mm and 6mm slips increased with the increase of angle size.

To examine the effects of angle size on ultimate load-carrying capacity, the ultimate load capacities of specimens with C1 quality concrete are given in Figure 2.45.

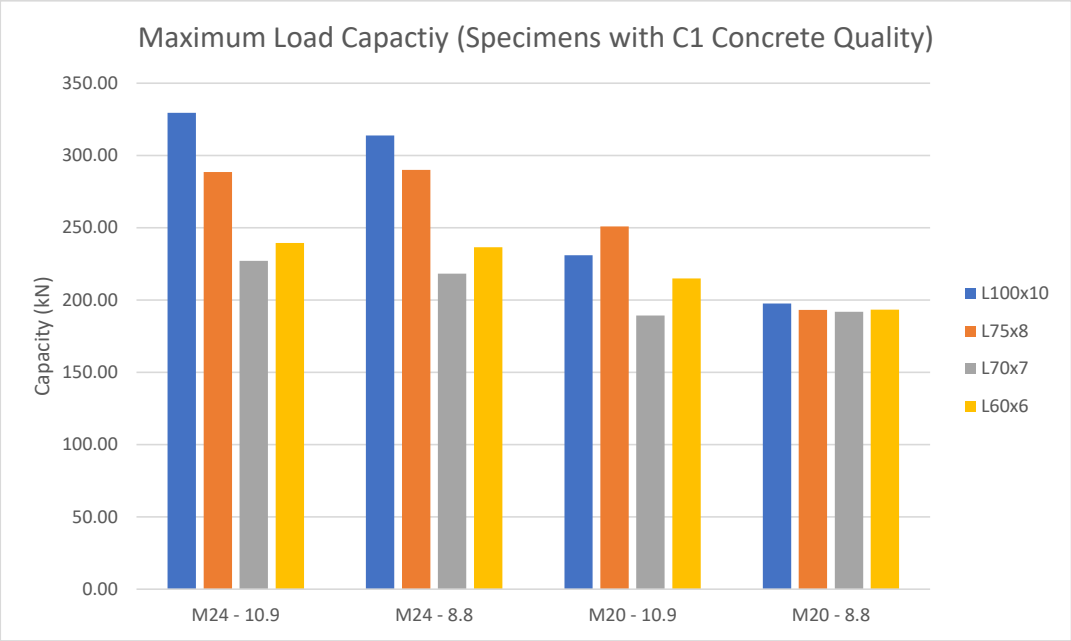

Figure 2.45: Ultimate capacities of specimens with C1 concrete quality (angle size effect)

According to the results, except for the specimens that experienced bolt shear-off, L100x10 angle connectors provided the highest capacity, and capacities decreased with a decrease in the angle size. Exceptionally, L70x7 connectors provided lower capacities compared to the L60x6 connectors, although their thickness was higher. The reason might be the relatively lower yield strength of the angle sections, reported in Table 2.4.

To examine the effects of bolt properties on load-carrying capacity before reaching the ductility limitation, loads carried until 3, and 6 mm for specimens with C1 concrete quality are given in Figure 2.46 and Figure 2.47, respectively.

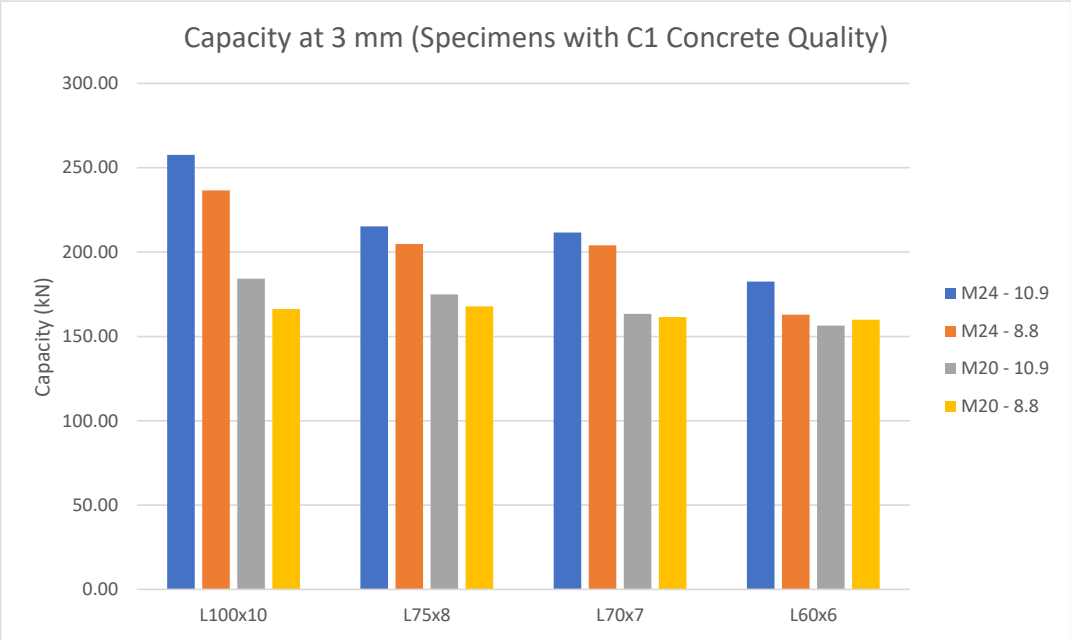

Figure 2.46: Loads at 3 mm slip of specimens with C1 concrete quality (bolt property effect)

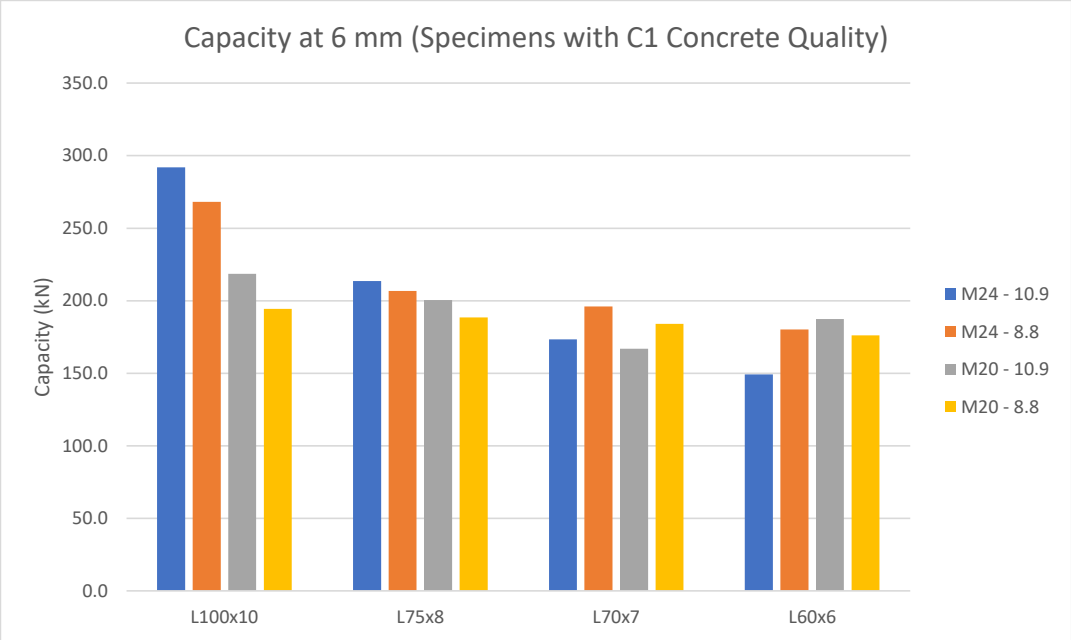

Figure 2.47: Loads at 6 mm slip of specimens with C1 concrete quality (bolt property effect)

According to the figures, in short, the load-carrying capacity of the specimens at 3 mm and 6mm slips increased with the use of stiffer bolts.

To examine the effects of bolt properties on ultimate load-carrying capacity, the ultimate load capacities of specimens with C1 quality concrete are given in Figure 2.48.

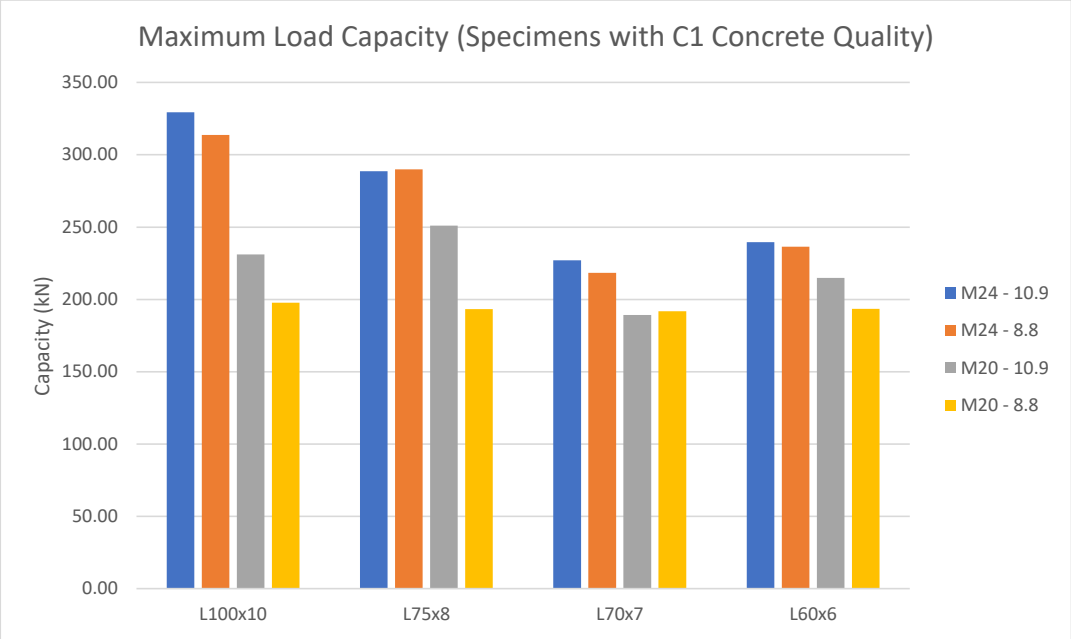

Figure 2.48: Ultimate capacities of specimens with C1 concrete quality (bolt property effect)

According to the results, the ultimate load-carrying capacity of the specimens increased with the increase of the bolt capacity.

The maximum slip displacement of each specimen is given in Figure 2.49 to strengthen the previous interpretations. According to the results, in general, the ductility of the specimens increased with the increase of the bolt capacity and with the decrease of the concrete quality.

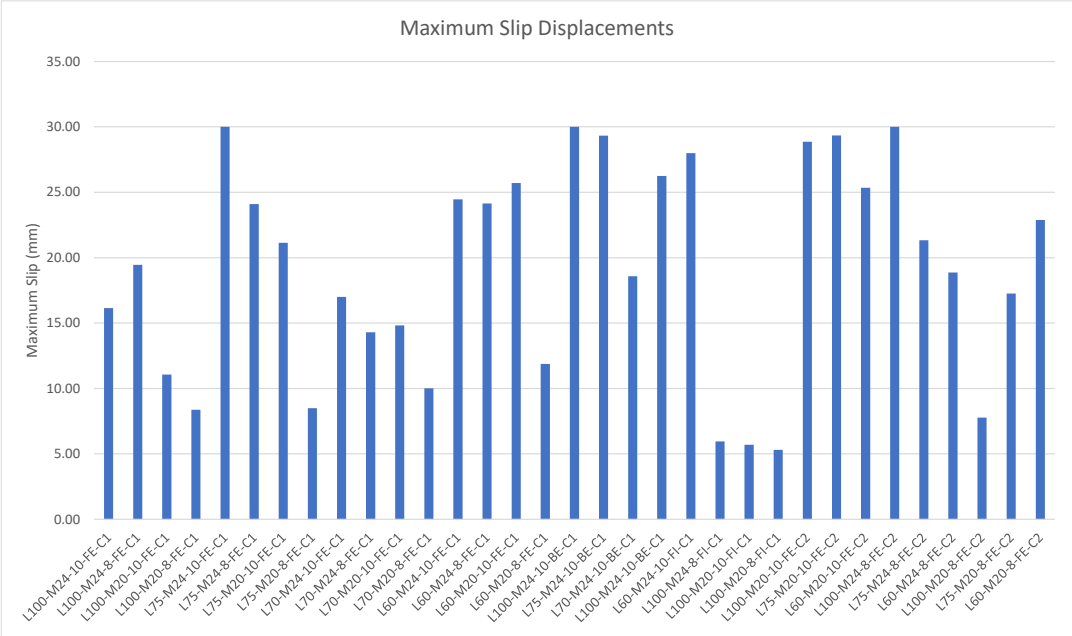

Figure 2.49: Maximum slip displacement of each specimen

The behavior of channel connectors in steel-concrete composite systems were investigated by Arıkoğlu et al. (2020). To evaluate the performance of the proposed connector system, the ultimate capacities of the specimens 1, 5, and 13 were compared with the capacities of channel connectors with similar heights, and the comparison is given in Table 2.9.

Table 2.9: Comparison with channel connectors

Specimen Name	Ultimate Capacity (kN)	Ultimate Slip (mm)	Specimen Name	Ultimate Capacity (kN)	Ultimate Slip (mm)	Capacity Difference (kN)	% Capacity Difference
L100-M24-10-FE-C1	329.4	16.2	UPN100-HSM-50	340.0	18.1	-10.57	-0.03
L75-M24-10-FE-C1	288.6	30.0	UPN80-HSM-50	328.8	15.6	-40.20	-0.14
L60-M24-10-FE-C1	239.5	24.5	UPN65-HSM-50	301.8	13.7	-62.25	-0.26

Where the chosen specimens from Arıkoğlu et al. (2020) had a connector width of 50 mm and high strength mortar (HSM) filling material with the compressive strength of 40.7 MPa.

According to the comparison, the proposed connector system had less stiffness against slip due to the high stiffness provided by the welded connections. Additionally, since the filling material used in the design of channel connectors had

relatively higher compressive strength, the ultimate capacity of the connectors was influenced in a positive manner. Nevertheless, the proposed system had similar behavior and slip capacity, which showed that bolted angle shear connectors were a strong alternative for welded connection systems.

2.3.3 Recommendations for Capacity Prediction

To predict the ultimate load-carrying capacity of the connectors at 6 mm slip, the specimens that experienced bolt shear-off failure were neglected. The average capacities, standard deviations (ST), and coefficient of variations (COV) of remaining specimens were calculated according to the size of angle sections and given in Table 2.10 and Table 2.11 for series 1 and 2, respectively.

Table 2.10: Series 1 - average load, ST, and COV

Series 1				
Specimen Name	**Load at 6 mm Displacement (kN)**	**Average Load (kN)**	**Standard Deviation (kN)**	**Coefficient of Variation (-)**
L100-M24-10-FE-C1	291.9	280.0	16.8	0.06
L100-M24-8-FE-C1	268.2			
L100-M20-10-FE-C1	NDBS			
L100-M20-8-FE-C1	NDBS			
L75-M24-10-FE-C1	213.5	206.9	6.5	0.03
L75-M24-8-FE-C1	206.7			
L75-M20-10-FE-C1	200.4			
L75-M20-8-FE-C1	NDBS			
L70-M24-10-FE-C1	173.3	178.7	15.4	0.09
L70-M24-8-FE-C1	196.1			
L70-M20-10-FE-C1	166.8			
L70-M20-8-FE-C1	NDBS			
L60-M24-10-FE-C1	149.2	172.2	20.3	0.12
L60-M24-8-FE-C1	180.1			
L60-M20-10-FE-C1	187.4			
L60-M20-8-FE-C1	NDBS			
NDBS: Neglected due to Bolt Shear-off				

Table 2.11: Series 2 - average load, ST, and COV

Series 2				
Specimen Name	**Load at 6 mm Displacement (kN)**	**Average Load (kN)**	**Standard Deviation (kN)**	**Coefficient of Variation (-)**
L100-M24-8-FE-C2	241.3	220.6	29.3	0.13
L100-M20-10-FE-C2	199.9			
L100-M20-8-FE-C2	NDBS			
L75-M24-8-FE-C2	182.8	173.5	9.5	0.05
L75-M20-10-FE-C2	163.8			
L75-M20-8-FE-C2	173.8			
L60-M24-8-FE-C2	152.4	146.3	11.3	0.08
L60-M20-10-FE-C2	133.2			
L60-M20-8-FE-C2	153.1			
NDBS: Neglected due to Bolt Shear-off				

The average load-carrying capacities of each series were compared and given in Table 2.12. Since the calculated coefficient of variations were low, less than 15%, average loads were directly used without any modification in comparison.

Table 2.12: Comparison of series – 6 mm

Comparison			
L Shape Size	**Average Load - Serie 1 (kN)**	**Average Load - Serie 2 (kN)**	**Ratio (Serie2/Serie1)**
L100x10	280.0	220.6	0.79
L75x8	206.9	173.5	0.84
L60x6	172.2	146.3	0.85
Average			0.83

The ratio between concrete qualities was calculated using Equation 2.2.

$$r = \sqrt{\frac{f_{c-series\ 2}}{f_{c-series\ 1}}} \tag{2.2}$$

$$r = \sqrt{\frac{28.7}{39.1}} = 0.86$$

The similarity of the average of calculated load ratios and the concrete strength ratio showed that the load-carrying capacity of the proposed connectors at 6 mm slip could be predicted for any concrete strength by using the load capacities of series 1 specimens which were 280 kN, 206.9 kN, and 172.2 kN for L100x10, L75x8, and L60x6 connectors, respectively.

The same procedure was followed for the capacities at 3- and 9- mm slip displacements. The obtained capacity comparison between the series 1 and series 2 specimens is given in Table 2.13 and Table 2.14 for 3mm slip and 9 mm slip, respectively.

Table 2.13: Comparison of series – 3 mm

Comparison			
L Shape Size	**Average Load - Serie 1 (kN)**	**Average Load - Serie 2 (kN)**	**Ratio (Serie2/Serie1)**
L100x10	247.3	194.8	0.79
L75x8	198.3	169.6	0.86
L60x6	167.3	143.9	0.86
Average			0.83

Table 2.14: Comparison of series – 9 mm

Comparison			
L Shape Size	**Average Load - Serie 1 (kN)**	**Average Load - Serie 2 (kN)**	**Ratio (Serie2/Serie1)**
L100x10	297.8	218.5	0.73
L75x8	206.2	177.2	0.86
L60x6	177.4	157.6	0.89
Average			0.83

The comparison between the tables of 3-, 6-, and 9- mm slips showed that the increase in the average shear load-carrying capacity of the specimens, with the increase of the slip displacement, was small. Additionally, the average of the series 1 and series 2 capacity ratios did not change with the slip displacement increase, indicating that the prediction method is accurate.

CHAPTER 3

PULL-OUT TESTS

In this chapter, an experimental investigation of the proposed shear connectors is made via pull-out tests conducted at the Structural Mechanics Laboratory of the Department of Civil Engineering at Middle East Technical University. These tests are the second phase of the experimental study and aim to understand the behavior and the tensile load-carrying capacity of the connectors.

3.1 Test Setup

The technical drawings of the test setup are given in Figure 3.1, and the photos are indicated in Figure 3.2. The test setup was designed to conduct a pull-out test on a typical connector, which is embedded into a concrete block. The setup was configured as a self-contained system that does not require any reaction wall or a vertical support system. The loading was applied by making use of a 600 kN capacity hydraulic jack. The applied load was measured by making use of a 1000 kN capacity load cell which is mounted on the top of the hydraulic jack. The load was transferred from the hydraulic jack to a rod with a 27 mm diameter which is connected to the shear connector embedded into the concrete.

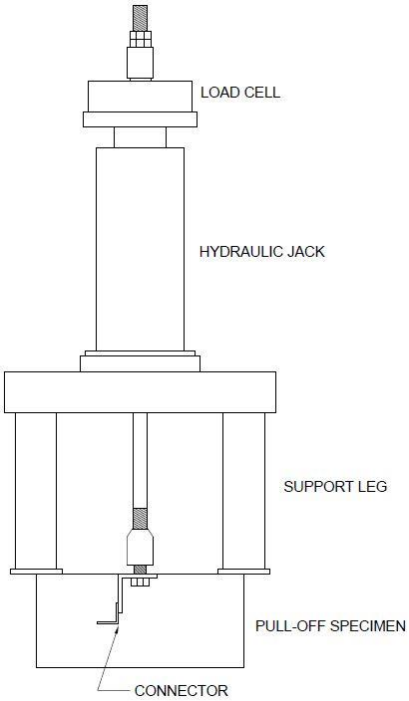

Figure 3.1: Test setup

Figure 3.2: Photos of the test setup: a) General view - 1, b) General view - 2, c) During test - 1, d) During test - 2

A typical test specimen consists of a square concrete block of 400 mm side length. The high-strength bolt used in the proposed connector extends out of the concrete block. A freely extending bolt was connected to the loading rod with a special transmitter produced for the test setup. A concrete cone type of failure, which has a failure radius of effective connector height, was expected while designing the test setup. Hence, the distance between supporting legs, shown in Figure 3.1, was designed long enough for not to prevent the concrete cone failure.

Two European channel UPN80 sections of 400 mm length were welded to a 150×100 mm steel plate with a 40 mm spacing between the channels to construct the support legs, as shown in Figure 3.3. The reaction beam located at the top of the supporting legs had the same orientation of the legs, shown in Figure 3.3. The 40 mm gap was ensured to provide enough spacing for the 27 mm diameter loading rod to pass through it.

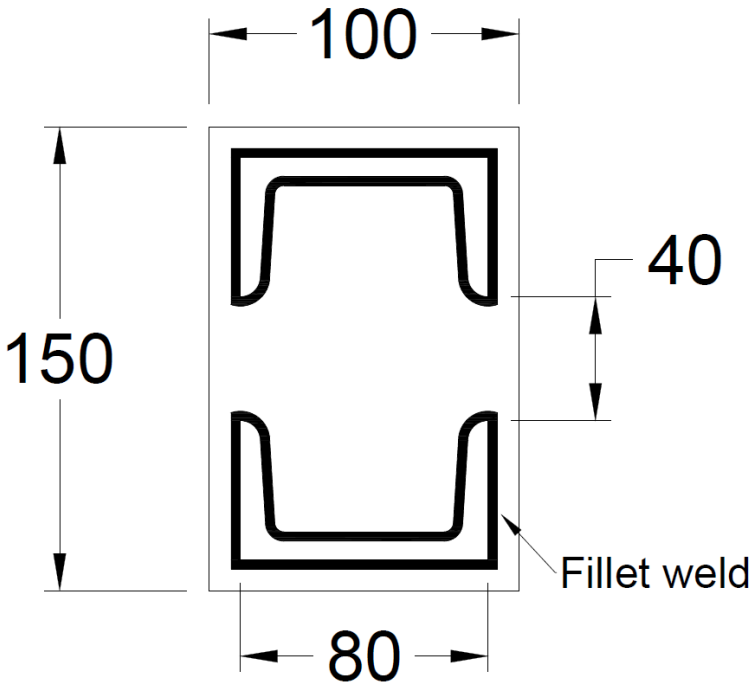

Figure 3.3: Supporting leg top view

3.1.1 Orientation of Data Recording Instruments

The applied load and the vertical displacement of the connector were monitored during a typical test. Two extension legs were welded to the transmitter. Two LVDTs were placed at the ends of the extension legs connected to the transmitter, as shown in Figure 3.4. The differential vertical displacement can be directly calculated by making of these two independent readings.

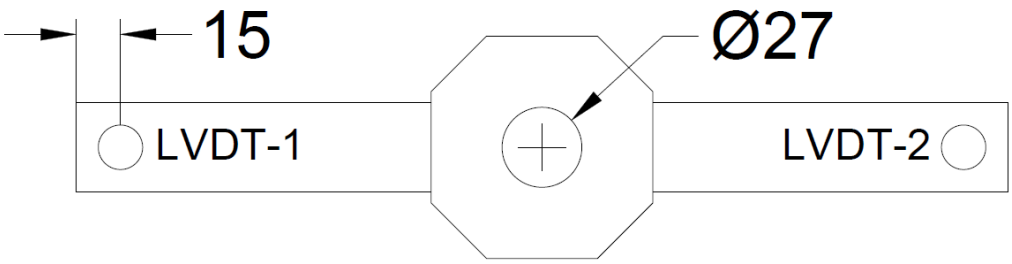

Figure 3.4: Orientation of LVDTs

3.2 Test Specimens

The pull-out experiments conducted in the literature were constructed with a concrete block supported by steel sections from top and bottom. The concrete block was clamped to the floor beam by two square sections and bolted to the top beam with investigated mechanical anchorages. However, in this study, a different test setup with a similar working mechanism was used. Thus, the design of the test specimens varied compared with the ones in the literature.

The concrete blocks used in test specimens had a square shape with 400 mm dimension and 180 mm thickness. Four 8 mm diameter bars were used as steel reinforcement in the long and short directions. These were placed symmetrically at the top and bottom surfaces, as shown in Figure 3.5. A total of 6 specimens were designed and the parameters considered are given in Section 3.2.1.

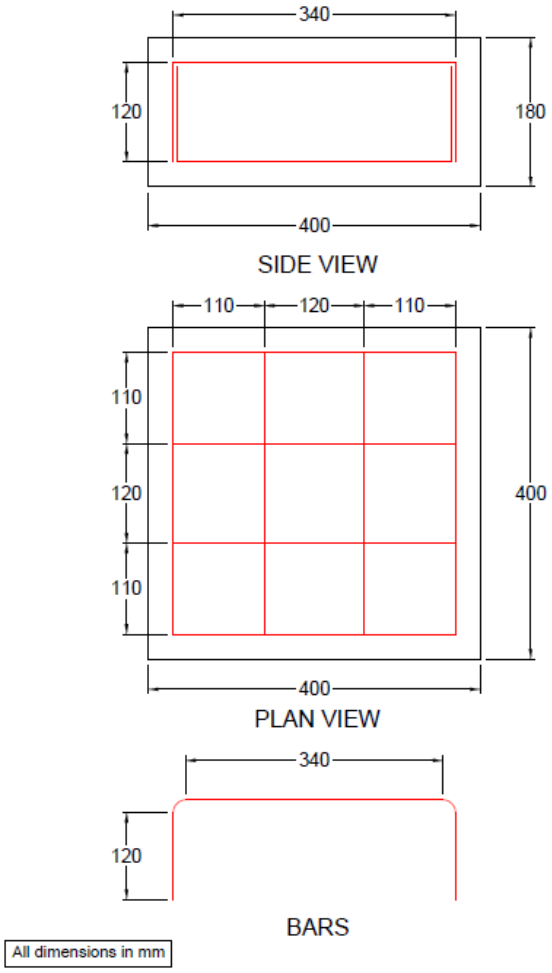

Figure 3.5: Reinforcement layout

3.2.1 Design Parameters

The size of the angle sections was the main parameter considered. Changes in the section sizes resulted in the change in total height, which enabled an increase in tension resistance. Detailed tabulated information about the specimens is given in Table 3.1. European angle sections L100×10, L75×8, L60×6, L40×4, and L30×3 with 50 mm width were used in the testing program. The leg size of the lower section was selected considering the applicability in beam specimen production, and the total

height is limited to stay in between the applicable deck height limits. M24 high-strength bolts with 10.9 grade were considered.

The nomenclature used for identifying the specimens is as follows: the first entry is used for the size of the lower angle section, where L100 is for L100×10 and L75 is for L75×8, the second entry is used for the size of the upper angle section 75 is for L75×8, 60 is for L60×6, 40 is for L40×4, and 30 is for L30×3, the third entry is for the total height of the specimen, and it is used as given in Table 3.1; although bolt diameter and bolt strength are not taken as parameters, in the nomenclature, the fourth entry is for bolt diameter where M24 refers to 24 diameter bolt, and the fifth entry is for bolt strength where 10 refers to 10.9 grade bolt.

For example, specimen 3 L100-40-120-M24-10 is a specimen with an L100×10 lower angle section, L40×40 upper angle section, a total height of 120 mm, and an M24 10.9 grade bolt. The list of all nomenclatures is given in Table 3.2.

Table 3.1: Experiment matrix for pull-out specimens

Specimen #	L Shape Size (mm)	Total height (mm)	Bolt Grade	Bolt diameter (mm)
1	L75 & L30	85	10.9	24
2	L75 & L40	95	10.9	24
3	L100 & L40	120	10.9	24
4	L75 & L60	115	10.9	24
5	L100 & L60	140	10.9	24
6	L100 & L75	155	10.9	24

Table 3.2: Specimen nomenclatures

Specimen #	Nomenclature	Specimen #	Nomenclature	Specimen #	Nomenclature
1	L75-30-85-M24-10	2	L75-40-95-M24-10	3	L100-40-120-M24-10
4	L75-60-115-M24-10	5	L100-60-140-M24-10	6	L100-75-155-M24-10

The upper angle sections were welded to lower angle sections using fillet welds with a constant welding leg of 20 mm. In other words, the angle sections overlap with each other by 20 mm. Bolt holes were introduced into the lower angle sections by making use of a drill bit. The size of the holes was equal to the bolt diameter. In other

words, there was no tolerance between the bolt hole and the bolt. An explanatory drawing of specimen 1 is given in Figure 3.6.

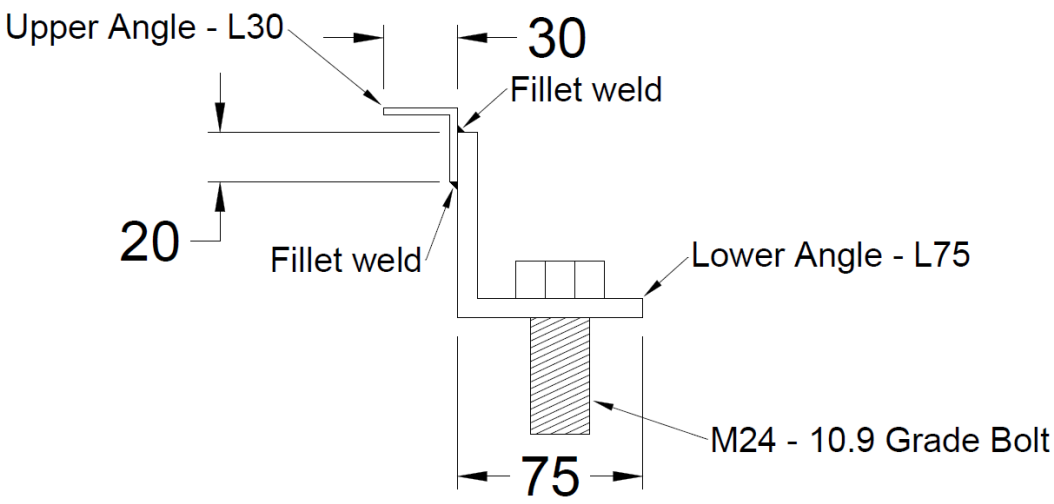

Figure 3.6: Specimen 1 (L75-30-85-M24-10)

Design specimens included combinations of the same lower angle section with different upper angle sections and the same upper angle section with different lower angle sections to understand the contributions of sections separately. Additionally, similar total heights constructed with different combinations were considered to understand whether the capacity depended on the upper angle section or total height.

3.2.2 Geometric and Material Properties

The angle sections with properties reported in Table 2.3 were used. The tensile strength of the angles is given in Table 2.4, and the stress-strain responses are given in Figure 2.7. The ultimate tensile strength of the bolts is given in Table 2.5.

The specimens were prepared with the second batch of push-out specimens, so the compressive strength of the concrete was 28.7 MPa.

3.3 Test Results

A total of six pull-out specimens, explained in Table 3.1, were tested. The conducted experiments had a single phase, and specimens were loaded to failure.

3.3.1 Observed Failure Modes

According to ACI (2014), the tensile load-carrying capacity of an embedded anchorage can be calculated by using the concrete cone method. Equation 3.1 was used for a single stud and no haunch system.

$$N_{cbg} = \frac{A_{Nc}}{A_{Nco}} * \psi_{ec,N} * \psi_{ed,N} * \psi_{c,N} * N_b \tag{3.1}$$

Where N_{cbg} is the load-carrying capacity in kips, A_{Nco} is the tributary area of the anchorage and calculated using Equation 3.2, A_{Nc} is the tributary area with haunch, and it is equal to A_{Nco} for designs with no haunch, $\psi_{ec,N}$ is eccentricity factor, and 1 for concentric loading, $\psi_{ed,N}$ is height factor and 1 for the cases where one and a half times of the connector height is less than 12 inches, $\psi_{c,N}$ is the haunch factor and 1 for the cases with no haunch, and N_b is the concrete tensile strength for an embedded anchorage and calculated using Equation 3.3.

$$A_{Nco} = 9 * h_{ef}^2 \tag{3.2}$$

$$N_b = k_c * \sqrt{f_c} * h_{ef}^{1.5} \tag{3.3}$$

Where in Equation 3.3, k_c is 24 for cast-in-place anchors, f_c is the compressive strength of the concrete on the 28th day, and h_{ef} is the effective length of the anchorage.

The concrete cone strength of the specimens was calculated and given in Table 3.3. With the use of the capacities and the experimental results given in Table 3.5, true errors and true percent relative errors (ε_t) are given in Table 3.4.

Table 3.3: Concrete cone strength of specimens

	Specimen 1	Specimen 2	Specimen 3	Specimen 4	Specimen 5	Specimen 6
h_{ef} (mm)	85.00	95.00	120.00	115.00	140.00	155.00
h_{ef} (in)	3.35	3.74	4.72	4.53	5.51	6.10
f_c (MPa)	28.70	28.70	28.70	28.70	28.70	28.70
f_c (psi)	4162.58	4162.58	4162.58	4162.58	4162.58	4162.58
k_c (-)	24.00	24.00	24.00	24.00	24.00	24.00
N_b (lbs)	9481.48	11199.54	15898.55	14919.43	20038.10	23342.07
A_{nco} (in^2)	100.82	125.89	200.85	184.53	273.44	335.15
A_{nc} (in^2)	100.82	125.89	200.85	184.53	273.44	335.15
$\psi_{ec,N}$	1	1	1	1	1	1
$\psi_{ed,N}$	1	1	1	1	1	1
$\psi_{c,N}$	1	1	1	1	1	1
N_{cbg} (lbs)	9481.48	11199.54	15898.55	14919.43	20038.10	23342.07
N_{cbg}(kN)	42.18	49.82	70.72	66.36	89.13	103.83

Table 3.4: Comparison between capacities and errors

Specimen Name	Experimental Capacity (kN)	Theoretical Capacity (kN)	True Error (E_t)	ε_t (%)
L75-30-85-M24-10	50.80	42.18	8.62	16.98
L75-40-95-M24-10	59.08	49.82	9.26	15.68
L100-40-120-M24-10	73.80	70.72	3.08	4.17
L75-60-115-M24-10	90.35	66.36	23.99	26.55
L100-60-140-M24-10	79.87	89.13	-9.26	-11.60
L100-75-155-M24-10	87.66	103.83	-16.17	-18.45

According to the errors given in Table 3.4, it can be said that the theoretical method underestimated the load-carrying capacity of the connectors with a total height of less than 120 mm since the bending of the upper angle section provided additional strength.

The failure of the specimens occurred in two phases. Bending of the lower angle section was observed, as shown in Figure 3.7 followed by breaking off the concrete cone, as shown in Figure 3.8.

Figure 3.7: Failure mode - phase 1

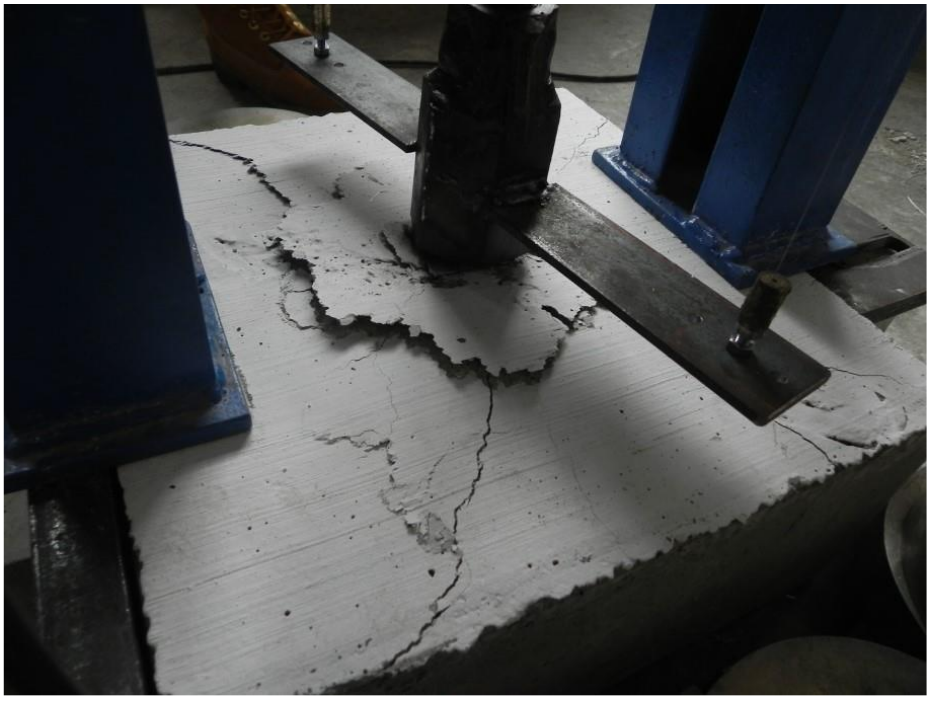

Figure 3.8: Failure mode - phase 2

3.3.2 Behavior Under Tensile Load

The pull-out displacement response of specimens under tensile applied loads is given in Figure 3.9, Figure 3.10, Figure 3.11, Figure 3.12, Figure 3.13, and Figure 3.14 for specimens 1 to 6, respectively.

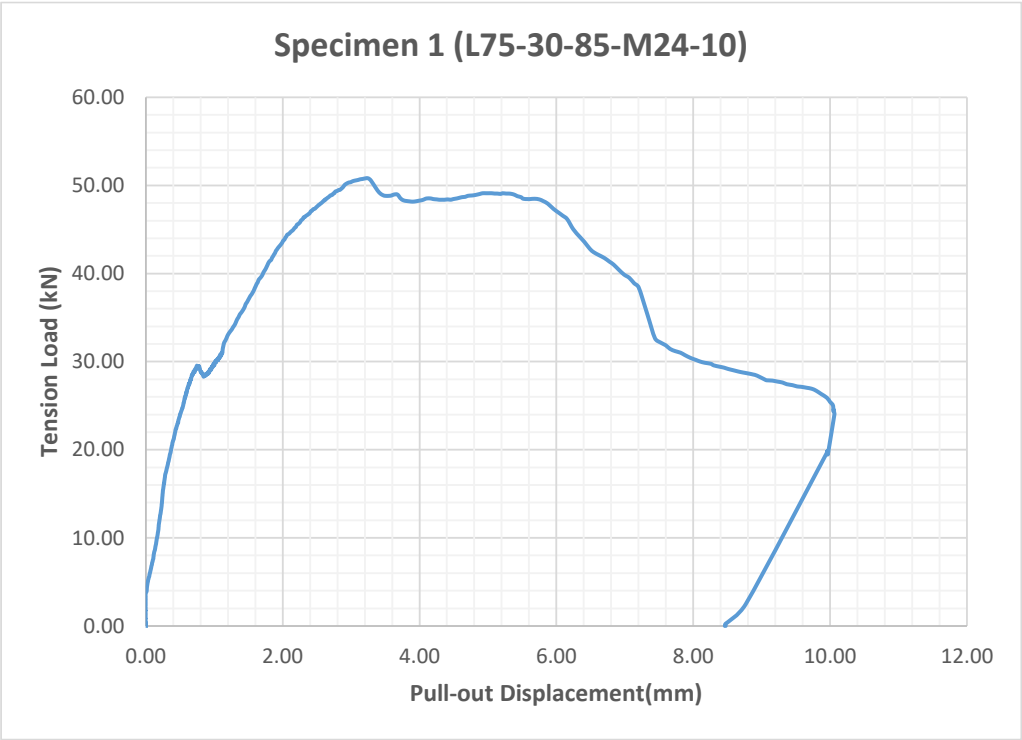

Figure 3.9: Specimen 1 - load vs. pull-out displacement

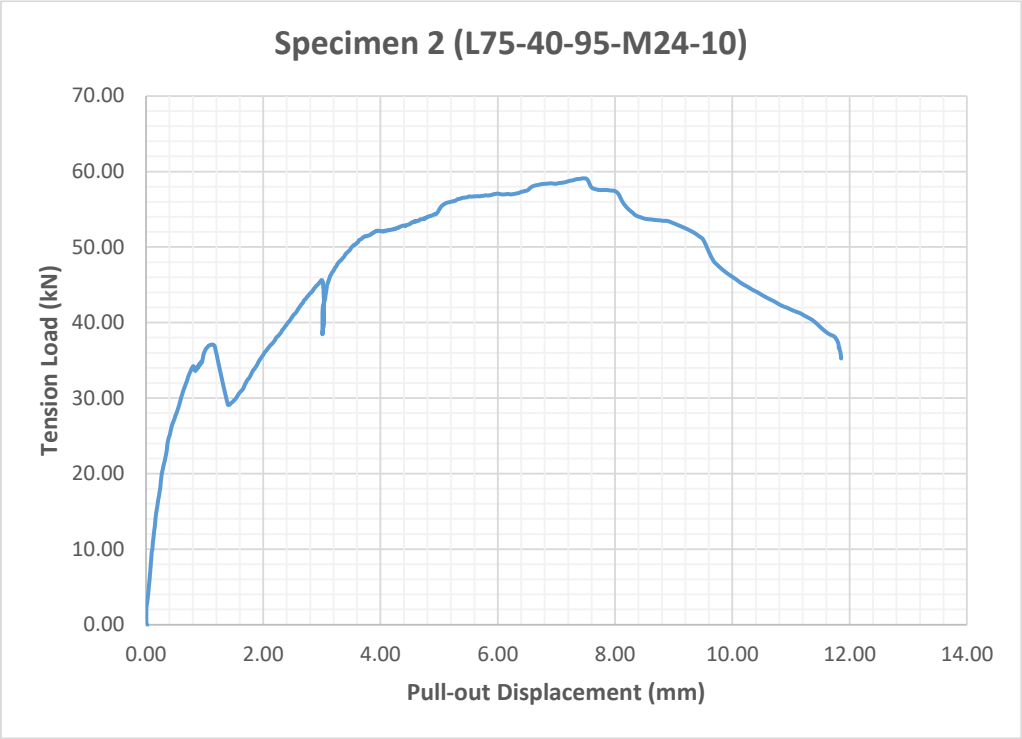

Figure 3.10: Specimen 2 - load vs. pull-out displacement

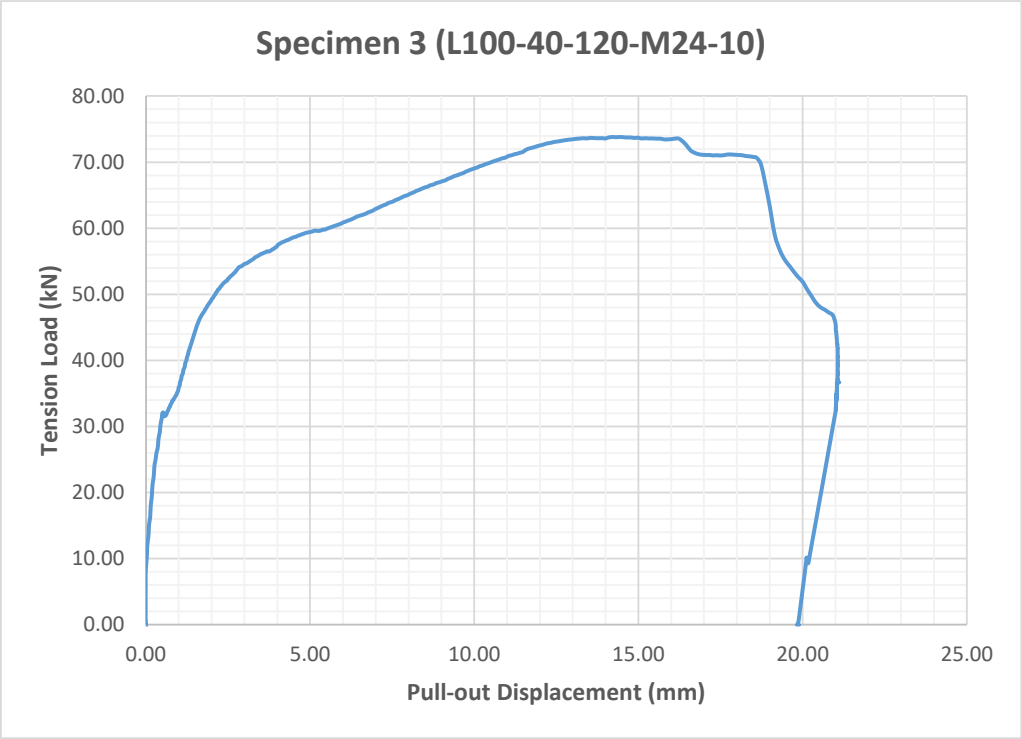

Figure 3.11: Specimen 3 - load vs. pull-out displacement

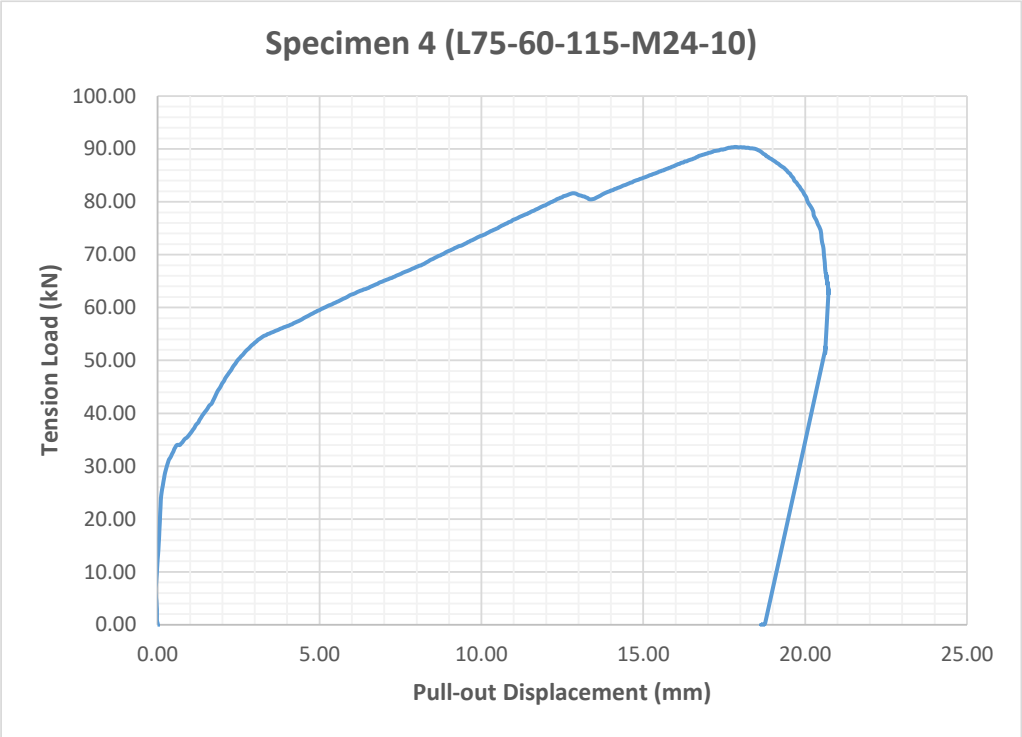

Figure 3.12: Specimen 4 - load vs. pull-out displacement

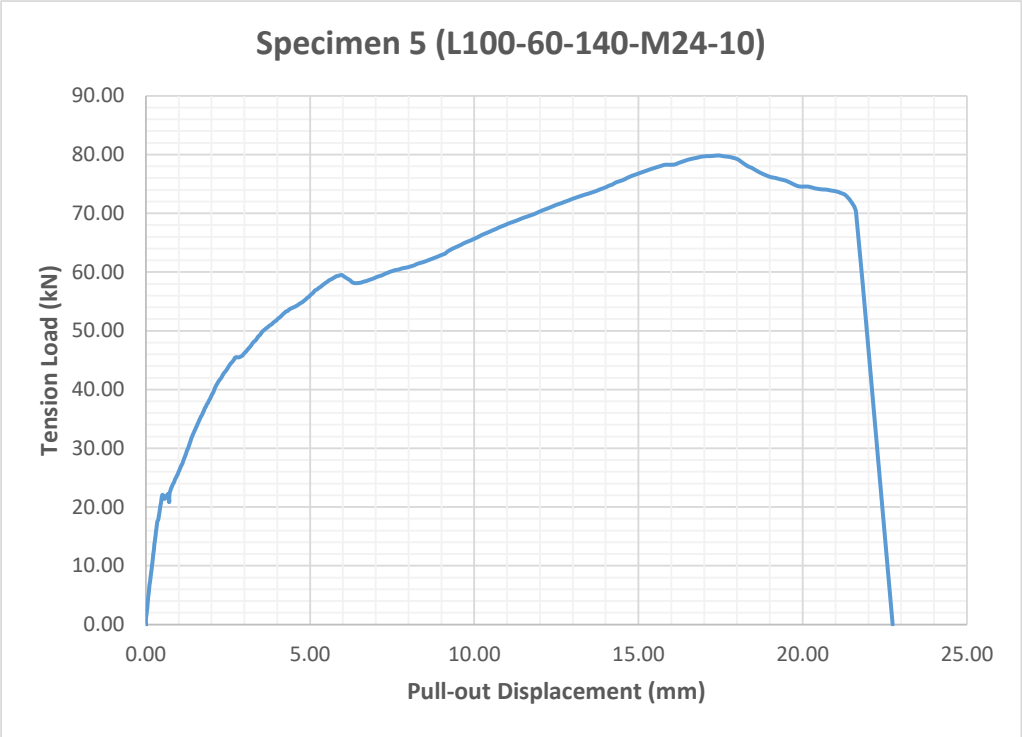

Figure 3.13: Specimen 5 - load vs. pull-out displacement

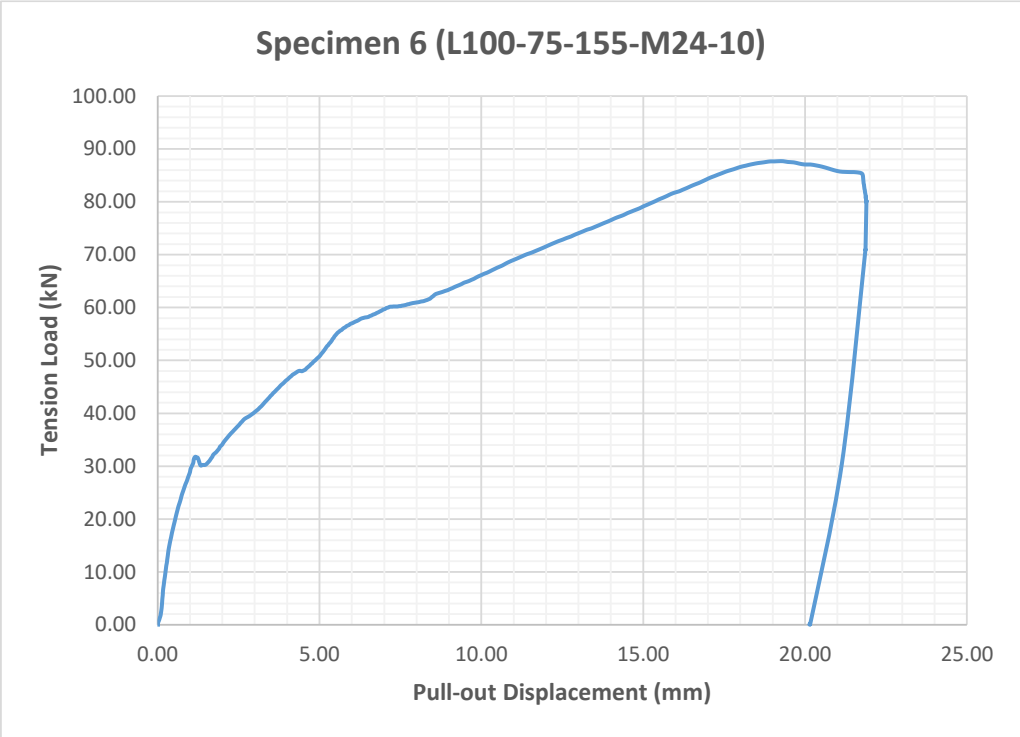

Figure 3.14: Specimen 6 - load vs. displacement

The specimens showed similar load-displacement behavior. According to the results, it can be seen that until an applied load of 20 kN, all specimens had a linear load-displacement response.

To ease the understanding of the interpretations regarding the ultimate behavior of specimens, the load versus pull-out displacement curves of all specimens are combined in a single graph, which is given in Figure 3.15. The comparison between specimens 1, 2, and 3 showed that increasing the total height of the specimens resulted in a higher load-carrying capacity. However, since members were expected to carry mainly shear forces in composite beam design, maximum favorable vertical deformation can be limited to 5 mm, although most of the specimens had a deformation capacity higher than 20 mm. In this manner, the comparison between specimens 5 and 6 showed that the increase in the total height of the connectors increased the capacity until a certain point that concrete strength became the governing factor. Additionally, the comparison between specimens 3 and 4, which had similar total heights, showed that in the means of capacity, an increase in the

size of the upper angle section was more beneficial compared to an increase in the size of the lower angle section.

On the other hand, considering the tensile capacity of the demountable headed studs with an embedment depth of 120 mm reported by Tan et al. (2019), i.e., 60 kN, all specimens have reached very satisfactory capacity limits.

Figure 3.15: Applied load vs. pull-out displacement curves of all specimens

The maximum load-carrying capacity, displacement at maximum load, maximum displacement capacity, and load carried at 5- and 10-mm displacements of each specimen are given in Table 3.5.

Table 3.5: Maximum load and displacements

Specimen Nomenclature	P_{max} (kN)	Δ at P = P_{max} (mm)	$Δ_{max}$ (mm)	P at Δ = 5 mm (kN)	P at Δ = 10 mm (kN)
L75-30-85-M24-10	50.80	3.25	10.06	49.11	25.42
L75-40-95-M24-10	59.08	7.46	13.88	55.22	45.73
L100-40-120-M24-10	73.80	14.21	21.12	59.49	69.09
L75-60-115-M24-10	90.35	17.82	20.72	59.67	73.61
L100-60-140-M24-10	79.87	17.46	21.62	56.14	66.03
L100-75-155-M24-10	87.66	19.32	21.90	50.88	66.06

According to the results given in Table 3.5, specimen 1, which was used in the design of beam specimens, reached its peak capacity at 3.25 mm and had an ultimate load-carrying and displacement capacities of 50.80 kN and 10 mm, respectively.

CHAPTER 4

BEAM BENDING TESTS

In this chapter, an experimental investigation of the proposed shear connectors is made via beam bending tests conducted at the Structural Mechanics Laboratory of the Department of Civil Engineering at Middle East Technical University. These tests are the third phase of the experimental study and aim to understand the behavior and the responses in real-life applications.

4.1 Test Setup

A single-point loading test setup was developed to conduct beam bending experiments. The technical drawing of the test setup is given in Figure 4.1, and the photos are indicated in Figure 4.2.

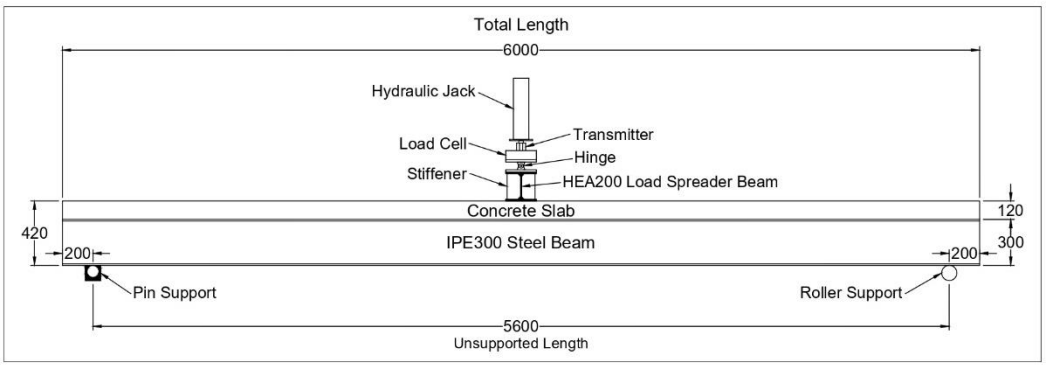

Figure 4.1: Test setup

The loading was applied by making use of a 600 kN capacity hydraulic jack. The non-stationary end of the hydraulic jack was attached to a steel frame, as shown in Figure 4.2a. The applied load was measured by making use of a 1000 kN capacity load cell which is mounted on the stationary end of the hydraulic jack. The load was

transferred from the hydraulic jack to a transmitter, which is fabricated specially for connecting the hydraulic jack and the load cell. Then, the load was transferred from the transmitter to the load cell. Finally, the load was transferred from the load cell to a hinge, which is used to stabilize the system against any rotation effects, and from the hinge to the HEA200 load spreader beam, which is used to spread the load to prevent excessive load concentrations that may cause local concrete crushing. Additionally, after some experiments, a rotation prevention system, shown in Figure 4.2b, was added to the system. The working mechanism of the rotation prevention system is limiting the vertical deformation (deflection) capacity of the concrete deck of the composite beam at the ends.

Figure 4.2: Photos of the test setup: a) General view, b) Rotation prevention system and LVDTs, c) Loading instruments, d) Strain gauges

A typical test specimen consists of a steel IPE300 beam and a concrete block that is connected to the steel beam using the proposed shear connectors with 6000x800x120 mm length, width, and height dimensions, respectively. Since the tensile capacity of the proposed connectors, investigated in Chapter 3, was satisfactory for not observing tensional failure, a clamping mechanism was not used; however, in some situations requiring the prevention of concrete splitting, a clamping mechanism may be considered to prevent concrete splitting.

4.1.1 Details of Data Recording Instruments

The applied load, the vertical deflection, the slip at the interface of the steel beam and concrete deck, and the strain values of the steel beam were monitored during a typical test.

Eight LVDTs were placed to measure the slip, LVDT-2 to LVDT-10, as shown in Figure 4.2b and Figure 4.3. Two LVDTs were placed in the middle to measure the vertical deflection at the midspan at the backside and frontside, as shown in Figure 4.3. Two LVDTs were placed at the quarters to measure the vertical deflection at the quarter spans, as shown in Figure 4.3. Five strain gauges were placed at the bottom of the top flange, the web of steel section, and the bottom of the bottom flange to measure the strain values on the steel beam. The number of relative slips and deflections, the rotation of the concrete block, and the strain profile through the loading can be directly calculated by making of these readings.

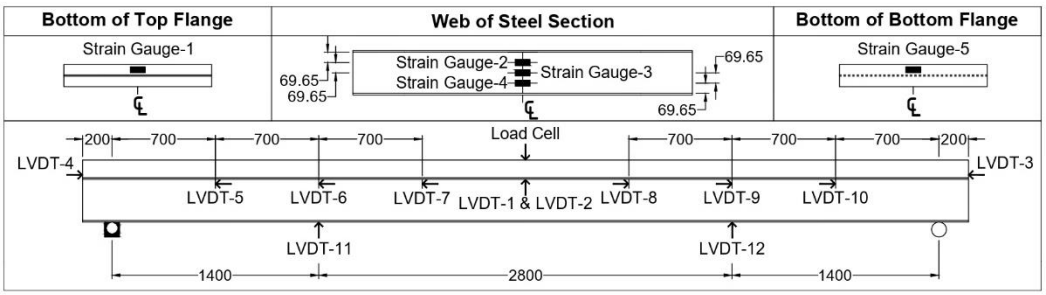

Figure 4.3: Orientation of LVDTs and strain gauges

4.2 Test Specimens

The beam specimens were prepared using the proposed shear connectors. The wire mesh reinforcements with 6 mm diameter and 150x150 mm square openings were used for reinforcing the concrete deck. The wire mesh was placed in two symmetric layers to the top and bottom, as shown in Figure 4.4. Bolted angle shear connectors were fastened to a 10.7 mm thick flange of European steel I-section, IPE300. A total of 4 specimens were designed and the parameters considered are given in Section 4.2.1. A plastic sheet was placed above the steel beam to prevent the bonding of concrete to the I-section and to eliminate friction at the interface.

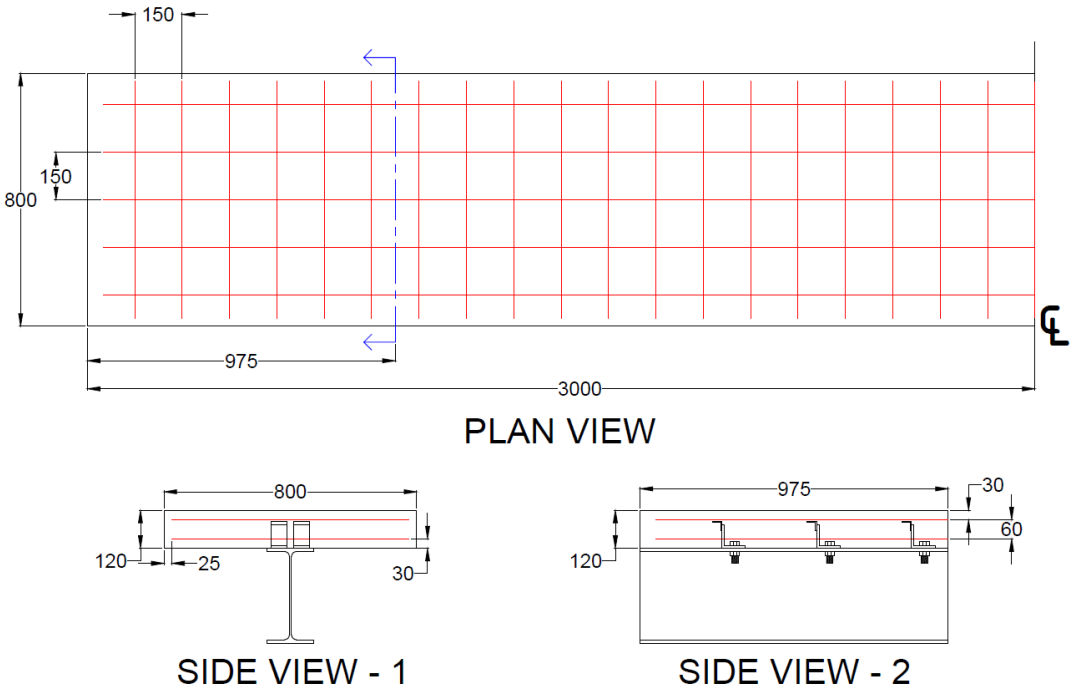

Figure 4.4: Reinforcement layout

4.2.1 Design Parameters

The size of the angle section, degree of composite action, bolt grade, the inclusion of hole tolerance, and bolt thread condition were considered as the prime variables. Detailed tabulated information about the specimens is given in Table 4.1. European

angle sections L100×10 and L75×8 with 50 mm width were used in the testing program. M20 high-strength bolts with 8.8 and 10.9 grades were considered.

The nomenclature used for identifying the specimens is as follows: the size of the angle section where L100 is for L100×10 and L75 is for L75×8, the second entry is used for the target degree of composite action where 100 is used for 100% composite, 50 is used for 50% composite, and 25 is used for 25% composite, the third entry is for the bolt strength where 8 and 10 stand for 8.8 and 10.9 grade bolts, respectively, the fourth entry is the inclusion of the hole tolerance, NT and 2T stand for "no tolerance" and "2 mm tolerance", respectively and the fifth entry stands for thread condition where E and I stand for "excluded" and "included," respectively.

For example, specimen 1 L75-100-10-NT-E is a specimen with an L75×8 angle section, 100% aimed degree of composite action, M20 10.9 grade bolt, no hole tolerance, and threads are excluded from the shear plane. The list of all nomenclatures is given in Table 4.2.

Table 4.1: Experiment matrix for beam bending specimens

Specimen #	Connector Used	Bolt Grade	Bolt diameter (mm)	Target Degree of Composite Action (%)	Push-out Capacity (kN) (Q_n)	Additional Information	# of connectors per half span	Total # of connectors
1	L75	10.9	20	100	180.93	-	9	18
2	L75	10.9	20	50	180.93	-	5	10
3	L75	10.9	20	25	180.93	2 mm hole tolerance	3	6
4	L100 - cut	8.8	20	25	158.14	L shape cut to h = 75 mm Threads Included	3	6

Table 4.2: Specimen nomenclatures

Specimen #	Nomenclature	Specimen #	Nomenclature
1	L75-100-10-NT-E	2	L75-50-10-NT-E
3	L75-25-10-2T-E	4	L100-25-8-NT-I

The first 3 specimens were designed to have a failure mode of concrete crushing, and the last specimen was designed to have a failure mode of bolt shear-off since specimen 4 had M20 8.8 grade bolts with threads included in the shear plane, which created considerably lower shear load-carrying capacity. To accomplish a design with threads included in the shear plane, three washers were placed between the steel section and the bolt. Additionally, specimen 4 was constructed with L100 angle

connectors cut to have a height of 75 mm to provide applicability to decks with 100 mm height since AISC (2016) states that a clear cover provided for shear connectors in the design of composite members should be accordance with ACI (2014) and in ACI (2014), the required minimum concrete cover is defined as ¾ inches, i.e., 19 mm.

The effect of hole tolerance and change in angle size on initial stiffness can be observed with the comparisons of specimens 2 and 3, and specimens 3 and 4, respectively. The effect of the degree of composite action on load-carrying capacity can be observed with the comparison of specimens 1 and 2.

In AISC (2016), it is stated that the degree of composite action could be calculated by Equation 4.1.

$$Degree\ of\ Composite\ Action = \frac{\sum Q_n}{\min\left(A_s F_y, 0.85 f_c' A_c\right)} \tag{4.1}$$

Where Q_n is the shear strength of the connector, A_s is the area of the steel section, F_y is the yield strength of the steel section, f'_c is the concrete compressive strength, and A_c is are of concrete block.

The calculation of the required number of shear connections for a target degree of composite action and back-calculation of composite ratio with the designed beam specimens will be given in Section 4.2.3 with the use of Equation 4.1.

4.2.2 Geometric and Material Properties

The angle sections with properties reported in Table 2.3 were used. The tensile strength of the angles is given in Table 2.4, and the stress-strain responses are given in Figure 2.7. The ultimate tensile strength of the bolts is given in Table 2.5.

Since all steel beam sections were ordered from the same batch, only one of them is measured with a caliper to identify the geometric properties of the I-section, IPE300, as reported in Table 4.3. The dimensions conformed to the EN10034 (1993)

standard. The coupons used to conduct tensile tests to determine load-carrying capacity were extracted from the same I-section according to EN10002 (2001). The obtained material properties are indicated in Table 4.4.

Table 4.3: IPE300 section dimensions

IPE 300 Steel Beam					
Flange Width (b_f) (mm)					
Left End		Right End		Average	Tabulated Value
153.54		153.56		153.21	150.00
153.32		153.53			
152.30		153.03			
Web Thickness (t_w) (mm)					
Left End		Right End		Average	Tabulated Value
7.72		7.71		7.72	7.10
7.74		7.74			
7.71		7.69			
Flange Thickness (t_f) (mm)					
Left End		Right End		Average	Tabulated Value
Left	Right	Left	Right	9.99	10.70
10.34	10.12	10.32	10.15		
9.33	10.34	9.34	9.94		
Section Depth (d) (mm)					
Left End		Right End		Average	Tabulated Value
303		303		302	300
302		302			
301		303			

Table 4.4: Material properties of I-section

	$F_{y,0.2}$	F_u	%E
	MPa	MPa	-
$(IPE300 - Web)_{N1}$	303.59	426.49	39.50
$(IPE300 - Web)_{N2}$	308.76	427.47	38.97
$(IPE300 - Web)_{N3}$	306.20	427.32	36.27
IPE300 - Web -Average	306.19	427.09	38.25
$(IPE300 - Flange)_{N1}$	290.48	421.29	19.73
$(IPE300 - Flange)_{N2}$	296.63	429.34	19.66
$(IPE300 - Flange)_{N3}$	292.50	428.76	41.34
IPE300 - Flange -Average	293.20	426.46	26.91

The stress-strain responses obtained from the coupon tests are given in Figure 4.5.

Figure 4.5: Stress versus strain diagram for I-sections

The specimens were prepared with the second batch of push-out specimens, so the compressive strength of the concrete was 28.7 MPa.

The required number of connectors for the aimed degree of composite actions can be calculated using the given properties is given in Table 4.5.

Table 4.5: Back calculated degrees of composite actions

Specimen #	Nomenclature	Aimed Degree of Composite Action (%)	Push-out Capacity (kN) (Q_n)	A_s (mm^2) (Taken from Section Table)	F_y (MPa) (Average of All Coupons- $R_{p0.2}$)	f'c (MPa)	A_c (mm^2) (h*w)	# of connectors per half span	Rounded # of connectors per half span	Total # of connectors	Back Calculated Degree (%)
1	L75-100-10-NT-E	100	180.93	5381	299.69	28.70	96000	8.91	9	18	100.98
2	L75-50-10-NT-E	50	180.93	5381	299.69	28.70	96000	4.46	5	10	56.10
3	L75-25-10-2T-E	25	180.93	5381	299.69	28.70	96000	2.23	3	6	33.66
4	L100-25-8-NT-I	25	158.14	5381	299.69	28.70	96000	2.55	3	6	29.42

The formulation used in the calculation of the required number of connectors per half span is a modified version of Equation 4.1, as given in Equation 4.2.

$$Needed\ Number\ of\ Connectors = \frac{(Composite\ Ratio) * (\min(A_s F_y, 0.85 f_c' A_c))}{Q_n} \quad (4.2)$$

Since the provided number of connectors needs to be an integer, found results are rounded up, which results in the need for a back-calculation to determine the exact degree of composite action of each specimen. Thus, Equation 4.3, a modified version of Equation 4.1, is derived and used in back-calculation of the degree of composite actions given in Table 4.5.

$$Back\ Calculated\ Composite\ Ratio = \frac{(\#of\ Rounded - up\ Connectors) * Q_n}{\min(A_s F_y, 0.85 f_c' A_c)} \quad (4.3)$$

The beam specimens were designed according to the calculated number of connectors per half span. While designing the specimens, the determination of the connector locations was the key issue. Considering the test setup, which is covered in Section 4.2, support locations were specified to be 200 mm shifted through the steel beam. In other words, considering two supports at the ends, the free span of the beams was shortened to 5600 mm. Stiffeners with a height of more than three-quarters of the beam depth were added to the locations which meet the supports on the steel beam to prevent the local crippling phenomenon stated in AISC (2016). In addition, the minimum distance between the connectors was taken as 300 mm, as stated in AISC (2016). The technical drawings of specimens are given in Figure 4.6.

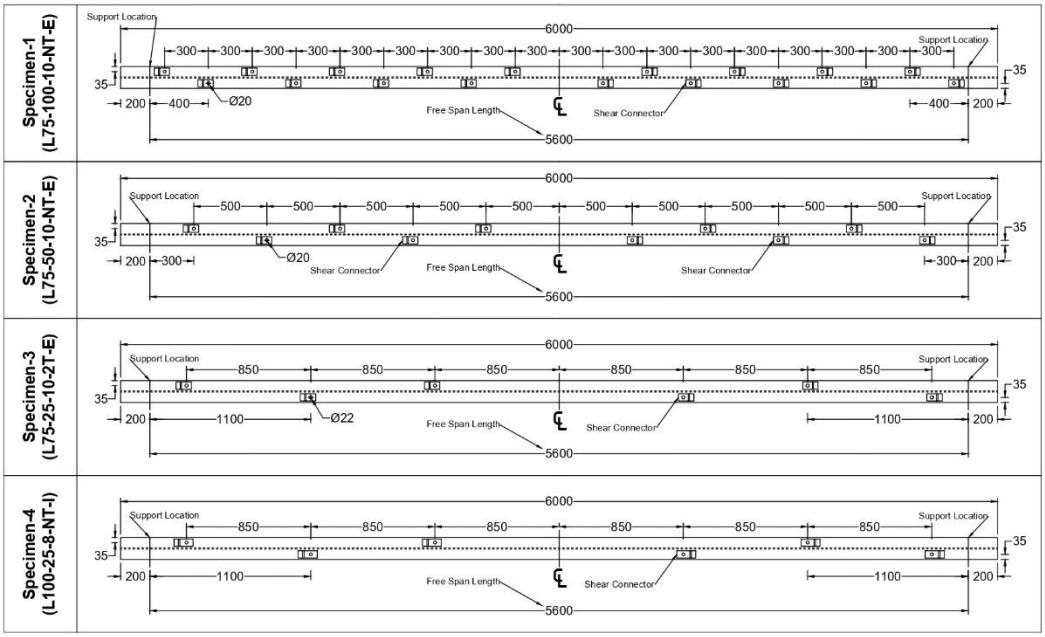

Figure 4.6: Technical drawings of specimens

4.3 Test Results

A total of four beam specimens, explained in Table 4.1, were tested under single-point loading. The conducted experiments had two main phases. In the first phase, specimens were cyclically loaded, consisting of four cycles to specified limits, i.e., 25 kN, 50 kN, and 75 kN, in the elastic range. In other words, 25 kN, 50 kN, and 75 kN loads were chosen as the elastic load limits, and specimens were loaded and unloaded four times to each limit. In the second phase, specimens were loaded to failure.

While conducting the experiments on specimen 2, twist of the concrete deck was observed, as shown in Figure 4.7. To prevent the differential deflection, the rotation prevention system, shown in Figure 4.2b, was developed, and experiments were conducted using that system. Therefore, the main loading of specimen 2 was completed in more than one stage, similar to cyclic loading.

Figure 4.7: Twist of concrete deck

4.3.1 Elastic Loading Tests

An applied load of 25 kN was chosen as the target load (TL) in this phase of experiments. Thus, 25, 50, and 75 kN loads were labeled as 1TL, 2TL, and 3TL, respectively. The main reason behind the undertaken loads was to ensure that the steel beam stayed in between the elastic region. The loads were applied slowly enough to prevent any sudden failure. Elastic loading tests were conducted to understand the behavior of the specimens under service load.

4.3.1.1 Load-Deflection Behaviors

The midspan deflection of the specimens under applied target loads is given in Figure 4.8, Figure 4.9, Figure 4.10, and Figure 4.11, respectively.

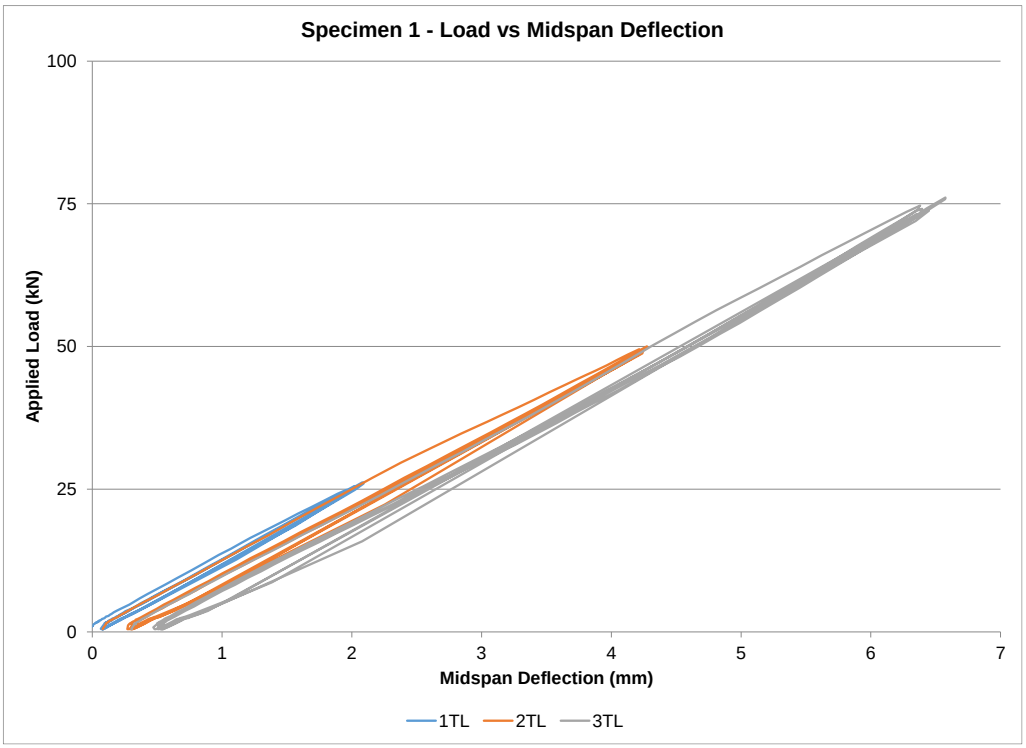

Figure 4.8: Specimen 1 - L75-100-10-NT-E - applied load vs. midspan deflection

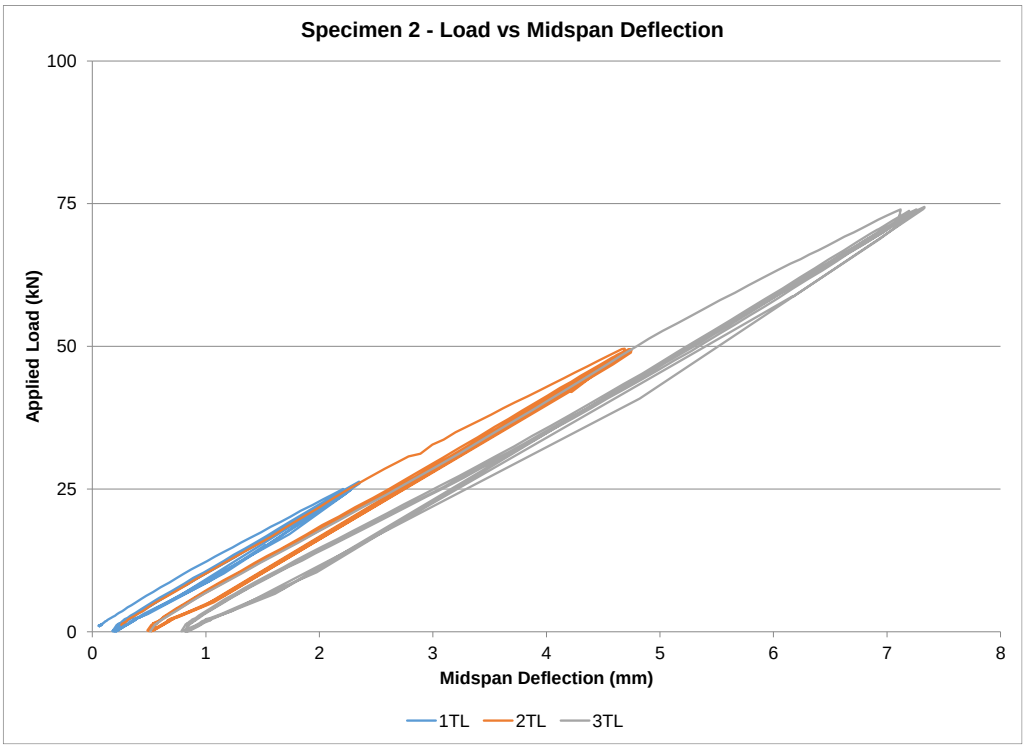

Figure 4.9: Specimen 2 - L75-50-10-NT-E - applied load vs. midspan deflection

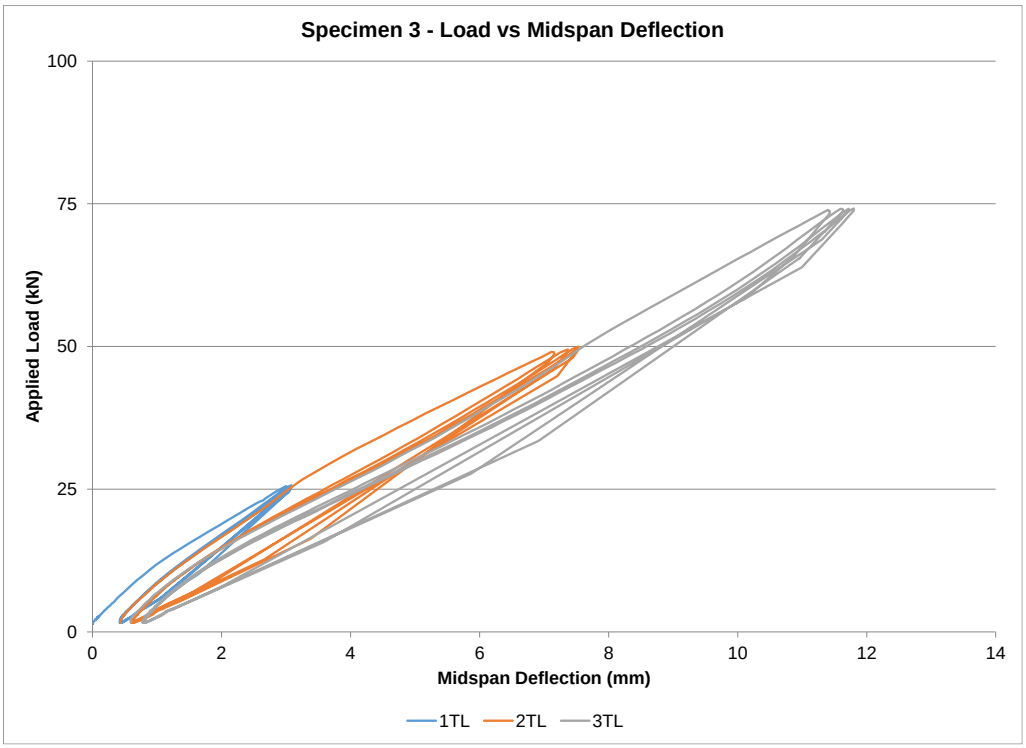

Figure 4.10: Specimen 3 - L75-25-10-2T-E - applied load vs. midspan deflection

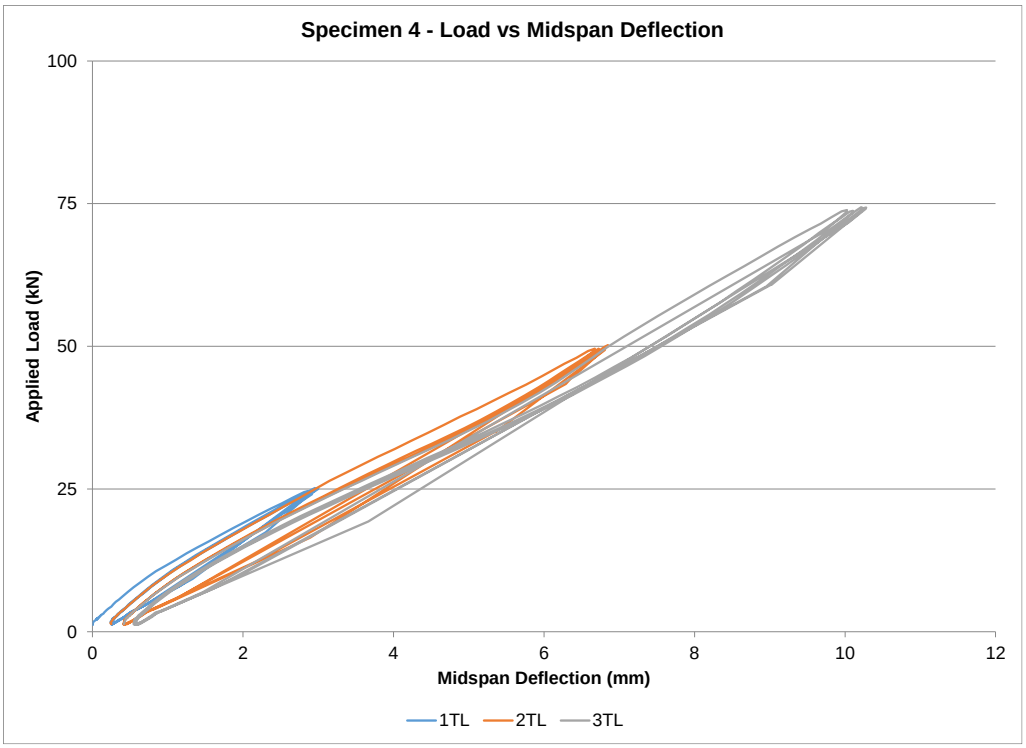

Figure 4.11: Specimen 4 - L100-25-8-NT-I - applied load vs. midspan deflection

The specimens showed similar load-deflection behavior. According to the results, it can be seen that the midspan deflection of composite beams decreases with the increase of the degree of composite action. In other words, the stiffness against deflection in elastic loadings increased with the increase of the composite ratio. Additionally, the inclusion of hole tolerance decreased the stiffness, which resulted in higher midspan deflections. To overcome the lower stiffness against deflection caused by the inclusion of hole tolerance, bolts of the connectors may be tightened with a higher torque.

The maximum and residual deflections observed at the midspan of each specimen are given in Table 4.6, Table 4.7, Table 4.8, and Table 4.9, respectively. It can be seen that the increase in load caused an increase in the residual deflections. Specimen 4, which has L100 connectors cut to have a height of 75 mm, showed fewer residual deflections compared to specimen 2, which has a higher composite degree but L75 connectors. The reason could be the higher rigidity of the L100 connector caused by its thickness.

Table 4.6: Specimen 1 maximum and residual midspan deflections

Specimen 1 - L75-100-10-NT-E	Loadings & Details		
	1TL	2TL	3TL
Load (kN)	**25**	**50**	**75**
Midspan Deflection at Maximum Load (mm)	2.09	4.20	6.19
Residual Midspan Deflection (mm)	0.08	0.31	0.53
Cumulative Residual Midspan Deflection (mm)	0.00	0.08	0.39
Cumulative Maximum Midspan Deflection (mm)	2.09	4.28	6.58

Table 4.7: Specimen 2 maximum and residual midspan deflections

Specimen 2 - L75-50-10-NT-E	Loadings & Details		
	1TL	2TL	3TL
Load (kN)	**25**	**50**	**75**
Midspan Deflection at Maximum Load (mm)	2.36	4.50	6.56
Residual Midspan Deflection (mm)	0.26	0.52	0.83
Cumulative Residual Midspan Deflection (mm)	0.00	0.26	0.77
Cumulative Maximum Midspan Deflection (mm)	2.36	4.75	7.33

Table 4.8: Specimen 3 maximum and residual midspan deflections

Specimen 3 - L75-25-10-2T-E	Loadings & Details		
	1TL	2TL	3TL
Load (kN)	**25**	**50**	**75**
Midspan Deflection at Maximum Load (mm)	3.08	7.10	10.78
Residual Midspan Deflection (mm)	0.44	0.59	0.80
Cumulative Residual Midspan Deflection (mm)	0.00	0.44	1.03
Cumulative Maximum Midspan Deflection (mm)	3.08	7.53	11.80

Table 4.9: Specimen 4 maximum and residual midspan deflections

Specimen 4 - L100-25-8-NT-I	Loadings & Details		
	1TL	2TL	3TL
Load (kN)	**25**	**50**	**75**
Midspan Deflection at Maximum Load (mm)	3.00	6.60	9.62
Residual Midspan Deflection (mm)	0.25	0.42	0.58
Cumulative Residual Midspan Deflection (mm)	0.00	0.25	0.67
Cumulative Maximum Midspan Deflection (mm)	3.00	6.85	10.28

4.3.1.2 Load-Slip Behaviors

The end slips of the specimens under applied target loads are given in Figure 4.12, Figure 4.13, Figure 4.14, and Figure 4.15, respectively.

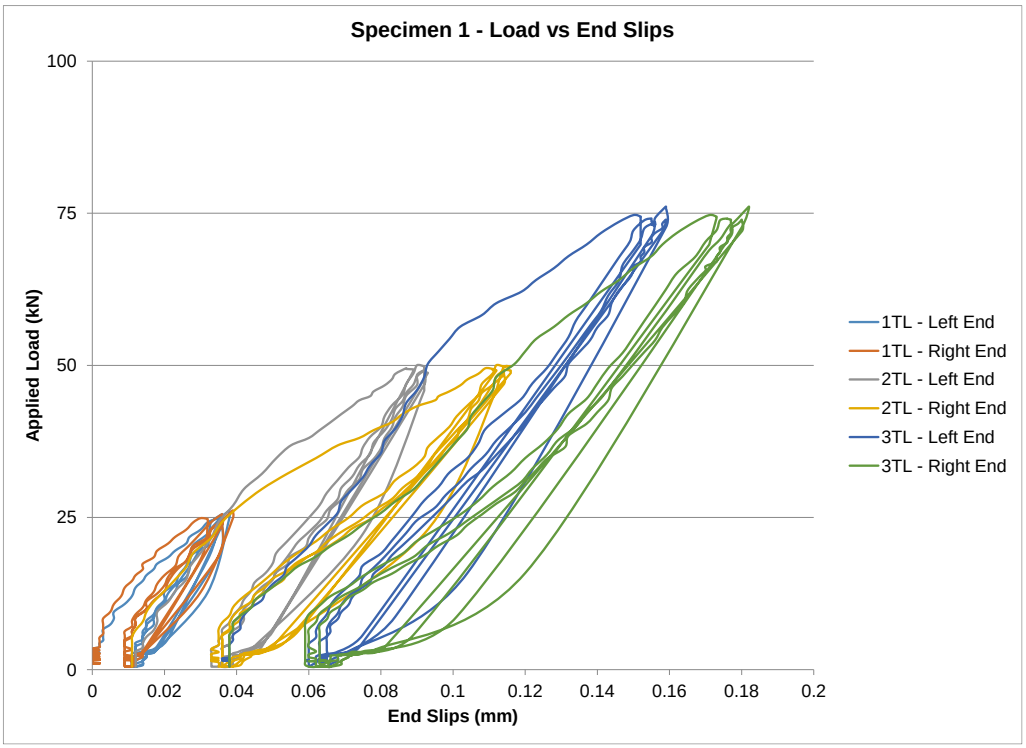

Figure 4.12: Specimen 1 - L75-100-10-NT-E - applied load vs. end slips

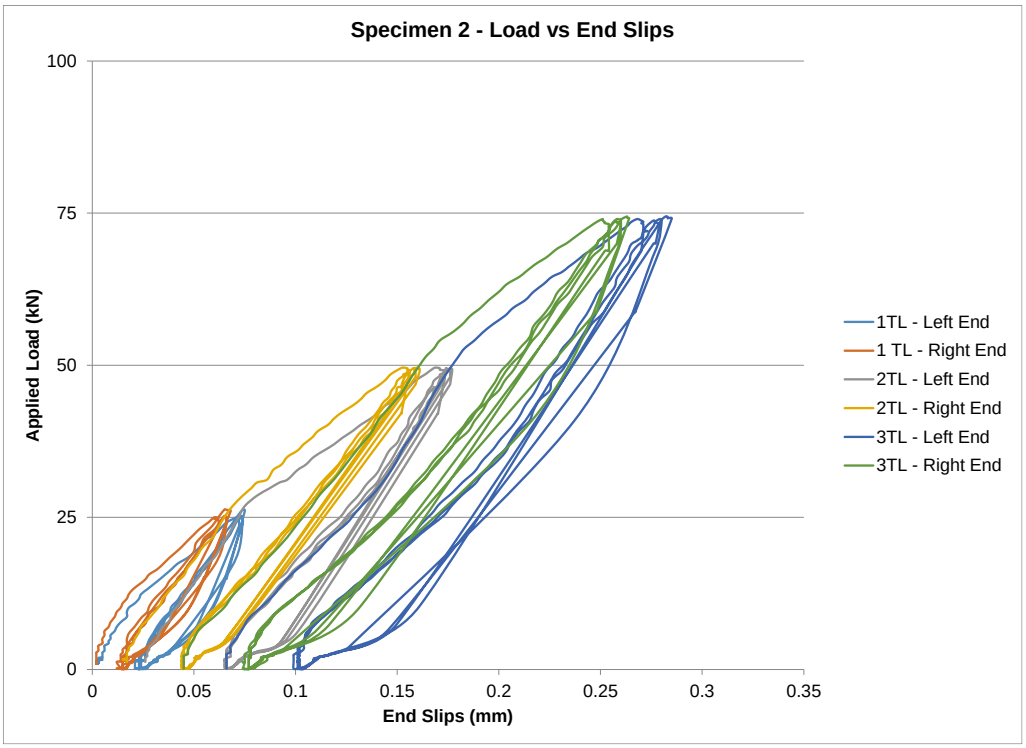

Figure 4.13: Specimen 2 - L75-50-10-NT-E - applied load vs. end slips

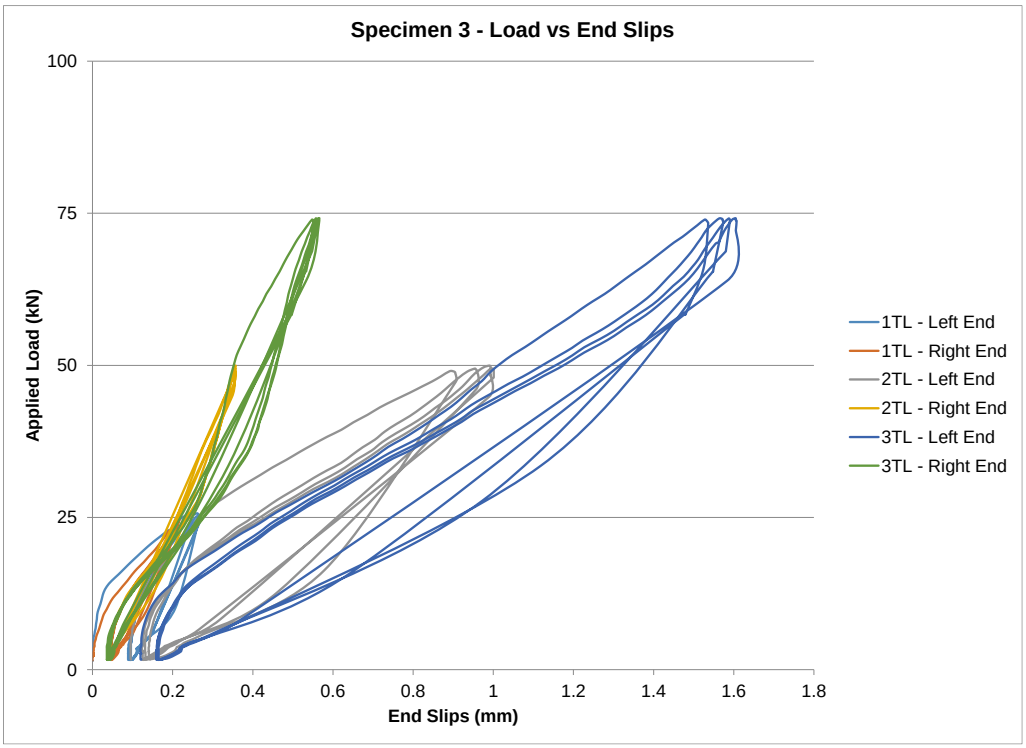

Figure 4.14: Specimen 3 - L75-25-10-2T-E - applied load vs. end slips

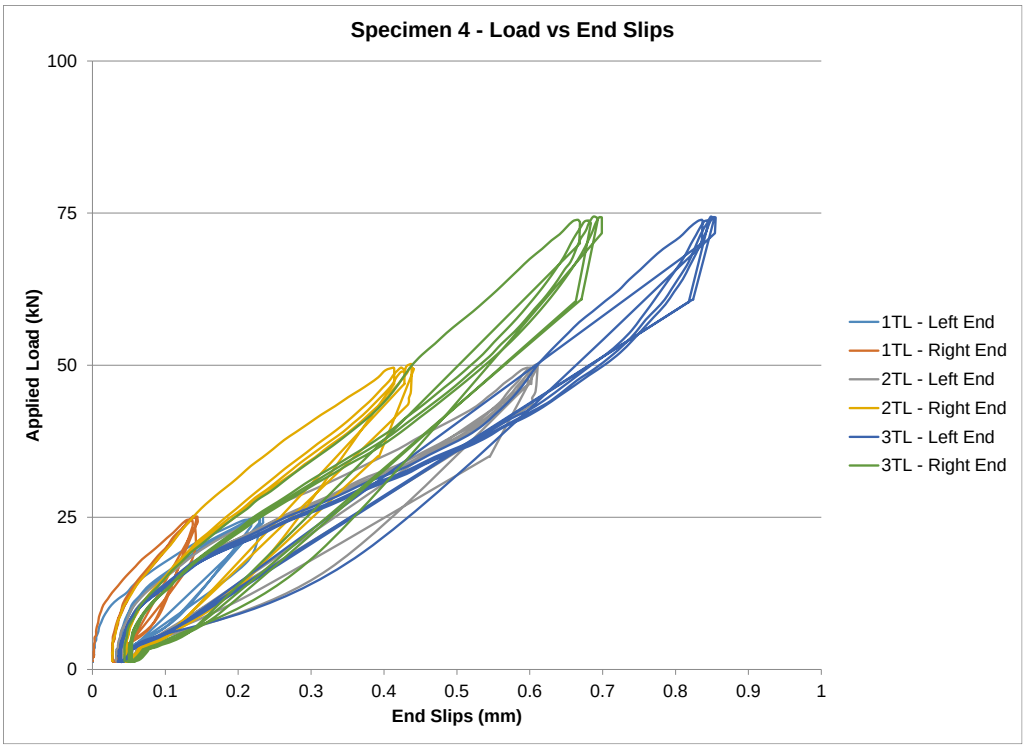

Figure 4.15: Specimen 4 - L100-25-8-NT-I - applied load vs. end slips

The specimens, except specimen 3, showed similar load-slip behavior. According to the results, it can be seen that the end slips of composite beams decrease with the increase of the degree of composite action. In other words, the stiffness against slip in elastic loadings increased with the increase of composite ratio. The differences between the slip of ends decreased with the increase in load, and under 3TL load, the differences were lower than 20%, which is acceptable. On the other hand, specimen 3 showed the highest end slips and slip difference between ends because of the hole tolerance. However, it was indicated by the results that the degree of end slips was low and within acceptable limits, according to Eurocode 4 (2011).

The maximum and residual slips observed at the ends of each specimen are given in Table 4.10, Table 4.11, Table 4.12, and Table 4.13, respectively. It can be seen that the increase in load caused an increase in the residual slips, and an increase in composite degree decreased the residual slips. In addition, the hole tolerance of specimen 3 caused higher residual slips compared to the others.

Table 4.10: Specimen 1 maximum and residual end slips

Specimen 1 - L75-100-10-NT-E	Loadings & Details		
	1TL	2TL	3TL
Load (kN)	25	50	75
Left End (LVDT4) Slip at Each Loading Cycle (mm)	0.04	0.08	0.11
Left End (LVDT4) Residual slip (mm)	0.01	0.04	0.07
Left End (LVDT4) Cumulative Residual Slip (mm)	0.00	0.01	0.05
Left End (LVDT4) Cumulative slip (mm)	0.04	0.09	0.16
Right End (LVDT3) Slip at Each Loading Cycle (mm)	0.04	0.11	0.13
Right End (LVDT3) Residual slip (mm)	0.01	0.04	0.07
Right End (LVDT3) Cumulative Residual Slip (mm)	0.00	0.01	0.05
Right End (LVDT3) Cumulative slip (mm)	0.04	0.12	0.18

Table 4.11: Specimen 2 maximum and residual end slips

Specimen 2 - L75-50-10-NT-E	Loadings & Details		
	1TL	2TL	3TL
Load (kN)	**25**	**50**	**75**
Left End (LVDT4) Slip at Each Loading Cycle (mm)	0.08	0.15	0.19
Left End (LVDT4) Residual slip (mm)	0.03	0.07	0.10
Left End (LVDT4) Cumulative Residual Slip (mm)	0.00	0.03	0.09
Left End (LVDT4) Cumulative slip (mm)	0.08	0.18	0.29
Right End (LVDT3) Slip at Each Loading Cycle (mm)	0.07	0.14	0.20
Right End (LVDT3) Residual slip (mm)	0.02	0.05	0.08
Right End (LVDT3) Cumulative Residual Slip (mm)	0.00	0.02	0.06
Right End (LVDT3) Cumulative slip (mm)	0.07	0.16	0.26

Table 4.12: Specimen 3 maximum and residual end slips

Specimen 3 - L75-25-10-2T-E	Loadings & Details		
	1TL	2TL	3TL
Load (kN)	**25**	**50**	**75**
Left End (LVDT4) Slip at Each Loading Cycle (mm)	0.27	0.91	1.39
Left End (LVDT4) Residual slip (mm)	0.10	0.12	0.16
Left End (LVDT4) Cumulative Residual Slip (mm)	0.00	0.10	0.22
Left End (LVDT4) Cumulative slip (mm)	0.27	1.00	1.61
Right End (LVDT3) Slip at Each Loading Cycle (mm)	0.22	0.32	0.49
Right End (LVDT3) Residual slip (mm)	0.04	0.04	0.04
Right End (LVDT3) Cumulative Residual Slip (mm)	0.00	0.04	0.08
Right End (LVDT3) Cumulative slip (mm)	0.22	0.36	0.57

Table 4.13: Specimen 4 maximum and residual end slips

Specimen 4 - L100-25-8-NT-I	Loadings & Details		
	1TL	2TL	3TL
Load (kN)	**25**	**50**	**75**
Left End (LVDT4) Slip at Each Loading Cycle (mm)	0.23	0.58	0.78
Left End (LVDT4) Residual slip (mm)	0.03	0.04	0.04
Left End (LVDT4) Cumulative Residual Slip (mm)	0.00	0.03	0.07
Left End (LVDT4) Cumulative slip (mm)	0.23	0.61	0.86
Right End (LVDT3) Slip at Each Loading Cycle (mm)	0.14	0.41	0.63
Right End (LVDT3) Residual slip (mm)	0.03	0.04	0.05
Right End (LVDT3) Cumulative Residual Slip (mm)	0.00	0.03	0.07
Right End (LVDT3) Cumulative slip (mm)	0.14	0.44	0.70

There were four slip recordings in both halves of the specimens, as shown in Figure 4.3. The maximum and residual slips observed at each half of the specimens are given in Table 4.14, Table 4.15, Table 4.16, Table 4.17, Table 4.18, Table 4.19, Table 4.20, and Table 4.21 for the left and the right ends of specimens 1 to 4, respectively.

The slip behavior of ends was similar to each other. According to the results, it can be seen that from the ends to the middle of the specimen, maximum and residual slip decreased since the slipping free span length decreased.

Table 4.14: Specimen 1 left half maximum and residual slips

Specimen 1 - L75-100-10-NT-E	Loadings & Details		
	1TL	2TL	3TL
Load (kN)	25	50	75
LVDT5 (Slip 2) Slip at Each Loading Cycle (mm)	0.04	0.09	0.13
LVDT5 (Slip 2) Residual slip (mm)	0.01	0.03	0.05
LVDT5 (Slip 2) Cumulative Residual Slip (mm)	0.00	0.01	0.04
LVDT5 (Slip 2) Cumulative slip (mm)	0.04	0.10	0.17
LVDT6 (Slip 3) Slip at Each Loading Cycle (mm)	0.03	0.09	0.13
LVDT6 (Slip 3) Residual slip (mm)	0.01	0.03	0.06
LVDT6 (Slip 3) Cumulative Residual Slip (mm)	0.00	0.01	0.04
LVDT6 (Slip 3) Cumulative slip (mm)	0.03	0.10	0.17
LVDT7 (Slip 4) Slip at Each Loading Cycle (mm)	0.02	0.06	0.09
LVDT7 (Slip 4) Residual slip (mm)	0.01	0.02	0.03
LVDT7 (Slip 4) Cumulative Residual Slip (mm)	0.00	0.01	0.03
LVDT7 (Slip 4) Cumulative slip (mm)	0.02	0.07	0.12
Where from left end to the middle, LVDT order is: 5 -> 6 -> 7			

Table 4.15: Specimen 1 right half maximum and residual slips

Specimen 1 - L75-100-10-NT-E	Loadings & Details		
	1TL	2TL	3TL
Load (kN)	25	50	75
LVDT10 (Slip 2) Slip at Each Loading Cycle (mm)	0.04	0.11	0.13
LVDT10 (Slip 2) Residual slip (mm)	0.01	0.04	0.07
LVDT10 (Slip 2) Cumulative Residual Slip (mm)	0.00	0.01	0.05
LVDT10 (Slip 2) Cumulative slip (mm)	0.04	0.12	0.18
LVDT9 (Slip 3) Slip at Each Loading Cycle (mm)	0.04	0.09	0.11
LVDT9 (Slip 3) Residual slip (mm)	0.02	0.05	0.07
LVDT9 (Slip 3) Cumulative Residual Slip (mm)	0.00	0.02	0.06
LVDT9 (Slip 3) Cumulative slip (mm)	0.04	0.11	0.17
LVDT8 (Slip 4) Slip at Each Loading Cycle (mm)	0.03	0.07	0.09
LVDT8 (Slip 4) Residual slip (mm)	0.01	0.03	0.05
LVDT8 (Slip 4) Cumulative Residual Slip (mm)	0.00	0.01	0.04
LVDT8 (Slip 4) Cumulative slip (mm)	0.03	0.08	0.13
Where from right end to the middle, LVDT order is: 10 -> 9 -> 8			

Table 4.16: Specimen 2 left half maximum and residual slips

Specimen 2 - L75-50-10-NT-E	Loadings & Details		
	1TL	2TL	3TL
Load (kN)	25	50	75
LVDT5 (Slip 2) Slip at Each Loading Cycle (mm)	0.07	0.15	0.20
LVDT5 (Slip 2) Residual slip (mm)	0.03	0.06	0.10
LVDT5 (Slip 2) Cumulative Residual Slip (mm)	0.00	0.03	0.09
LVDT5 (Slip 2) Cumulative slip (mm)	0.07	0.18	0.29
LVDT6 (Slip 3) Slip at Each Loading Cycle (mm)	0.08	0.17	0.22
LVDT6 (Slip 3) Residual slip (mm)	0.02	0.04	0.05
LVDT6 (Slip 3) Cumulative Residual Slip (mm)	0.00	0.02	0.07
LVDT6 (Slip 3) Cumulative slip (mm)	0.08	0.19	0.29
LVDT7 (Slip 4) Slip at Each Loading Cycle (mm)	0.07	0.14	0.20
LVDT7 (Slip 4) Residual slip (mm)	0.02	0.05	0.08
LVDT7 (Slip 4) Cumulative Residual Slip (mm)	0.00	0.02	0.06
LVDT7 (Slip 4) Cumulative slip (mm)	0.07	0.16	0.26
Where from left end to the middle, LVDT order is: 5 -> 6 -> 7			

Table 4.17: Specimen 2 right half maximum and residual slips

Specimen 2 - L75-50-10-NT-E	Loadings & Details		
	1TL	2TL	3TL
Load (kN)	**25**	**50**	**75**
LVDT10 (Slip 2) Slip at Each Loading Cycle (mm)	0.07	0.15	0.22
LVDT10 (Slip 2) Residual slip (mm)	0.02	0.05	0.09
LVDT10 (Slip 2) Cumulative Residual Slip (mm)	0.00	0.02	0.07
LVDT10 (Slip 2) Cumulative slip (mm)	0.07	0.17	0.29
LVDT9 (Slip 3) Slip at Each Loading Cycle (mm)	0.05	0.12	0.18
LVDT9 (Slip 3) Residual slip (mm)	0.02	0.04	0.07
LVDT9 (Slip 3) Cumulative Residual Slip (mm)	0.00	0.02	0.06
LVDT9 (Slip 3) Cumulative slip (mm)	0.05	0.14	0.24
LVDT8 (Slip 4) Slip at Each Loading Cycle (mm)	0.04	0.10	0.16
LVDT8 (Slip 4) Residual slip (mm)	0.01	0.03	0.05
LVDT8 (Slip 4) Cumulative Residual Slip (mm)	0.00	0.01	0.03
LVDT8 (Slip 4) Cumulative slip (mm)	0.04	0.11	0.19
Where from right end to the middle, LVDT order is: 10 -> 9 -> 8			

Table 4.18: Specimen 3 left half maximum and residual slips

Specimen 3 - L75-25-10-2T-E	Loadings & Details		
	1TL	2TL	3TL
Load (kN)	**25**	**50**	**75**
LVDT5 (Slip 2) Slip at Each Loading Cycle (mm)	0.25	0.87	1.28
LVDT5 (Slip 2) Residual slip (mm)	0.10	0.14	0.17
LVDT5 (Slip 2) Cumulative Residual Slip (mm)	0.00	0.10	0.23
LVDT5 (Slip 2) Cumulative slip (mm)	0.25	0.97	1.51
LVDT6 (Slip 3) Slip at Each Loading Cycle (mm)	0.22	0.80	1.22
LVDT6 (Slip 3) Residual slip (mm)	0.08	0.11	0.16
LVDT6 (Slip 3) Cumulative Residual Slip (mm)	0.00	0.08	0.19
LVDT6 (Slip 3) Cumulative slip (mm)	0.22	0.88	1.41
LVDT7 (Slip 4) Slip at Each Loading Cycle (mm)	0.15	0.61	0.95
LVDT7 (Slip 4) Residual slip (mm)	0.05	0.09	0.13
LVDT7 (Slip 4) Cumulative Residual Slip (mm)	0.00	0.05	0.14
LVDT7 (Slip 4) Cumulative slip (mm)	0.15	0.66	1.09
Where from left end to the middle, LVDT order is: 5 -> 6 -> 7			

Table 4.19: Specimen 3 right half maximum and residual slips

Specimen 3 - L75-25-10-2T-E	Loadings & Details		
	1TL	2TL	3TL
Load (kN)	25	50	75
LVDT10 (Slip 2) Slip at Each Loading Cycle (mm)	0.21	0.34	0.55
LVDT10 (Slip 2) Residual slip (mm)	0.03	0.03	0.03
LVDT10 (Slip 2) Cumulative Residual Slip (mm)	0.00	0.03	0.06
LVDT10 (Slip 2) Cumulative slip (mm)	0.21	0.37	0.61
LVDT9 (Slip 3) Slip at Each Loading Cycle (mm)	0.17	0.25	0.42
LVDT9 (Slip 3) Residual slip (mm)	0.03	0.02	0.03
LVDT9 (Slip 3) Cumulative Residual Slip (mm)	0.00	0.03	0.05
LVDT9 (Slip 3) Cumulative slip (mm)	0.17	0.28	0.47
LVDT8 (Slip 4) Slip at Each Loading Cycle (mm)	0.09	0.08	0.11
LVDT8 (Slip 4) Residual slip (mm)	0.01	0.00	0.00
LVDT8 (Slip 4) Cumulative Residual Slip (mm)	0.00	0.01	0.01
LVDT8 (Slip 4) Cumulative slip (mm)	0.09	0.09	0.11
Where from right end to the middle, LVDT order is: 10 -> 9 -> 8			

Table 4.20: Specimen 4 left half maximum and residual slips

Specimen 4 - L100-25-8-NT-I	Loadings & Details		
	1TL	2TL	3TL
Load (kN)	25	50	75
LVDT5 (Slip 2) Slip at Each Loading Cycle (mm)	0.21	0.51	0.69
LVDT5 (Slip 2) Residual slip (mm)	0.04	0.04	0.04
LVDT5 (Slip 2) Cumulative Residual Slip (mm)	0.00	0.04	0.08
LVDT5 (Slip 2) Cumulative slip (mm)	0.21	0.55	0.77
LVDT6 (Slip 3) Slip at Each Loading Cycle (mm)	0.18	0.45	0.62
LVDT6 (Slip 3) Residual slip (mm)	0.03	0.04	0.04
LVDT6 (Slip 3) Cumulative Residual Slip (mm)	0.00	0.03	0.06
LVDT6 (Slip 3) Cumulative slip (mm)	0.18	0.48	0.68
LVDT7 (Slip 4) Slip at Each Loading Cycle (mm)	0.13	0.29	0.40
LVDT7 (Slip 4) Residual slip (mm)	0.03	0.04	0.05
LVDT7 (Slip 4) Cumulative Residual Slip (mm)	0.00	0.03	0.06
LVDT7 (Slip 4) Cumulative slip (mm)	0.13	0.32	0.46
Where from left end to the middle, LVDT order is: 5 -> 6 -> 7			

Table 4.21: Specimen 4 right half maximum and residual slips

Specimen 4 - L100-25-8-NT-I	Loadings & Details		
	1TL	2TL	3TL
Load (kN)	25	50	75
LVDT10 (Slip 2) Slip at Each Loading Cycle (mm)	0.18	0.47	0.73
LVDT10 (Slip 2) Residual slip (mm)	0.02	0.04	0.05
LVDT10 (Slip 2) Cumulative Residual Slip (mm)	0.00	0.02	0.06
LVDT10 (Slip 2) Cumulative slip (mm)	0.18	0.49	0.79
LVDT9 (Slip 3) Slip at Each Loading Cycle (mm)	0.14	0.36	0.55
LVDT9 (Slip 3) Residual slip (mm)	0.03	0.05	0.07
LVDT9 (Slip 3) Cumulative Residual Slip (mm)	0.00	0.03	0.08
LVDT9 (Slip 3) Cumulative slip (mm)	0.14	0.39	0.63
LVDT8 (Slip 4) Slip at Each Loading Cycle (mm)	0.07	0.18	0.31
LVDT8 (Slip 4) Residual slip (mm)	0.01	0.03	0.05
LVDT8 (Slip 4) Cumulative Residual Slip (mm)	0.00	0.01	0.04
LVDT8 (Slip 4) Cumulative slip (mm)	0.07	0.19	0.35
Where from right end to the middle, LVDT order is: 10 -> 9 -> 8			

4.3.1.3 Strain Distributions

Strain values were monitored during the loadings using the strain gauges shown in Figure 4.3. The monitored strain distributions at the midspan of the steel section against each loading cycle are given in Table 4.22, Table 4.23, Table 4.24, and Table 4.25 for specimens 1 to 4, respectively.

Table 4.22: Specimen 1 strain distributions

Specimen 1 - L75-100-10-NT-E	Loadings & Details		
	1TL	2TL	3TL
Load (kN)	25	50	75
Strain in steel beam top flange (με)	-22.51	-67.02	-106.53
Strain in steel upper part of web (με)	38.98	58.47	58.47
Strain in steel middle of web (με)	85.22	155.84	228.98
Strain in steel lower part of web (με)	135.52	270.57	401.64
Strain in steel beam bottom flange (με)	184.79	381.16	572.10

Table 4.23: Specimen 2 strain distributions

Specimen 2 - L75-50-10-NT-E	Loadings & Details		
	1TL	2TL	3TL
Load (kN)	25	50	75
Strain in steel beam top flange (με)	-44.87	-114.93	-185.50
Strain in steel upper part of web (με)	12.90	46.16	41.20
Strain in steel middle of web (με)	72.48	132.89	199.35
Strain in steel lower part of web (με)	131.78	261.57	412.54
Strain in steel beam bottom flange (με)	193.78	398.72	584.60

Table 4.24: Specimen 3 strain distributions

Specimen 3 - L75-25-10-2T-E	Loadings & Details		
	1TL	2TL	3TL
Load (kN)	25	50	75
Strain in steel beam top flange (με)	-116.94	-368.79	-584.43
Strain in steel upper part of web (με)	-36.09	-143.35	-230.04
Strain in steel middle of web (με)	39.38	57.05	90.37
Strain in steel lower part of web (με)	122.55	258.19	406.43
Strain in steel beam bottom flange (με)	209.60	485.19	-

Table 4.25: Specimen 4 strain distributions

Specimen 4 - L100-25-8-NT-I	Loadings & Details		
	1TL	2TL	3TL
Load (kN)	25	50	75
Strain in steel beam top flange (με)	-110.36	-295.90	-461.33
Strain in steel upper part of web (με)	-30.68	-100.09	-155.91
Strain in steel middle of web (με)	44.35	77.61	119.45
Strain in steel lower part of web (με)	125.17	264.46	413.85
Strain in steel beam bottom flange (με)	209.71	469.84	720.53

According to the coupon test results given in Table 4.4, the yield strength of the steel beam was taken as 293.20 MPa, which is the yield strength of flanges, since the strain distribution of the bottom flange was the highest. In addition, the elastic modulus of the steel section was taken as 200 GPa. As a result, the yield strain value of the steel section was determined as 1466 με. Comparing recorded strain values with yield

strain value proved that the steel section did not yield during the loadings and the tests were in the elastic region.

To locate the neutral axis (NA) of specimens in each loading, strain distributions with their trendlines were drawn and given in Figure 4.16, Figure 4.17, Figure 4.18, Figure 4.19, Figure 4.20, Figure 4.21, Figure 4.22, Figure 4.23, Figure 4.24, Figure 4.25, Figure 4.26, and Figure 4.27 for loadings 1TL to 3TL and specimens 1 to 4 and, respectively.

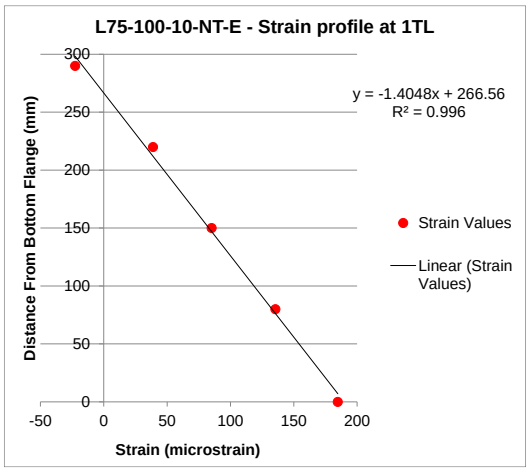

Figure 4.16: Specimen 1 strain distribution at 1TL

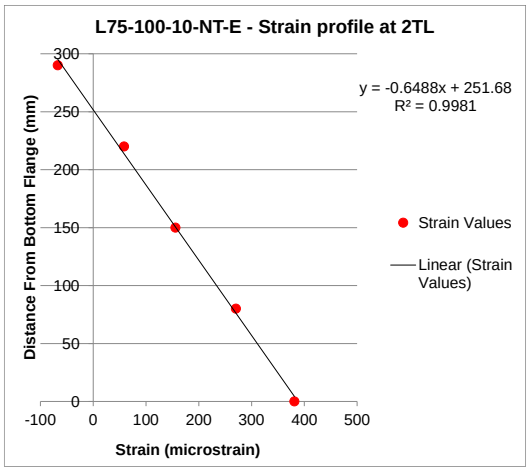

Figure 4.17: Specimen 1 strain distribution at 2TL

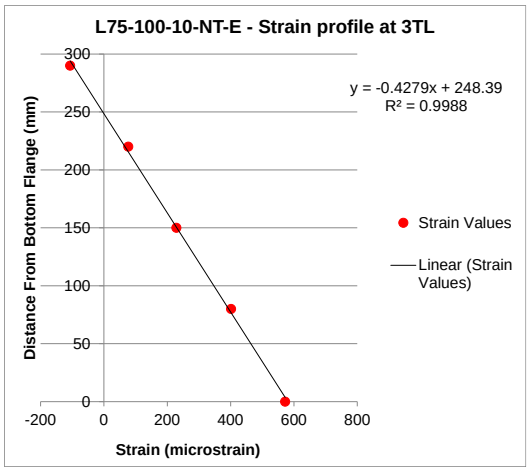

Figure 4.18: Specimen 1 strain distribution at 3TL

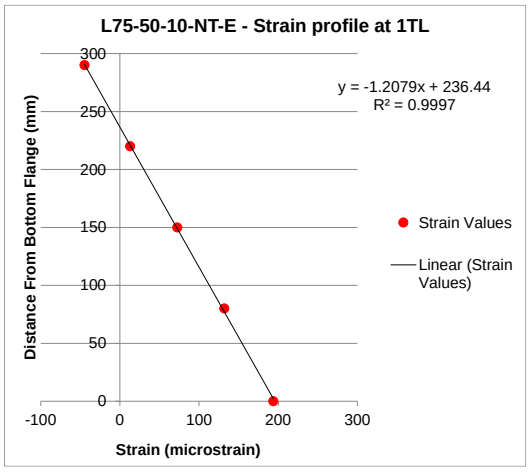

Figure 4.19: Specimen 2 strain distribution at 1TL

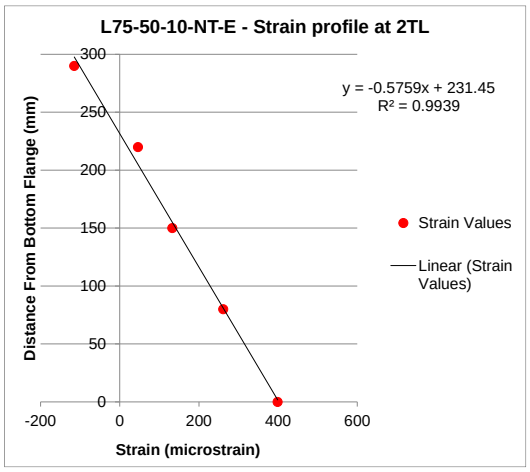

Figure 4.20: Specimen 2 strain distribution at 2TL

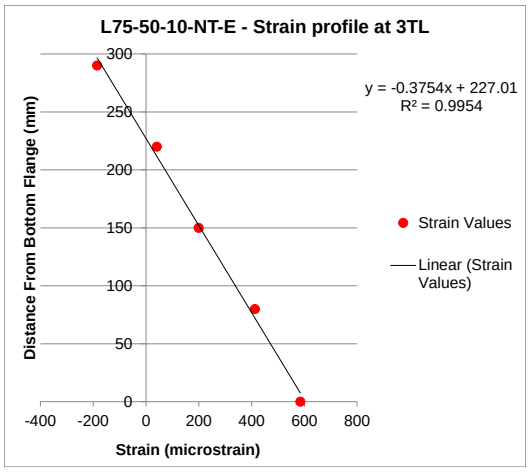

Figure 4.21: Specimen 2 strain distribution at 3TL

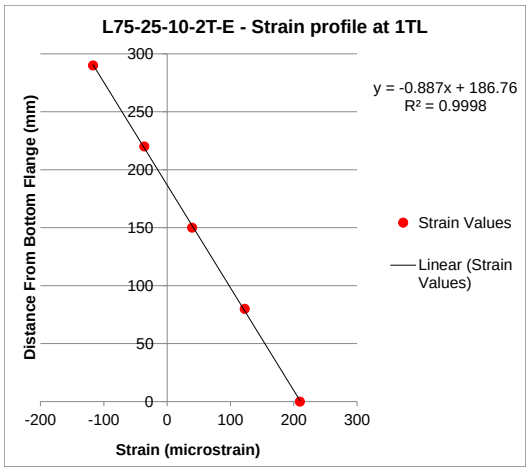

Figure 4.22: Specimen 3 strain distribution at 1TL

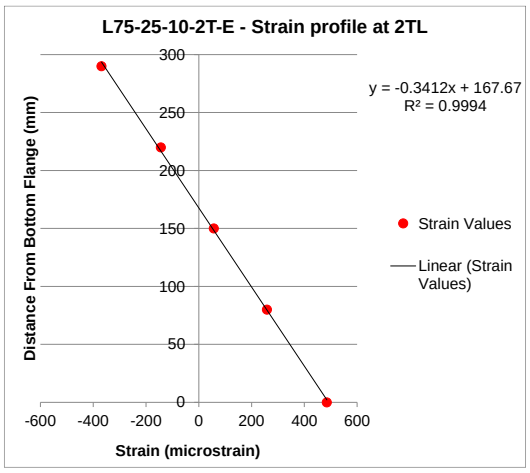

Figure 4.23: Specimen 3 strain distribution at 2TL

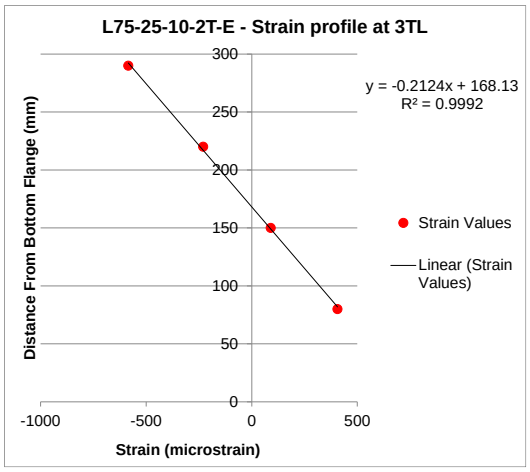

Figure 4.24: Specimen 3 strain distribution at 3TL

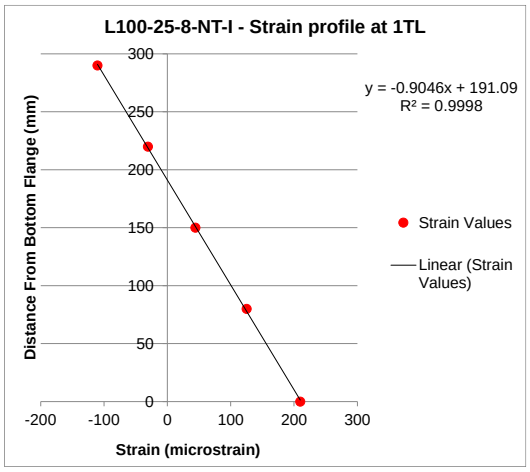

Figure 4.25: Specimen 4 strain distribution at 1TL

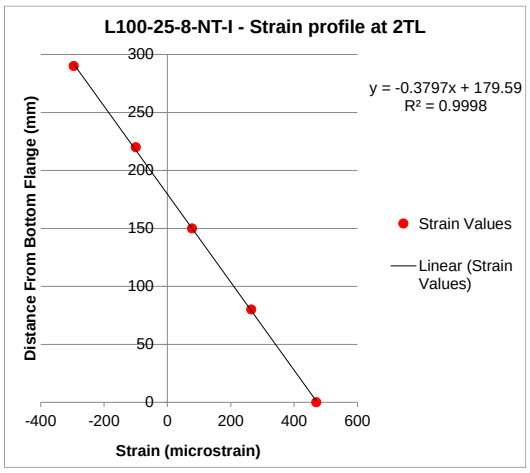

Figure 4.26: Specimen 4 strain distribution at 2TL

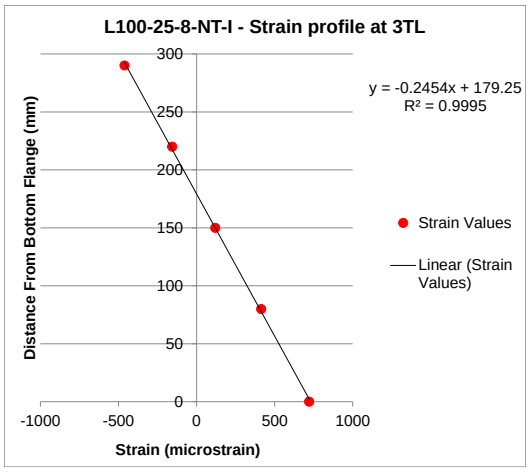

Figure 4.27: Specimen 4 strain distribution at 3TL

According to the trendlines drawn, neutral axis locations are determined and given in Table 4.26.

Table 4.26: NA (Neutral Axis) locations measured from the bottom flange

Specimen # & Nomenclature	NA Locations from bottom		
	1TL	2TL	3TL
Specimen 1 - L75-100-10-NT-E	266.56	251.68	248.39
Specimen 2 - L75-50-10-NT-E	236.44	231.45	227.01
Specimen 3 - L75-25-10-2T-E	186.76	167.67	168.13
Specimen 4 - L100-25-8-NT-I	191.09	179.59	179.25

The strain values showed that with the increase of the degree of composite action, strain distribution through the steel beam decreased since the contribution of the concrete to the capacity increases. In other words, the increase of composite degree resulted in shifting the neutral axis upwards with the higher contribution of concrete. The position of the neutral axis was observed to change with the increase in the applied load. This is attributable to the micro-cracking of the concrete deck and the slip that takes between the steel section and the concrete deck.

4.3.2 Ultimate Loading Tests

In the second phase of the experiments, previously cyclic loaded specimens were loaded to their ultimate capacity, which varies between 8.5 and 11.5 TL.

4.3.2.1 Load-Deflection Behaviors

The midspan deflection of specimens is given in Figure 4.28, Figure 4.29, Figure 4.30, and Figure 4.31, respectively.

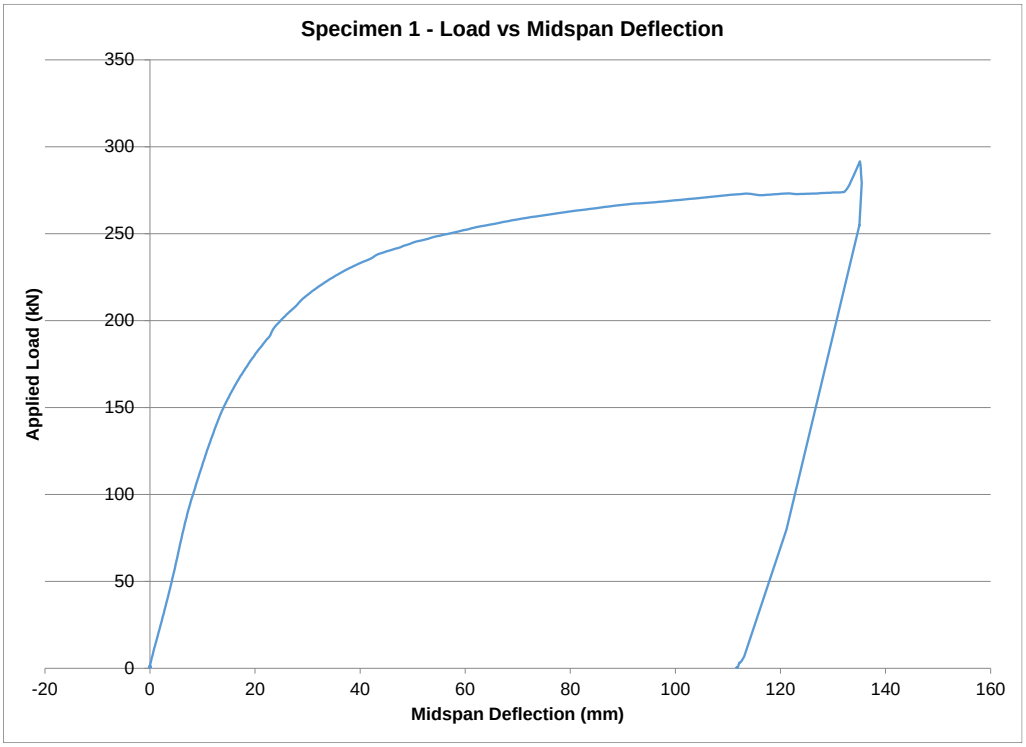

Figure 4.28: Specimen 1 - L75-100-10-NT-E - applied load vs. midspan deflection

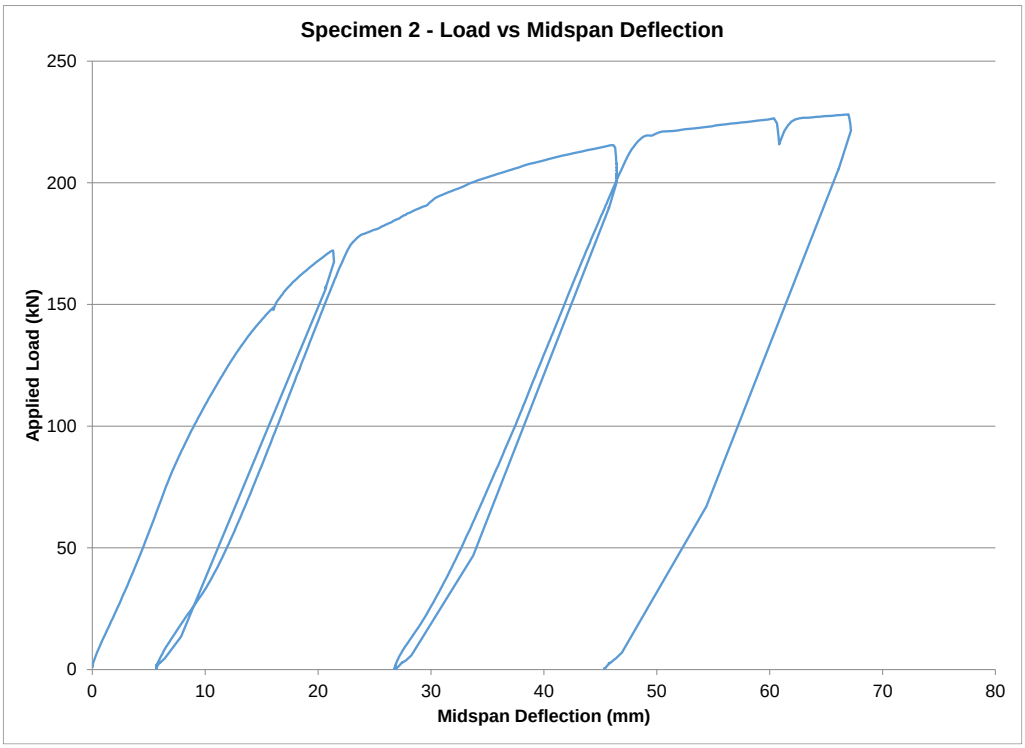

Figure 4.29: Specimen 2 - L75-50-10-NT-E - applied load vs. midspan deflection

Figure 4.30: Specimen 3 - L75-25-10-2T-E - applied load vs. midspan deflection

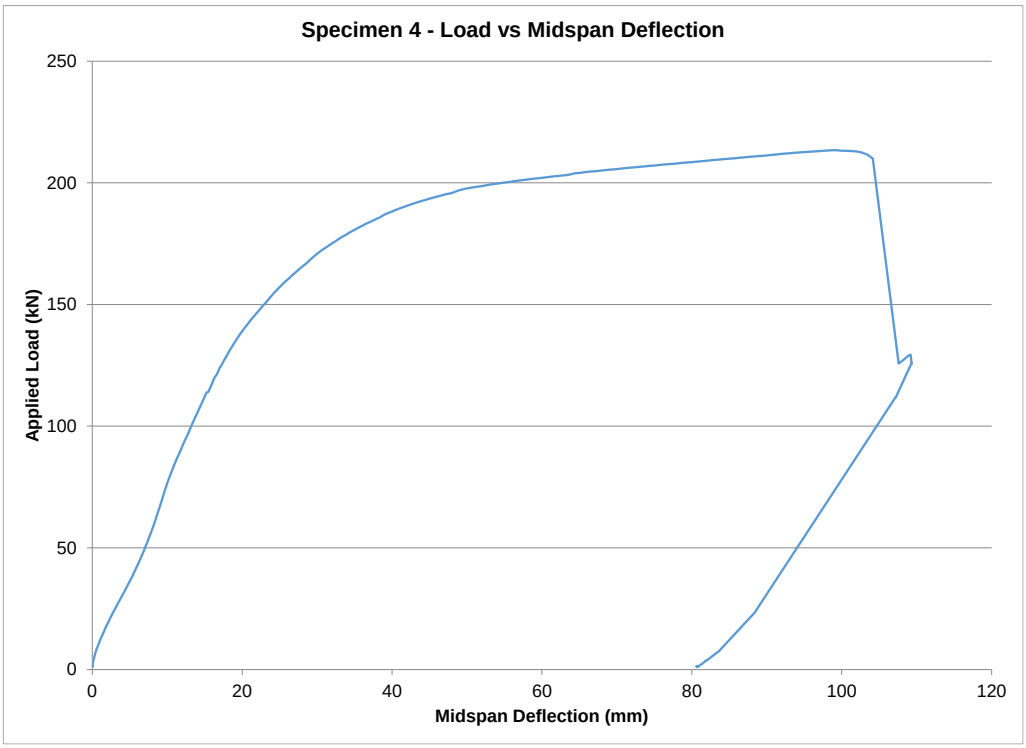

Figure 4.31: Specimen 4 - L100-25-8-NT-I - applied load vs. midspan deflection

If specimen 2 is ignored, considering the consequences of twist observed during the loading, the midspan deflection capacity of composite beams increased with the increase of the degree of composite action.

To ease the understanding of the interpretations regarding the behavior of specimens, the load versus midspan deflection curves of all specimens are combined in a single graph, which is given in Figure 4.32. According to the results, the initial stiffness of beams increased with the increase of the degree of composite action; however, it decreased with the inclusion of the hole tolerance. In addition, the inclusion of hole tolerance decreased the load-carrying and deflection capacities of the specimen. To overcome the lower stiffness caused by the inclusion of hole tolerance, bolts of the connectors may be tightened with a higher torque.

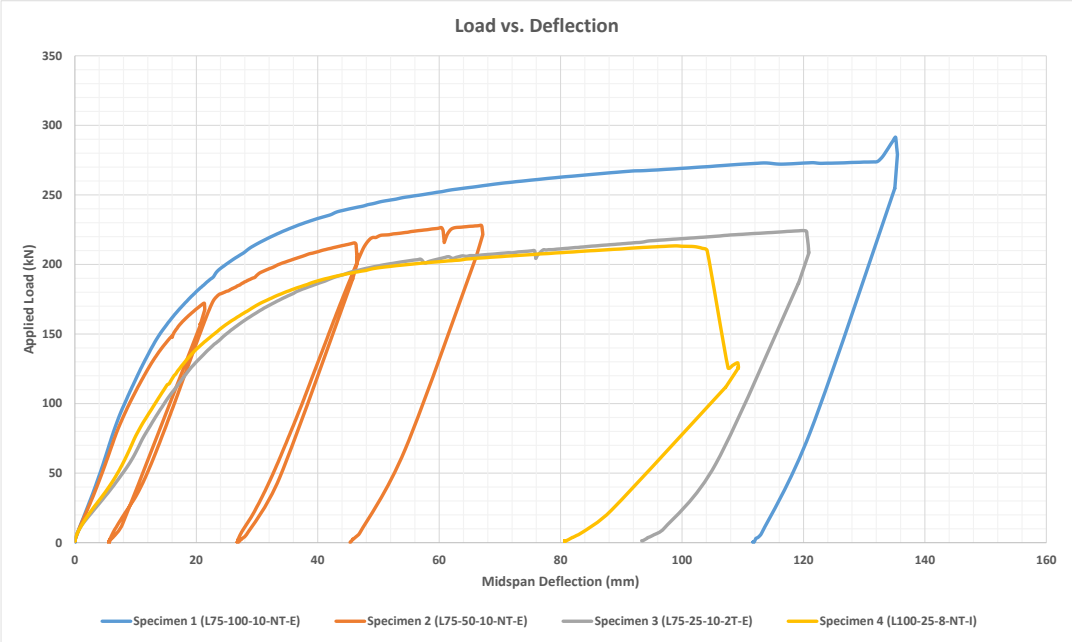

Figure 4.32: Applied load vs. midspan deflection curves of all specimens

The maximum and residual deflections observed at midspan and quarter points of each specimen are given in Table 4.27. It can be seen that residual (plastic or permanent) deflections of specimens increased with the increase of the applied load, which was the load-carrying capacity of the specimens. Additionally, quarter point deflections were higher than half of the midspan deflections, which showed that beams deflected in a quadric shape.

Table 4.27: Maximum and residual deflections of all specimens

Ultimate Loading	Specimen 1 - L75-100-10-NT-E	Specimen 2 - L75-50-10-NT-E	Specimen 3 - L75-25-10-2T-E	Specimen 4 - L100-25-8-NT-I
Applied Load (kN)	291.60	228.08	224.47	213.43
Applied Moment (kNm)	408.24	319.32	314.25	298.80
Maximum Midspan Deflection (mm)	135.47	67.20	120.86	109.30
Residual Midspan Deflection (mm)	111.66	45.33	93.36	80.68
Maximum Quarter Point Deflection (mm)	74.53	39.11	68.31	62.20
Residual Quarter Point Deflection (mm)	58.78	24.92	50.91	43.89

4.3.2.2 Load-Slip Behaviors

The end slips of the specimens under their ultimate capacities are given in Figure 4.33, Figure 4.34, Figure 4.35, and Figure 4.36, respectively.

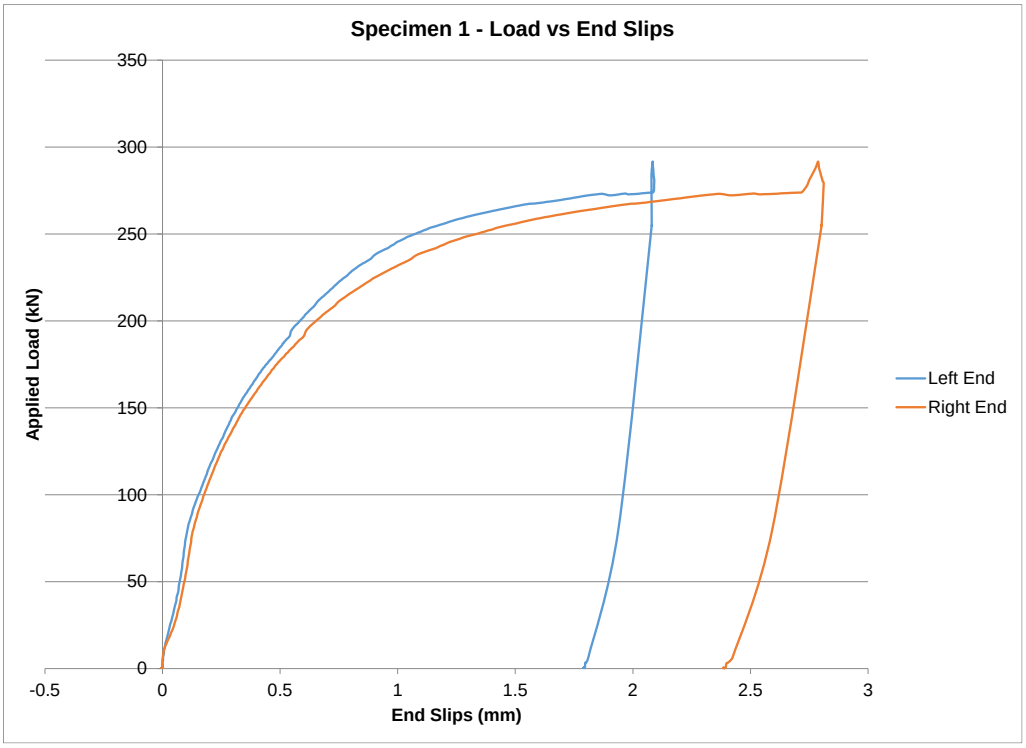

Figure 4.33: Specimen 1 - L75-100-10-NT-E - applied load vs. end slips

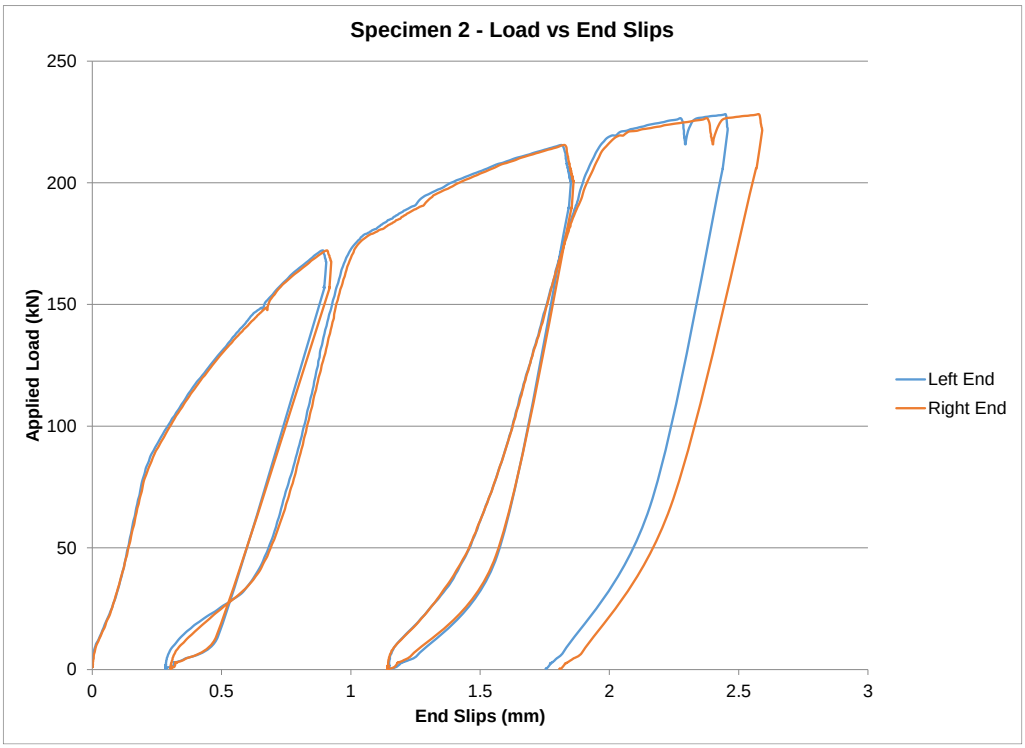

Figure 4.34: Specimen 2 - L75-50-10-NT-E - applied load vs. end slips

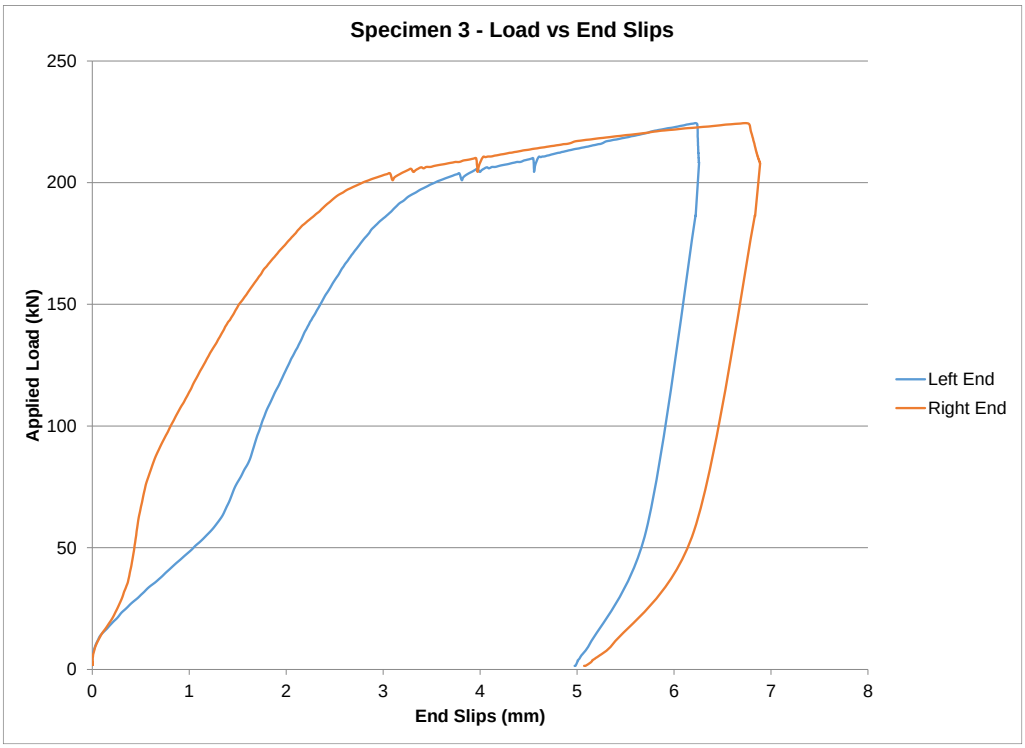

Figure 4.35: Specimen 3 - L75-25-10-2T-E - applied load vs. end slips

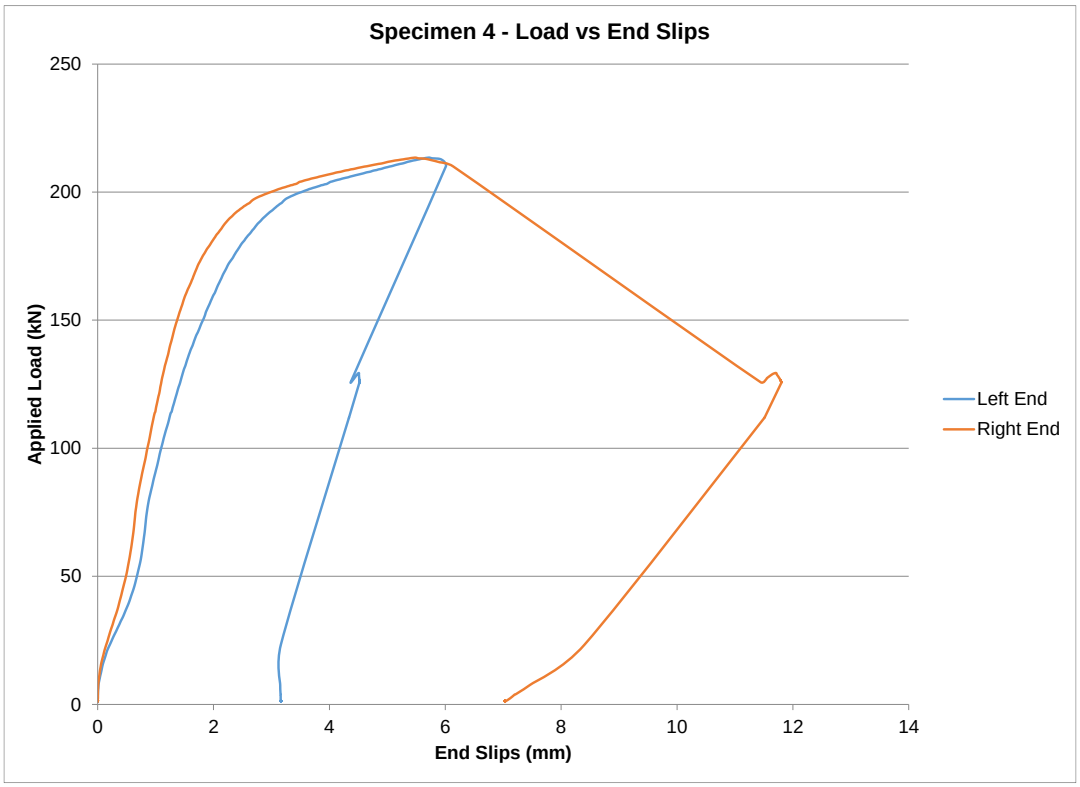

Figure 4.36: Specimen 4 - L100-25-8-NT-I - applied load vs. end slips

To ease the understanding of the interpretations regarding the behavior of specimens, the load versus average end slip curves of all specimens are combined in a single graph, which is given in Figure 4.37.

The slip demand of the specimens depended on the degree of composite action. With the increase of composite degree, slip demand increased, but the stiffness against slip decreased dramatically. Additionally, the inclusion of hole tolerance decreased initial stiffness against slip vastly. However, it should be noted that bolts on the right half of specimen 4 were sheared-off which caused a separation of concrete and steel and reduced the slipping of the left side. Thus, investigating the behavior of specimen 4 with Figure 4.36 showed that bolt shear-off may cause sudden capacity loss and differential slips of ends, i.e., higher than 7 mm.

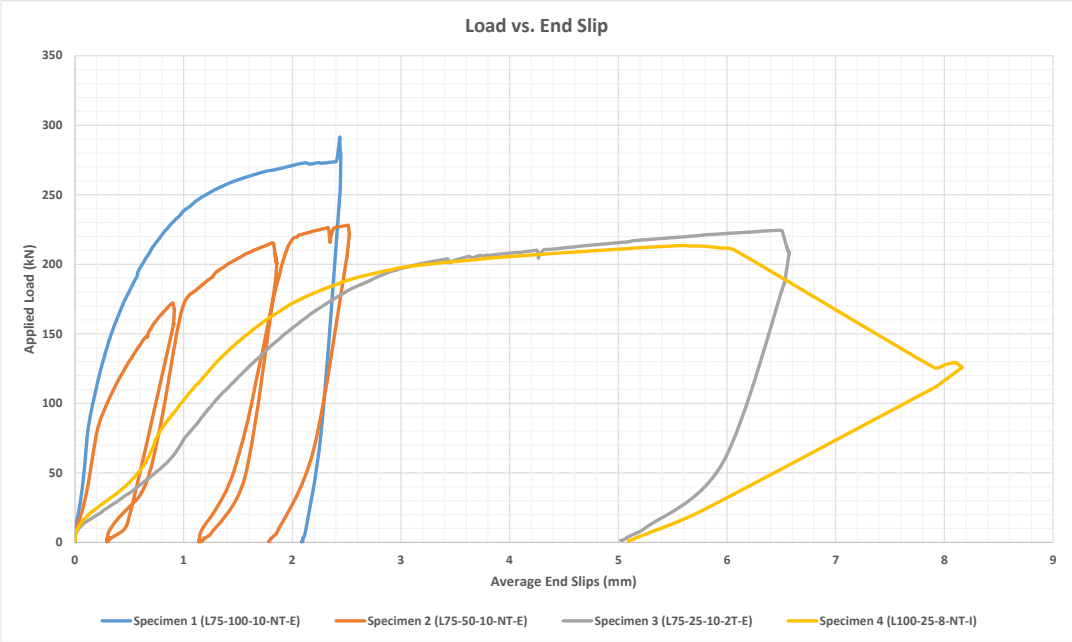

Figure 4.37: Applied load vs. average end slip curves of all specimens

The maximum and residual slips observed at the ends of each specimen are given in Table 4.28.

Table 4.28: Maximum and residual end slips of all specimens

Ultimate Loading	Specimen 1 - L75-100-10-NT-E	Specimen 2 - L75-50-10-NT-E	Specimen 3 - L75-25-10-2T-E	Specimen 4 - L100-25-8-NT-I
Applied Load (kN)	291.60	228.08	224.47	213.43
Applied Moment (kNm)	408.24	319.32	314.25	298.80
Left End (LVDT4) Slip at Ultimate Load (mm)	2.09	2.46	6.26	6.01
Left End (LVDT4) Residual slip (mm)	1.79	1.75	4.97	3.16
Right End (LVDT3) Slip at Ultimate Load (mm)	2.81	2.59	6.89	11.80
Right End (LVDT3) Residual slip (mm)	2.38	1.81	5.07	7.03

The decrease of stiffness against slip, which mainly depended on the degree of composite action, caused higher permanent slips on specimens. However, the decreased slip stiffness caused by the inclusion of hole tolerance had a negligible effect on the average residual slip.

As mentioned in Section 4.3.1.2, there were four slip recordings in both halves of the specimens. The maximum and residual slips observed at each half of the specimens are given in Table 4.29 and Table 4.30 for the left- and right-hand sides.

Table 4.29: Left half maximum and residual slips of all specimens

Ultimate Loading	Specimen 1 - L75-100-10-NT-E	Specimen 2 - L75-50-10-NT-E	Specimen 3 - L75-25-10-2T-E	Specimen 4 - L100-25-8-NT-I
Applied Load (kN)	291.60	228.08	224.47	213.43
Applied Moment (kNm)	408.24	319.32	314.25	298.80
LVDT5 (Slip 2) Slip at Ultimate Load (mm)	2.25	2.61	6.20	5.63
LVDT5 (Slip 2) Residual slip (mm)	1.89	1.89	4.92	3.18
LVDT6 (Slip 3) Slip at Ultimate Load (mm)	2.46	2.46	6.17	5.45
LVDT6 (Slip 3) Residual slip (mm)	2.09	1.68	5.00	3.09
LVDT7 (Slip 4) Slip at Ultimate Load (mm)	2.66	2.18	5.65	4.80
LVDT7 (Slip 4) Residual slip (mm)	2.33	1.65	4.69	2.88
Where from left end to the middle, LVDT order is: 5 -> 6 -> 7				

Table 4.30: Right half maximum and residual slips of all specimens

Ultimate Loading	Specimen 1 - L75-100-10-NT-E	Specimen 2 - L75-50-10-NT-E	Specimen 3 - L75-25-10-2T-E	Specimen 4 - L100-25-8-NT-I
Applied Load (kN)	291.60	228.08	224.47	213.43
Applied Moment (kNm)	408.24	319.32	314.25	298.80
LVDT10 (Slip 2) Slip at Ultimate Load (mm)	2.69	2.61	6.86	11.73
LVDT10 (Slip 2) Residual slip (mm)	2.33	1.79	4.99	7.08
LVDT9 (Slip 3) Slip at Ultimate Load (mm)	3.08	2.46	6.68	10.80
LVDT9 (Slip 3) Residual slip (mm)	2.69	1.82	4.95	7.00
LVDT8 (Slip 4) Slip at Ultimate Load (mm)	3.14	2.18	5.35	9.81
LVDT8 (Slip 4) Residual slip (mm)	2.81	1.70	4.24	6.43
Where from right end to the middle, LVDT order is: 10 -> 9 -> 8				

The slip behavior of ends was similar to each other. According to the results, it can be seen that from the ends to the middle of the specimen, maximum and residual slip decreased since the slipping free span length decreased.

4.3.2.3 Mode of Failures

The main observed failure modes were concrete crushing and bolt shear-off, as mentioned in Section 4.2.1. In general, the flexural response of the specimens was yielding at the midspan of the steel beam, as shown in Figure 4.38b, followed by crushing of the concrete deck at the midspan, as shown in Figure 4.38d. However, specimen 4 (L100-25-8-NT-I) experienced bolt shear-off, as shown in Figure 4.38c, followed by the yielding of the steel beam, which caused a separation between the steel beam and concrete deck horizontally. The excessiveness of the maximum right

end slip value, given in Figure 4.36, of specimen 4 compared to the other three specimens demonstrates its failure mode.

Figure 4.38: Beam specimen failure: a) Permanent deflection, b) Yielding at midspan, c) Bolt shear-off, d) Concrete crushing and cracks

All specimens underwent permanent deflection at the midspan regardless of the failure mode, as shown in Figure 4.38a. The cracks formed at the midspan of the deck exceeded 60 mm, which is higher than half of the height of the concrete deck, as shown in Figure 4.38d.

4.3.3 Comparison of Experimental Results with Predicted Capacities

The two main factors considered during the design phase of the structures are load-carrying capacity and serviceability limit states. The elastic deflections of the composite system can be predicted with the area transformation method, where the transformation ratio is obtained by the ratio between elastic modulus values of concrete and steel sections. Using the obtained ratio, the width of the chosen section is modified, and the calculations are carried out using the transformed system. The load-carrying capacity of composite sections can be calculated by a rigid plastic analysis, i.e., stress blocks in this study, where effective concrete height is calculated using the load-carrying capacity of the steel beam and the composite ratio. Then, the plastic neutral axis (PNA) is located to calculate the capacity.

4.3.3.1 Comparison of Elastic Deflections

As stated, the area transformation method was used to predict the elastic midspan deflections of the composite sections. As previously mentioned, the elastic modulus of the steel section was taken as 200 GPa, and the elastic modulus of the concrete deck was calculated using Equation 4.4 taken from the Hognestad Concrete model.

$$E_c = 12680 + 460 * f_{c-28} \tag{4.4}$$

$$E_c = 12680 + 460 * 28.7 = 25882\ MPa = 25.88\ GPa$$

Using the elastic modulus values, the area transformation ratio was calculated using Equation 4.5.

$$n = \frac{E_c}{E_s} \tag{4.5}$$

$$n = \frac{25.88}{200} = 0.129$$

The width of the concrete deck, which is 800 mm, was transformed using the ratio.

$$w_{modified} = 800 * n = 800 * 0.129 = 103.528\, mm$$

After area transformation, the new center of gravity was determined as $\bar{y} = 296.244\, mm$ from the bottom of the section. Using the calculated center of gravity, the moment of inertia of the transformed section was calculated with respect to the x-axis as $I_{x-x} = 2.632 * 10^{-4}\, m^4$ since the section was under positive bending.

Equation 4.6, which gives the midspan deflection for simply supported and single point loaded sections, was used to estimate the theoretical deflections.

$$\delta_{midspan} = \frac{P * L^3}{48 * E * I} \tag{4.6}$$

Where P is the applied load, L is the free span length, E is the elastic modulus, and I is the moment of inertia.

$$\delta_{midspan-25kN} = \frac{25 * 5.6^3}{48 * 200 * 10^6 * 2.632 * 10^{-4}} = 1.738 * 10^{-3}\, m = 1.738\, mm$$

$$\delta_{midspan-50kN} = \frac{50 * 5.6^3}{48 * 200 * 10^6 * 2.632 * 10^{-4}} = 3.476 * 10^{-3}\, m = 3.476\, mm$$

$$\delta_{midspan-75kN} = \frac{75 * 5.6^3}{48 * 200 * 10^6 * 2.632 * 10^{-4}} = 5.214 * 10^{-3}\, m = 5.214\, mm$$

Since the calculated deflections, i.e., 1.738, 3.476, and 5.214 mm, were for the fully-composite sections, a deflection prediction formula for partially-composite sections was needed to be used. Equation 4.7, suggested by BSI (2000) for traditional headed studs and applicability for demountable connections checked by Rehman et al. (2018), was used to calculate the midspan deflections of partially-composite specimens.

$$\delta_{partial} = \delta_{fully} + 0.5 * (1 - \eta) * \left(\delta_{steel} - \delta_{fully}\right) \tag{4.7}$$

Where $\delta_{partial}$, δ_{fully}, and δ_{steel} are the midspan deflections of partially-composite, fully-composite, and steel-only cases, respectively, and η is the degree of composite action.

The moment of inertia of the steel section was calculated as $I_{x-x} = 7.85 * 10^{-5}\ m^4$. Furthermore, using Equation 4.6 and moment of inertia, midspan deflections of steel section for 1TL, 2TL, and 3TL loads were calculated as 5.826, 11.651, and 17.477 mm.

Instead of the targeted degree of composite actions, for accuracy, back calculated composite ratios were used, i.e., 100, 56, 34, and 30%. For example, for specimen 2 under 1TL, midspan deflection was calculated as given below.

$$\delta_{56-composite} = 1.738 + 0.5 * (1 - 0.56) * (5.826 - 1.738) = 2.637\ mm$$

The midspan deflections measured during the experiments, true errors, and true percent relative errors (ε_t), which were calculated using theoretical deflections and experimental deflections, are given in Table 4.31.

Table 4.31: Elastic loading - theoretical vs. experimental deflections with errors

Specimen Name	Applied Load (kN)	Theoretical Deflection (mm)	Elastic Loading Experimental Deflection (mm)	True Error (E_t)	ε_t (%)
L75-100-10-NT-E	25	1.738	1.984	0.246	14.146
	50	3.476	4.241	0.765	22.022
	75	5.214	6.411	1.198	22.969
L75-50-10-NT-E	25	2.637	2.249	-0.388	-14.730
	50	5.274	4.711	-0.563	-10.678
	75	7.912	7.226	-0.685	-8.663
L75-25-10-2T-E	25	3.087	3.033	-0.054	-1.761
	50	6.174	7.383	1.209	19.579
	75	9.261	11.636	2.376	25.653
L100-25-8-NT-I	25	3.169	2.944	-0.225	-7.097
	50	6.337	6.751	0.414	6.533
	75	9.506	10.150	0.644	6.776

The results given in Table 4.31 show that the deflections are underestimated by 14 to 22 percent for the full composite beam. This could be attributable to the slip that takes place between steel and concrete. Even if a fully composite beam is used, slip at the interface is unavoidable. The predicted deflections for partially composite beams are more promising, especially for specimens L75-50-10-NT-E and L100-25-8-NT-I, where the errors were less than 10 percent for most of the loading cases. For L75-25-10-2T-E, the errors are greater than 20 percent; this can be attributable to the hole tolerance introduced in this specimen, which resulted in higher interface slips.

4.3.3.2 Comparison of Capacities

The load-carrying capacity of the composite sections can be calculated using a rigid plastic analysis method of stress blocks. PNA of each specimen was located using the force equilibrium with assumptions. While making the assumptions, the critical point is that with the decrease in the degree of composite action, PNA shifts downwards to increase the contribution of steel section to compression. After locating PNA, summations of the first moment of areas multiplied with the related yield or compressive strengths gave the moment capacity. However, the calculated moment capacity of the systems should be reduced since beams were already loaded under their own weight. The effect of the weight of the specimens was taken as distributed load, and the moment caused by the distributed load was calculated using Equation 4.8.

$$M_{distributed-load} = \frac{w * L^2}{8} \tag{4.8}$$

In this case, Equation 4.8 becomes:

$$w = \left(\frac{42.2}{1000} + 2.5 * 0.8 * 0.12\right) * 9.81 = 2.768 \ {}^{kN}/_{m}$$

Where 42.2 is the kg weight of the steel section per meter, 2.5 is the ton weight of the concrete deck per cubic meter, 0.8 is the deck width in meters, and 0.12 is the deck height in meters.

$$M_{weight} = \frac{2.768 * 5.6^2}{8} = 10.852\ kN * m$$

The moment capacities of the composite sections with material properties indicated in Section 4.2.3 is given in Figure 4.39.

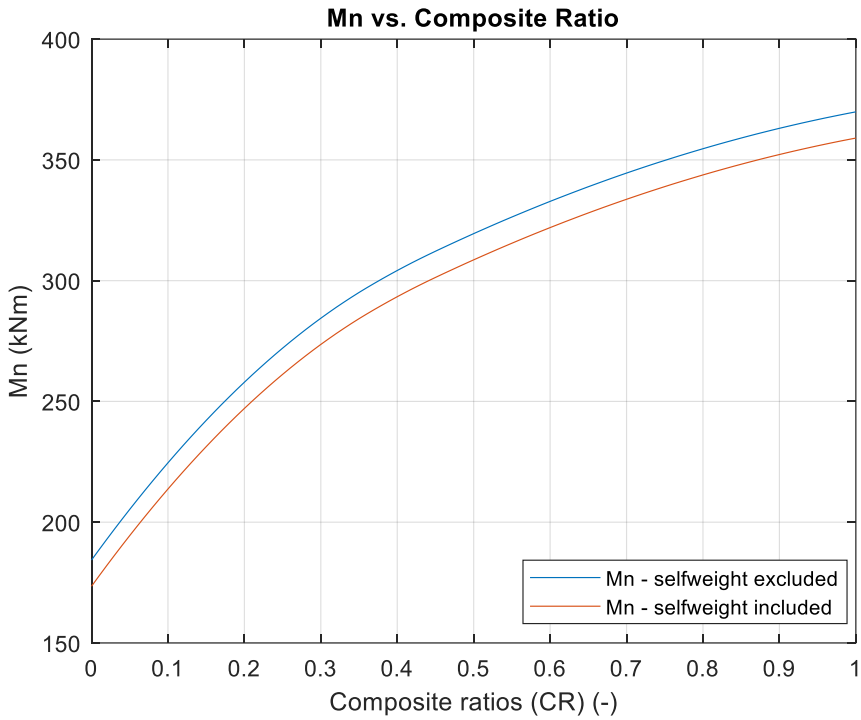

Figure 4.39: Mn vs. composite ratio

Since the free span length was 5.6 m and specimens were simply supported and under single point loading (SPL), moment capacities were used to calculate load-carrying capacities by using Equation 4.8. Calculated capacities are given in Figure 4.40.

$$P_{simply\ supported-SPL} = \frac{4 * M_n}{L} \tag{4.8}$$

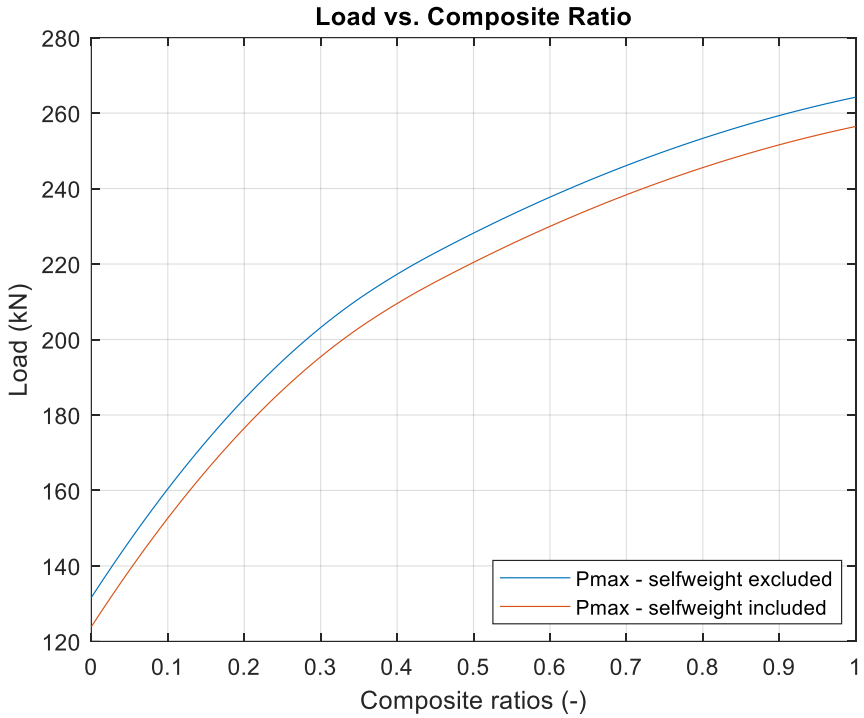

Figure 4.40: Applied load vs. composite ratio

The comparison of experimental and theoretical capacities was not possible without necessary modifications. According to Hicks & Lawson (2014), the maximum permanent midspan deflection of a composite member should not exceed 60 mm. Additionally, according to IBC (2018), permanent midspan deflection of a system similar to the test setup should be limited to L/120, which is equal to 46.67 mm in this case since the free span length of the system was 5.6 m. To evaluate the suitability of specimens to the limitations, maximum and permanent midspan deflections were calculated, as given in Table 4.32.

Table 4.32: Maximum and permanent midspan deflections of specimens

Specimen #	Maximum Midspan Deflection (mm)	Permanent Midspan Deflection (mm)	Elastic Deflection (mm)
1	135.47	111.66	23.81
2	67.20	45.33	21.87
3	120.86	93.36	27.50
4	109.30	80.68	28.62

Considering the limitations stated above and the permanent midspan deflection of specimen 2, i.e., 45.33 mm, permanent deflection of specimens 1, 2, and 4 were taken as 45 mm. The measured elastic deflection values were added to the considered permanent deflections, and the matching load values were taken as maximum applied loads, as shown in Table 4.33.

Table 4.33: Modified maximum loads

Specimen #	Permanent Deflection (mm)	Elastic Deflection (mm)	Modified Maximum Deflection (mm)	Modified Maximum Loads (kN)
1	45.00	23.81	68.81	257.70
2	45.33	21.87	67.20	228.08
3	45.00	27.50	72.50	208.65
4	45.00	28.62	73.62	206.75

The modified maximum loads were used to compare the experimental and theoretical capacities. However, back-calculated degrees of composite action were used for the accuracy of results, as given in Table 4.5, instead of targeted degrees. The results of the comparisons are given in Figure 4.39, and the obtained graph is given in Figure 4.41. After the conversion of moment capacities to load capacities, the results were given in Figure 4.40, and the obtained graph is given in Figure 4.42.

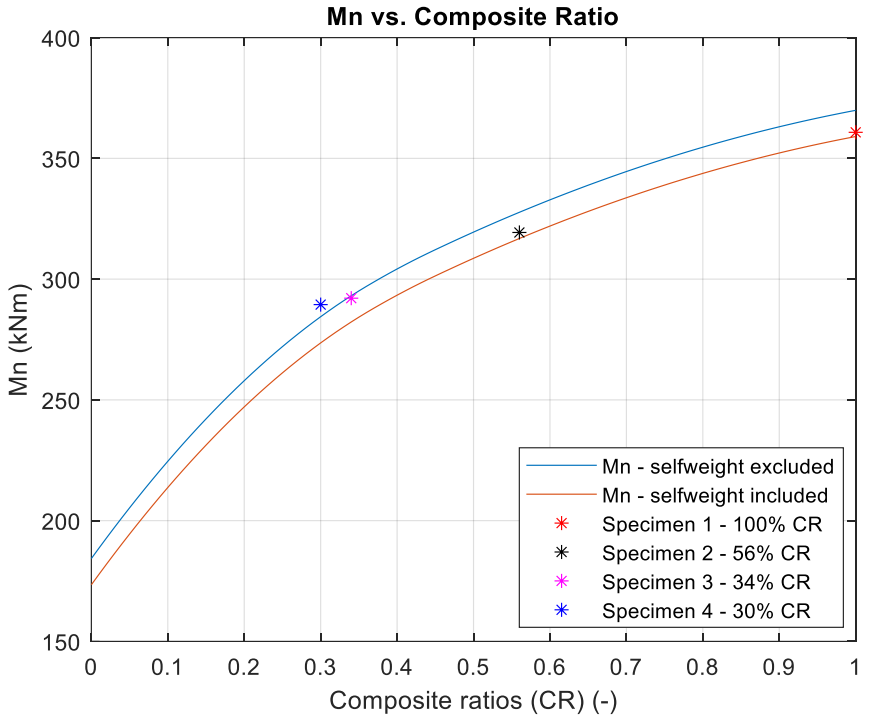

Figure 4.41: Mn vs. composite ratio with experimental values

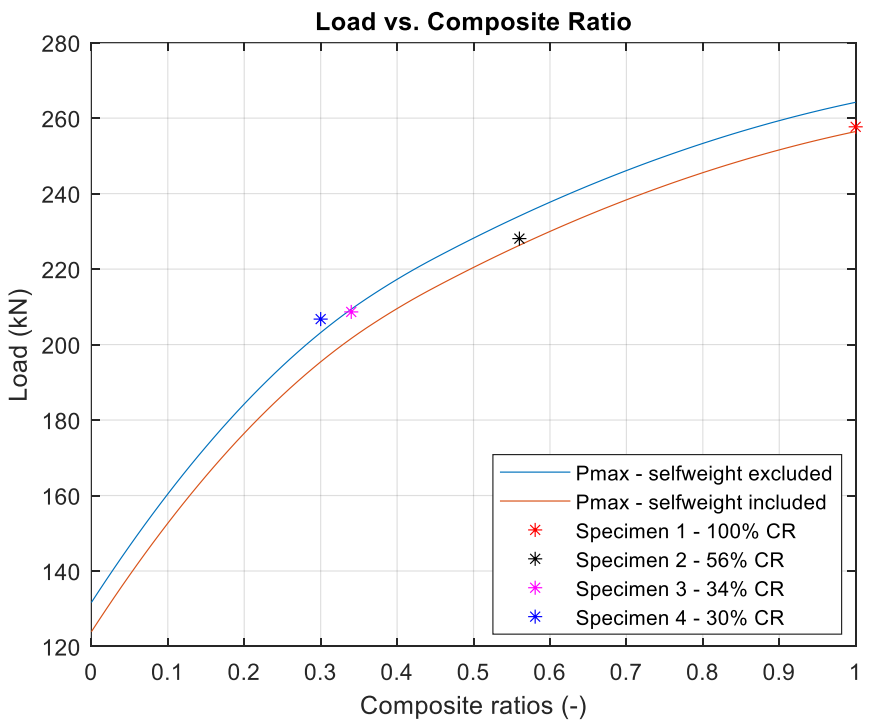

Figure 4.42: Applied load vs. composite ratio with experimental values

According to Figure 4.41 and Figure 4.42, the rigid plastic analysis, which is used to predict the load-carrying capacity of non-demountable composite systems with traditional headed studs, was accurate enough to predict the load-carrying capacities, and the capacity of the specimens is higher than the expected capacities under the effect of their own weight.

4.3.4 Demountability

After completion of the experiments, the concrete deck of each specimen was demounted from the steel beam, as illustrated in Figure 4.43. Although the demounting process was easy, it should be noted that in normal conditions, beams would be loaded under service loads unless any catastrophic event occurred. Thus, the experiment results and demountability of specimens show that the proposed connector system offers a sustainable, applicable, and beneficial connection in steel-concrete composite systems.

Figure 4.43: Demounting of a concrete deck from steel beam

CHAPTER 5

SUMMARY, CONCLUSION, AND RECOMMENDATIONS FOR FUTURE WORK

5.1 Summary

The literature review results showed that the use of a connector system providing demountability and consisting of two angle sections and a high-strength bolt was not investigated. In this thesis, the findings of an experimental research program with three phases on demountable shear connectors are reported.

In the first phase, the push-out experiments were conducted. The load-slip behavior, parameters Affecting the load and slip capacities, the failure modes of specimens, and a load-carrying capacity prediction method were obtained.

In the second phase, the pull-out experiments were conducted. The behavior of the connectors under tensile forces and the ability of the connectors to prevent the splitting between concrete and steel were obtained.

In the third phase, the full-scale beam bending experiments were conducted. The feasibility and the applicability of the proposed connectors were determined. In addition, failure modes that might be observed in practice were determined.

5.2 Conclusions

5.2.1 Conclusions related with Push-out Tests

The results of the first phase indicated that load-carrying capacity and initial stiffness of the composite systems with proposed connectors increased with the increase of the size of the angle sections, the inclusion of the bolts with higher diameters and

grades, use of concrete blocks with higher compressive strength, and exclusion of the threads from the shear plane. In addition, the placement of the connectors in the front direction to the applied load instead of the back direction was more beneficial in terms of capacity and initial stiffness. Additionally, a method for the load-carrying capacity prediction of the connectors at 6 mm slip, i.e., Eurocode 4 ductility limit, was proposed.

The slip displacement capacity, i.e., ductility, of the specimens increased with the increase of the size of the angle sections, use of the bolts with higher shear load capacity and concrete blocks with lower compressive strength, and exclusion of the threads from the shear plane. Additionally, similar to load capacity and the initial stiffness, loading of the specimens in the front direction was beneficial.

5.2.2 Conclusions related with Pull-out Tests

The results of the second phase indicated that the tensile load-carrying capacity of the specimens was increased with the increase of both the total height and size of the upper angle section. The experimental capacities of specimens were compared with the capacities predicted by ACI. According to the comparison, connectors with a total height of less than 120 mm surpassed the prediction. Therefore, the proposed connector system is a favorable alternative for welded studs in terms of tensile behavior.

5.2.3 Conclusions related with Beam Bending Tests

The results of the third phase indicated that the midspan deflection capacity of the specimens increased with the increase of the degree of composite action. The initial stiffness against deflection was also increased with the increase of composite degree; however, it decreased with the inclusion of the hole tolerance.

The slip demand of the specimens decreased with the increase of the degree of composite action. However, the decrease in the composite degree caused a dramatic decrease in the initial stiffness against slip.

According to the total results, the proposed connector system is applicable and feasible. Additionally, the connectors can be used in the design of composite beams to accommodate composite ratios between 30% and 100%.

5.3 Recommendations for Future Work

In composite construction, metal decks are used as formworks. Thus, to strengthen the applicability of the proposed connection system, testing of push-out and full-scale beam specimens with metal decks can be investigated as future work. In addition, a variety of the parameters included in the design can be increased, such as the inclusion of hole tolerance in the push-out tests and change of connector width.

REFERENCES

AASHTO. (2014). Highway bridge design specifications. In *Bridge Engineering Handbook: Fundamentals, Second Edition* (Issue September). https://doi.org/10.1201/b15616

ABAQUS. (2012). *Hibbit HD, Karlsson BI, Sorensen EP. ABAQUS user's manual Version 6.12. Pawtucket, USA: Hibbitt, Karlsson & Sorensen Inc.; 2012.* (6.12).

ACI. (2014). ACI 318-14 - Building Code Requirements for Structural Concrete. In *American Concrete Institute*.

AISC. (2016). Specification for Structural Steel Buildings, ANSI / AISC 360-16. *American Institute of Steel Construction*, 676.

Arıkoğlu, P., Baran, E., & Topkaya, C. (2020). Behavior of channel connectors in steel-concrete composite beams with precast slabs. *Journal of Constructional Steel Research*, *172*. https://doi.org/10.1016/j.jcsr.2020.106167

ASTM-A193. (2004). Standard Specification for Alloy-Steel and Stainless Steel Bolting for High Temperature or High Pressure Service and Other Special Purpose Applications. *Metallic Materials*, *03*(May 2002), 1–12. https://doi.org/10.1520/A0193

ASTM-A325. (1986). *Specification for Structural Joints Using ASTM A325 or A490 Bolts*. 28–21.

Ataei, A., Bradford, M. A., & Liu, X. (2016). Experimental study of composite beams having a precast geopolymer concrete slab and deconstructable bolted shear connectors. *Engineering Structures*, *114*, 1–13. https://doi.org/10.1016/j.engstruct.2015.10.041

Ataei, A., Zeynalian, M., & Yazdi, Y. (2019). Cyclic behaviour of bolted shear connectors in steel-concrete composite beams. *Engineering Structures*, *198*(August), 109455. https://doi.org/10.1016/j.engstruct.2019.109455

Azad, A. R. G., Kreitman, K., Engelhardt, M. D., Helwig, T., & Williamson, E. (2017). A technique for strengthening existing continuous non-composite steel girder bridges using post-installed shear connectors and inelastic moment redistribution. *IABSE Conference, Vancouver 2017: Engineering the Future - Report*, *January*, 1217–1224. https://doi.org/10.2749/vancouver.2017.1217

Balkos, K. D., Sjaarda, M., West, J. S., & Walbridge, S. (2019). Static and fatigue tests of steel-precast composite beam specimens with through-bolt shear connectors. *Journal of Bridge Engineering*, *24*(5), 04019036. https://doi.org/10.1061/(asce)be.1943-5592.0001382

Ban, H., Uy, B., Pathirana, S. W., Henderson, I. E. J., Mirza, O., & Zhu, X. (2015). Time-dependent behaviour of composite beams with blind bolts under sustained loads. *Journal of Constructional Steel Research*, *112*, 196–207. https://doi.org/10.1016/j.jcsr.2015.05.004

Biswas, M. (1986). On modular full depth bridge deck rehabilitation. *Journal of Transportation Engineering*, *112*(1), 105–120. https://doi.org/10.1061/(ASCE)0733-947X(1986)112:1(105)

BSI. (2000). *British Standard 5950-1:2000: Structural Use of Steel Work in Buildings Part 1*. *1*, 222.

Chen, Y., Zhao, Y., West, J. S., & Walbridge, S. (2014). Behaviour of steel-precast composite girders with through-bolt shear connectors under static loading. *Journal of Constructional Steel Research*, *103*, 168–178. https://doi.org/10.1016/j.jcsr.2014.09.001

Dai, X., Lam, D., & Saveri, E. (2015). Effect of concrete strength and stud collar size to shear capacity of demountable shear connectors. *Journal of Structural Engineering*, *141*(11), 04015025. https://doi.org/10.1061/(asce)st.1943-541x.0001267

Dallam, L. N. (1969). Pushout tests with high strength bolt shear connectors. *Missouri State Highway Department Department*, *99352*(68).

Dallam, L. N., & Harpster, J. L. (1968). Composite beam tests with high-strength bolt shear connectors. *Missouri State Highway Department*.

Eckelman, M. J., Brown, C., Troup, L. N., Wang, L., Webster, M. D., & Hajjar, J. F. (2018). Life cycle energy and environmental benefits of novel design-for-deconstruction structural systems in steel buildings. *Building and Environment*, *143*(April), 421–430. https://doi.org/10.1016/j.buildenv.2018.07.017

EN10002. (2001). *EN 10002:2001 - Metallic Materials - Tensile Testing*.

EN10034. (1993). EN 10034:1993 - Specification for Structural steel I and H section - Tolerances on shape and dimensions. In *British Standard* (p. 14).

EN10056-2. (1993). *EN 10056-2:1993 - Specification for Structural steel equal and unequal leg angles - Part 2: Tolerances on shape and dimensions* (p. 12).

EN14399. (2009). EN14300-10: High-strength structural bolting assemblies for preloading - Part 10: System HRC - Bolt and nut assemblies with calibrated preload. In *British Standard* (Vol. 3).

Eurocode 4. (2011). *EN1994-1-1 - Eurocode 4: Design of composite steel and concrete structures – Part 1-1: General rules and rules for buildings*. *1*(2005).

Eurocode 4. (2012). *EN1994-1-2 - Eurocode 4: Design of composite steel and concrete structures – Part 1-2: General rules - Structural fire design*. *1*(2005).

Feidaki, E., Vasdravellis, G., He, J., & Wang, S. (2019). Steel-yielding demountable shear connector for composite floors with precast hollow-core slab units. *Journal of Structural Engineering*, *145*(8), 04019076. https://doi.org/10.1061/(asce)st.1943-541x.0002356

Girão Coelho, A. M., Lawson, R. M., & Aggelopoulos, E. S. (2019). Optimum use of composite structures for demountable construction. *Structures*, *20*(January), 116–133. https://doi.org/10.1016/j.istruc.2019.03.005

Henderson, I. E. J., Zhu, X., Uy, B., & Mirza, O. (2015a). Dynamic behaviour of

steel-concrete composite beams with different types of shear connectors. Part I: Experimental study. *Engineering Structures*, *103*, 298–307. https://doi.org/10.1016/j.engstruct.2015.08.035

Henderson, I. E. J., Zhu, X., Uy, B., & Mirza, O. (2015b). Dynamic behaviour of steel-concrete composite beams with different types of shear connectors. Part II: Modelling and comparison. *Engineering Structures*, *103*, 308–317. https://doi.org/10.1016/j.engstruct.2015.08.033

Hicks, S. J., & Lawson, R. M. (2014). *Design of composite beams using precast concrete slabs*. *April*. https://doi.org/10.13140/RG.2.2.23890.35529

IBC. (2018). International Building Code 2018. In *International Code Council* (Vol. 53, Issue 9). International Code Council.

Kozma, A., Odenbreit, C., Braun, M. V., Veljković, M., & Nijgh, M. P. (2018). Push-out tests on demountable shear connectors of steel-concrete composite structures. *12th International Conference on Advances in Steel-Concrete Composite Structures*. https://doi.org/10.4995/asccs2018.2018.7155

Kozma, A., Odenbreit, C., Braun, M. V., Veljković, M., & Nijgh, M. P. (2019). Push-out tests on demountable shear connectors of steel-concrete composite structures. *Structures*, *21*(April), 45–54. https://doi.org/10.1016/j.istruc.2019.05.011

Kwon, G., Engelhardt, M. D., & Klingner, R. E. (2009). Strengthening bridges by developing composite action in existing non-composite bridge girders. *Structural Engineering International: Journal of the International Association for Bridge and Structural Engineering (IABSE)*, *19*(4), 432–437. https://doi.org/10.2749/101686609789847109

Kwon, G., Engelhardt, M. D., & Klingner, R. E. (2010a). A case study of bridge strengthening through the use of post-installed shear connectors. *Structures Congress 2010*, *2004*, 666–675. https://doi.org/10.1061/41130(369)61

Kwon, G., Engelhardt, M. D., & Klingner, R. E. (2010b). Behavior of post-installed shear connectors under static and fatigue loading. *Journal of Constructional Steel Research*, *66*(4), 532–541. https://doi.org/10.1016/j.jcsr.2009.09.012

Kwon, G., Engelhardt, M. D., & Klingner, R. E. (2011). Experimental behavior of bridge beams retrofitted with postinstalled shear connectors. *Journal of Bridge Engineering*, *16*(4), 536–545. https://doi.org/10.1061/(asce)be.1943-5592.0000184

Kwon, G., Engelhardt, M. D., & Klingner, R. E. (2012). Parametric Studies and Preliminary Design Recommendations on the Use of Postinstalled Shear Connectors for Strengthening Noncomposite Steel Bridges. *Journal of Bridge Engineering*, *17*(2), 310–317. https://doi.org/10.1061/(asce)be.1943-5592.0000261

Lam, D., Dai, X., Ashour, A., & Rehman, N. (2017). Recent research on composite beams with demountable shear connectors. *Steel Construction*, *10*(2), 125–134. https://doi.org/10.1002/stco.201710016

Langarudi, P. A., & Ebrahimnejad, M. (2020). Numerical study of the behavior of bolted shear connectors in composite slabs with steel deck. *Structures*, *26*(April), 501–515. https://doi.org/10.1016/j.istruc.2020.04.037

Liberati, E. A. P., Nogueira, C. G., Leonel, E. D., & Chateauneuf, A. (2016). Failure analysis of reinforced concrete structures subjected to chloride penetration and reinforcements corrosion. In *Handbook of Materials Failure Analysis with Case Studies from the Chemicals, Concrete and Power Industries*. Elsevier Ltd. https://doi.org/10.1016/B978-0-08-100116-5.00005-3

Liu, X., Bradford, M. A., & Ataei, A. (2017). Flexural performance of innovative sustainable composite steel-concrete beams. *Engineering Structures*, *130*, 282–296. https://doi.org/10.1016/j.engstruct.2016.10.009

Liu, X., Bradford, M. A., Chen, Q. J., & Ban, H. (2016). Finite element modelling of steel-concrete composite beams with high-strength friction-grip bolt shear

connectors. *Finite Elements in Analysis and Design*, *108*, 54–65. https://doi.org/10.1016/j.finel.2015.09.004

Liu, X., Bradford, M. A., & Lee, M. S. S. (2015). Behavior of high-strength friction-grip bolted shear connectors in sustainable composite beams. *Journal of Structural Engineering*, *141*(6), 04014149. https://doi.org/10.1061/(asce)st.1943-541x.0001090

Loqman, N., Safiee, N. A., Bakar, N. A., & Nasir, N. A. M. (2018). Structural Behavior of Steel-Concrete Composite Beam using Bolted Shear Connectors: A Review. *MATEC Web of Conferences*, *203*, 1–12. https://doi.org/10.1051/matecconf/201820306010

Moynihan, M. C., & Allwood, J. M. (2014). Viability and performance of demountable composite connectors. *Journal of Constructional Steel Research*, *99*, 47–56. https://doi.org/10.1016/j.jcsr.2014.03.008

Nijgh, M. P., Gîrbacea, I. A., & Veljković, M. (2019). Elastic behaviour of a tapered steel-concrete composite beam optimized for reuse. *Engineering Structures*, *183*(August 2018), 366–374. https://doi.org/10.1016/j.engstruct.2019.01.022

Odenbreit, C., & Kozma, A. (2019). Dismountable flooring systems for multiple use. *IOP Conference Series: Earth and Environmental Science*, *225*(1). https://doi.org/10.1088/1755-1315/225/1/012028

Pathirana, S. W., Uy, B., Mirza, O., & Zhu, X. (2015). Strengthening of existing composite steel-concrete beams utilising bolted shear connectors and welded studs. *Journal of Constructional Steel Research*, *114*, 417–430. https://doi.org/10.1016/j.jcsr.2015.09.006

Pathirana, S. W., Uy, B., Mirza, O., & Zhu, X. (2016a). Bolted and welded connectors for the rehabilitation of composite beams. *Journal of Constructional Steel Research*, *125*, 61–73. https://doi.org/10.1016/j.jcsr.2016.06.003

Pathirana, S. W., Uy, B., Mirza, O., & Zhu, X. (2016b). Flexural behaviour of

composite steel-concrete beams utilising blind bolt shear connectors. *Engineering Structures*, *114*, 181–194. https://doi.org/10.1016/j.engstruct.2016.01.057

Pavlović, M., Marković, Z., Veljković, M., & Budevac, D. (2013). Bolted shear connectors vs. headed studs behaviour in push-out tests. *Journal of Constructional Steel Research*, *88*, 134–149. https://doi.org/10.1016/j.jcsr.2013.05.003

Pavlović, M., Spremić, M., Marković, Z., Budevac, D., & Veljković, M. (2014). Recent research of shear connection in prefabricated steel-concrete composite beams. *Journal of Applied Engineering Science*, *12*(1), 75–80. https://doi.org/10.5937/jaes12-5676

Rehman, N., Lam, D., Dai, X., & Ashour, A. (2016). Experimental study on demountable shear connectors in composite slabs with profiled decking. *Journal of Constructional Steel Research*, *122*, 178–189. https://doi.org/10.1016/j.jcsr.2016.03.021

Rehman, N., Lam, D., Dai, X., & Ashour, A. (2018). Testing of composite beam with demountable shear connectors. *Proceedings of the Institution of Civil Engineers: Structures and Buildings*, *171*(1), 3–16. https://doi.org/10.1680/jstbu.16.00172

Rowe, M., & Bradford, M. A. (2013). Partial shear interaction in deconstructable steel-concrete composite beams with bolted shear connectors. *Design, Fabrication and Economy of Metal Structures*, *1968*, 585–590. https://doi.org/10.1007/978-3-642-36691-8_87

Sencu, R. M., Wang, Y. C., Yang, J., & Lam, D. (2019). Performance evaluation of demountable shear connectors with collar step at ambient and elevated temperatures. *Engineering Structures*, *194*(May), 94–105. https://doi.org/10.1016/j.engstruct.2019.05.059

Suwaed, A. S. H., He, J., & Vasdravellis, G. (2022). Experimental and numerical

evaluation of a welded demountable shear connector through horizontal pushout tests. *Journal of Structural Engineering*, *148*(2), 1–13. https://doi.org/10.1061/(asce)st.1943-541x.0003269

Suwaed, A. S. H., & Karavasilis, T. L. (2017). Novel demountable shear connector for accelerated disassembly, repair, or replacement of precast steel-concrete composite bridges. *Journal of Bridge Engineering*, *22*(9), 04017052. https://doi.org/10.1061/(asce)be.1943-5592.0001080

Suwaed, A. S. H., & Karavasilis, T. L. (2018). Removable shear connector for steel-concrete composite bridges. *Steel and Composite Structures*, *29*(1), 107–123. https://doi.org/10.12989/scs.2018.29.1.107

Tan, E. L., Varsani, H., & Liao, F. (2019). Experimental study on demountable steel-concrete connectors subjected to combined shear and tension. *Engineering Structures*, *183*(May 2018), 110–123. https://doi.org/10.1016/j.engstruct.2018.12.088

Wang, J. Y., Guo, J. Y., Jia, L. J., Chen, S. M., & Dong, Y. (2017). Push-out tests of demountable headed stud shear connectors in steel-UHPC composite structures. *Composite Structures*, *170*, 69–79. https://doi.org/10.1016/j.compstruct.2017.03.004

Wang, L., Webster, M. D., & Hajjar, J. F. (2019). Pushout tests on deconstructable steel-concrete shear connections in sustainable composite beams. *Journal of Constructional Steel Research*, *153*, 618–637. https://doi.org/10.1016/j.jcsr.2018.10.020

Wang, L., Webster, M. D., & Hajjar, J. F. (2020). Design for deconstruction using sustainable composite beams with precast concrete planks and clamping connectors. *Journal of Structural Engineering*, *146*(8), 04020158. https://doi.org/10.1061/(asce)st.1943-541x.0002659

Yang, F., Liu, Y., Jiang, Z., & Xin, H. (2018). Shear performance of a novel demountable steel-concrete bolted connector under static push-out tests.

Engineering Structures, *160*(December 2017), 133–146. https://doi.org/10.1016/j.engstruct.2018.01.005

Yi, N. H., Kim, J. H. J., Han, T. S., Cho, Y. G., & Lee, J. H. (2012). Blast-resistant characteristics of ultra-high strength concrete and reactive powder concrete. *Construction and Building Materials*, *28*(1), 694–707. https://doi.org/10.1016/j.conbuildmat.2011.09.014